Femtosecond Laser Processing of Wide Bandgap Semiconductors and Their Applications

A thesis presented
by

Katherine Collett Furr Phillips

to
The School of Engineering and Applied Sciences
in partial fulfillment of the requirements
for the degree of
Doctor of Philosophy
in the subject of

Applied Physics

Harvard University
Cambridge, Massachusetts
September 2014

Thesis advisor Author

Eric Mazur **Katherine Collett Furr Phillips**

Femtosecond Laser Processing of Wide Bandgap Semiconductors and Their Applications

Abstract

This thesis explores the production, characterization, and water oxidation efficiency of wide bandgap semiconductors made through femtosecond-laser irradiation of various materials. Our investigation focuses on three main aspects: 1) producing titanium dioxide (TiO_2) from titanium metal, 2) using our laser-made materials in a photoelectrochemical cell for water oxidation, and 3) utilizing the femtosecond laser to create a variety of other mixed metal oxides for further water oxidation studies and biological applications.

We first discuss producing TiO_2 and titanium nitride. We report that there is chemical selectivity at play in the femtosecond laser doping process so not all dopants in the surrounding atmosphere will necessarily be incorporated. We then show that the material made from laser-irradiation of titanium metal, when annealed, has a three-fold enhancement in overall water oxidation when irradiated with UV light. We attribute this enhancement through various material characterization methods to the creation of a more pure form of rutile TiO_2 with less defects. We then present a variety of studies done with doping both TiO_2 and other oxides with broadband photoelectrochemistry and offer that the dopant incorporation hurts the overall water oxidation rate. Lastly, we use the laser-treated titanium to test cell adhesion and viability.

Our results demonstrate an ability to femtosecond-laser process semiconductors to produce materials that no one has made previously and study their properties using collaborations across chemistry and biology, yielding true interdisciplinary research.

CONTENTS

Citations to previously published work

Parts of this dissertation cover research reported in the following articles:

1. E. C. Landis, K. C. Phillips, C. M. Friend, and E. Mazur, “Formation of nanostructured TiO_2 by femtosecond laser irradiation of titanium in O_2,” *Journal of Applied Physics*, **112**, 063108, 2012.

2. K. C. Phillips, H. Ghandi, and E. Mazur, “Ultrafast laser processing of semiconductors,” *Submitted to Advances in Optics and Photonics*, 2014.

3. K. C. Phillips, T. Cremer, A. Bartasyte, J. Suntivich, A.-K. Henss, C. M. Friend, and E. Mazur, “Production of rutile TiO_2 on titanium foil via femtosecond laser irradiation for photoelectrochemical oxygen evolution,” *Submitted to ACS Catalysis*, 2014.

4. K. C. Phillips, J. Suntivich, C. M. Friend, and E. Mazur, “Femtosecond doping of $3d$ transition metals in TiO_2: The effect of the dopant chemistry on the light-assisted oxygen evolution activity,” *In preparation*, 2014.

5. J. D. B. Bradley, C. C. Evans, J. T. Choy, O. Reshef, P. B. Deotare, F. Parsy, K. C. Phillips, M. Loncar, and E. Mazur, “Submicrometer-wide amorphous and polycrystalline anatase TiO_2 waveguides for microphotonic devices.,” *Optics Express*, **20**, 21, 2012.

Acknowledgments

> "Most people say that it is the intellect which makes a great scientist.
> They are wrong: it is character."
>
> *Albert Einstein*

I firmly believe that many different types of people can be scientists, and it is the amazing people around me that have helped me to fulfill my dream of receiving my PhD. I have had the wonderful opportunity to work and learn among the world's best and brightest, and it has been an honor for the past five years. I have found that success in both research and life takes perseverance, confidence, and most importantly, support from all of those around you. I am forever grateful for the love and patience that so many have shown me during my life, and it will take a lifetime to repay what my family, friends, and colleagues have given me thus far.

My journey to graduate school was a long one—I have wanted my PhD from around the time I entered kindergarten when I accompanied my mom in her trips to UNCC, where she is a professor. I have learned from some of the best teachers a student can ask for, and I want to thank especially Ms. Lynn (preschool), Mr. Taylor (middle school social studies), Ms. Womack (high school history), Mr. Strong (theory of knowledge), Mr. Madre (high school calculus), and Mr. Patterson (high school physics) for letting me explore my curiosity and pushing me to excel in everything that I do.

At NC State University, I had a few professors who especially helped me along the way. I want to thank Karen Daniels for letting me be her first student and Stephen Reynolds, who showed me that you can have many passions in life and still be a physicist. With the Park Program, I want to thank Eva Feucht, Laura Lunsford, my roommates (Rachel Babson, Rachel Blackmon, and Lindsey Robinson), and the

Park Scholars for their support and love in pushing the envelope on what a physics major can accomplish. When I moved to Cambridge University, I found so many like-minded individuals, and their love and support throughout my time in England and at Harvard have been very important to me.

I would like to thank Eric Mazur for the amazing opportunity to be one of his students and a member of his group, both through the undergraduate REU program and as a graduate student. I have learned so much from Eric, especially how to look beyond the initial results, craft a perfect talk, and control the message. I have become more self-confident and resilient, and I thank Eric for teaching me these and many other scientific and useful skills. As I leave Harvard and explore the world, I know I will appreciate all the lessons learned here in a new way.

As for my committee, I want to first thank Cynthia Friend for her continued support during my PhD. She opened her lab, her research group, and her resources to my project, and I know that I would not have succeeded without her guidance and support. I would also like to thank Tim Kaxiras for his support while on my thesis committee, Tonio Buonassisi for his solar knowledge, and Evelyn Hu for her guidance in all parts of life.

In relation to my research, I want to first thank all of the Black Silicon subgroup: Renee Sher, Yu-Ting Lin, Ben Franta, Guoliang Deng, Alex Raymond, Hemi Gandhi, and Matt Smith for supporting my non-silicon based research. For the watersplitting and photochemistry experiments, I want to specifically thank those that helped make my thesis research possible, including Jin Suntivich, Elizabeth Landis, Anne Co, Ausrine Bartasyte, Yang Shao-Horn, Till Cremer, Tian Ming, Ann-Kathrin Henss, and the rest of the Friend group. With my brief foray into biophysics research, I want to thank Nabiha Saklayen, Marinus Huber, Weilu Shen, and Lauren Milling for helping my last PhD wish come true with the work on dental implants.

In relation to the Mazur group, with whom I spent most of my time as a graduate student, I would like to thank my peers for supporting me throughout my PhD and the thesis writing process: Sally Kang, Orad Reshef, Phil Munoz, Sarah Griesse-Nascimento, Chris Evans, Michael Moebius, Kelly Miller, and Sebastien Courvoisier. Because I have spent many years in and out of the Mazur group, I would like to then thank the older graduate students and researchers who supported me as an REU and helped me with my decision to come to Harvard: Geoff Svacha, Tina Shih, Rafael Gattass, Jessica Watkins, and Sam Chung. Once I came to Harvard as a graduate student, I appreciate all the guidance and support that many older graduate students gave me, which includes Jason Dowd, Eric Diebold, Mark Winkler, Prakriti Tayalia, Kevin Vora, and Haifei Zhang. I would also like to thank the younger students for their enthusiasm and love for science: Daryl Vulis, Marinna Madrid, Weilu Shen, Sam Kim, Ruwan Senaratne, and Stephanie Swartz. Finally, I immensely appreciate the input and guidance I received from the many postdocs and visitors that I had the pleasure to work with: Valeria Nuzzo, Jon Bradley, Paul Peng, Brian Lukoff, Julie Schell, Laura Tucker, Erwin Marti, Yang Li, Yuto Tanaka, Thierry Sarnet, Shobha Shukla, Michel Meunier, and James Fraser.

In addition, I must thank Virginia Casas for everything that she does in keeping the Mazur group running and knowing all the intricacies that make Harvard such a special place to navigate.

Outside of the lab, I want to thank Jean Anne and Kevin Incorvia, Elise Novitski, Lauren Hartle, Rebecca Perry, Grant England, Brian Clark, Roger Diebold, Shanying Cui, Julie Sygiel, and Halley Jacobs for being supportive friends for the past few years, and I cannot wait to see you all achieve your dreams.

Most importantly, I want to thank my family for constantly supporting me. I want to thank my mom, Susan Furr, for putting my dreams above all else and showing me that there is no limit to what I can achieve. I want to thank my dad, Ted Phillips, for doing whatever it takes for me to succeed and for being there in all my moments of doubt. I know that you both have sacrificed so much, and no matter what I do, I know that I cannot repay all that you have done for me. Lastly, I want to thank my brother, James Phillips, for keeping me grounded, and I have really enjoyed watching you develop both intellectually and socially—you are going to do wonderful things!

I also want to thank Alex Showers for his unending love and support for the entirety of my PhD. His humor and level-headedness are always appreciated and have made the thesis research and writing fly by. I cannot wait to experience all that life has to offer us and look forward to every experience and adventure we go on together.

Finally, I want to dedicate this thesis to my maternal grandmother, Myrtle Collett Furr, whom I always called Kiki—she was the light of my life, and I just wish she was here to share all of these amazing experiences. I only hope that I can mimic her kindness and dedication to hard work in all that I pursue in life.

On a less serious note, I want to thank LeVar Burton for showing me how fun reading is and the true meaning of "teamwork", Julia Child for demonstrating that anyone can make something wonderful, Sally Ride for showing me that I can soar,

and Disney for making every journey full of life and love. To quote one of my favorite leaders, Eleanor Roosevelt: "The future belongs to those who believe in the beauty of their dreams." Thank you to all that are reading this for believing in my dreams and making them come true.

Kasey Phillips

September 2014

Cambridge, MA

Acknowledgement of Financial Support

This thesis is based on work funded by the National Science Foundation under contract CHE-DMR-DMS 0934480, support from the National Science Foundation Graduate Research Fellowship under Grant Nos. DGE 0644491 and DGE 0946799, and support from the Department of Defense (DoD) through the National Defense Science and Engineering Graduate Fellowship (NDSEG) Program. I would also like to thank the Park Foundation for my support at NC State University and the Center for Nanoscale Systems for providing many tools that I utilized in my research. All of these organizations have given me the freedom to explore all that I found interesting and exciting in science and beyond.

To my loving family and for all that they have given. It is in the completion of this thesis that I hope to make you proud.

CHAPTER 1

INTRODUCTION

1.1 Overview

Femtosecond-laser processing has provided many new avenues for light-trapping and opened the field of hyperdoping when Black Silicon was first produced twenty years ago. We have now extended this method to a whole host of other materials, namely oxides. Wide bandgap semiconductors possess many properties that make it more difficult to work with than silicon, including multiple constituent elements and a bandgap that does not absorb our 800-nm laser wavelength. In addition, we used our knowledge gained with silicon to approach a different problem in the field of solar fuels, where we use materials that can both absorb light and perform water oxidation to produce hydrogen for the hydrogen economy. With femtosecond-laser processing, we can produce surface structures and introduce new materials into a host material. In this dissertation, we demonstrate that we can first produce oxides by laser-texturing metal surfaces in an oxygen-containing atmosphere and show the first successful implementation of laser-made TiO_2 for water oxidation applications. We then present studies on dopant-inclusion in oxides, perform photoelectrochemistry, and consider how the oxidation state of the dopant affects the water oxidation rate. Lastly, we discuss using TiO_2 as a platform for cell adhesion and viability for biological applications.

1.2 Organization of the dissertation

This thesis reports on our progress in extending our fs-laser hyperdoping process to oxides, namely TiO_2, and using the materials made to perform water oxidation and cell growth for biological applications.

Chapter 2 gives an overview of all types of material processing of semiconductors using ultrafast lasers and describes a variety of applications, including surface modification, bulk modification, and deposition techniques.

Chapter 3 investigates the production of TiO_2 from femtosecond-laser processing of titanium metal in oxygen and shows the chemical selectivity at play between oxygen and nitrogen doping during laser irradiation.

In Chapter 4, we study the efficiency of water oxidation for non-doped TiO_2 and give an in-depth elemental analysis of the laser-made material. We also compare our annealed, laser-treated sample to two different control samples to show we produce a more efficient, higher-qualtiy rutile TiO_2 with femtosecond laser irradiation.

Chapter 5 presents the doping of a variety of wide bandgap semiconductors. In this section, we demonstrate that laser doping of TiO_2 and other oxides is possible with different dopants, but the doping does not increase the overall efficiency of water oxidation and that the dopant oxidation state is an important factor in the resulting photoelectrochemistry.

Chapter 6 introduces a study of cell adhesion and viability on the laser-structured titanium metal and shows that the surface structures aid the growth of cells when compared to titanium foil, producing a potential new material for dental implants.

Chapter 7 summarizes the main results obtained in this thesis and proposes future avenues of research in hyperdoping and surface structuring with femtosecond lasers.

Appendix A provides information on the history and implementation of Chirped Pulse Amplification for ultrafast lasers.

CHAPTER 2

ULTRAFAST PROCESSING OF SEMICONDUCTORS AND APPLICATIONS

In this chapter, we cover various applications of femtosecond laser processing and give an overview of the different processes that can result from using an ultrafast laser on a host of materials. We cover surface and bulk applications and show how femtosecond lasers can be used to deposit various materials. We will show the advantages and disadvantages of using ultrafast lasers compared to lasers that operate in other regimes.

2.1 Introduction

Ultrafast lasers have been developed over half a century and are becoming more user-friendly and less costly every year. Ultrafast lasers incorporate both the femtosecond (1 fs = 10^{-15} s) and picosecond (1 ps = 10^{-12} s) time regimes, where both types of lasers have been used to interact with and characterize hosts of different materials. Compared to longer pulse widths, ultrafast pulses are unique in that they are characterized by incredibly high peak intensities and interact with materials on a time scale faster than heat diffusion. These two features allow ultrafast lasers to very precisely manipulate materials.

Over the last decades, several factors have increased the interest in applications of ultrafast processing of semiconductors. [1] Across industries, feature sizes are becoming smaller, and components are becoming more densely packed which require ultrafast lasers to manipulate. Along with smaller devices, several applications employing ultrafast lasers have been established that have given more attention to ultrafast laser processing, including automobile machining, LASIK eye surgery, and photomask repair. [2] Lastly, with the development of turnkey ultrafast systems that are easier to use, more research with ultrafast laser-matter interactions is occurring across disciplines while industrial users are exploring more avenues for ultrafast application processing.

In this chapter, we will first briefly present an introduction to and history of ultrafast laser processing of semiconductors. Next, we will give an overview of the fundamental physical processes that occur in ultrafast light-matter interactions. Then, we will discuss various surface modification, bulk modification, and deposition applications of ultrafast laser processing.

2.1.1 Femtosecond laser history

The creation of mode-locking, or fixing the phase between the longitudinal modes in a laser cavity, transformed the laser industry in 1964 and made the generation of picosecond pulses possible for the first time. [3, 4] With shorter pulses come higher peak intensities, and these new picosecond pulses brought intensities on the order of 10^9 W/cm^2. To amplify picosecond pulses and extract these higher energies, the nonlinear effects that occur at such high powers first need to be taken into account. [5] As the intensity is spatially-dependent, the nonlinear phase also changes over the length of the pulse. For a Gaussian-shaped pulse, the nonlinear phase will be largest in the center of the pulse where the intensity is the highest. This phase results in a spatially-dependent nonlinear index, and with a larger index of refraction in the center, the pulse acts like a lens and self-focuses. The process of self-focusing damages the lasing crystal at high enough intensities.

Chirped Pulse Amplification was developed to amplify the pulses while keeping the nonlinear effects from destroying the crystal. [6] Chirped Pulse Amplification consists of three steps: pulse spreading, amplification, and pulse compression (Fig. 2.1). By spreading the pulse orders of magnitude (usually about 10^4–10^8 times), the pulse can be amplified in the crystal without approaching the damage threshold or having intensities where nonlinear effects come into play. [7] With a spread pulse, the fluence remains the same but the power measured at any one frequency is much lower. After amplification, the pulse is then compressed.

The process of spreading and compressing can be achieved with many configurations, such as gratings, prisms, or lenses. The first spreader was designed in 1985

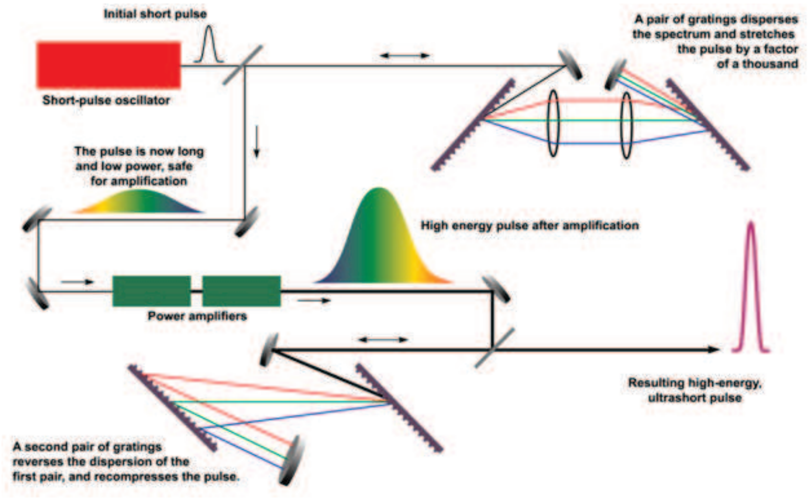

Figure 2.1: Detailed diagram of CPA, altered from Ref. [8].

using an optical fiber for spreading with parallel gratings for compression and was improved upon by perfectly matching the spreader and compressor in 1987. [7, 9]

With shorter incoming pulses come pulses with very large bandwidths. By dispersing the pulse with the spreader, the pulse becomes chirped, meaning that the many frequencies in the bandwidth are separated in time. The chirp is developed by a combination of self-phase modulation and group velocity dispersion. A more indepth discussion of Chirped Pulse Amplification is given in Appendix A. Through the development of Chirped Pulse Amplification, ultrafast lasers have moved to higher repetition rates, higher powers, and shorter pulse lengths.

2.2 Physical processes in laser irradiation

Femtosecond pulse lengths dictate the kinetics of melting and resolidification of target semiconductors. A more detailed review of the fundamental dynamics is available in Ref. [10]. Upon fs-pulse irradiation, the semiconductor experiences several regimes of excitation and relaxation, before returning to full equilibrium. The four regimes are 1) carrier excitation, 2) thermalization, 3) carrier removal, and 4) thermal and structural effects as detailed in Fig. 2.2. [10] Due to the nature of ultrafast pulses, we also describe the resulting differences when compared to shorter, nanosecond (1 ns = 10^{-9} s) pulses.

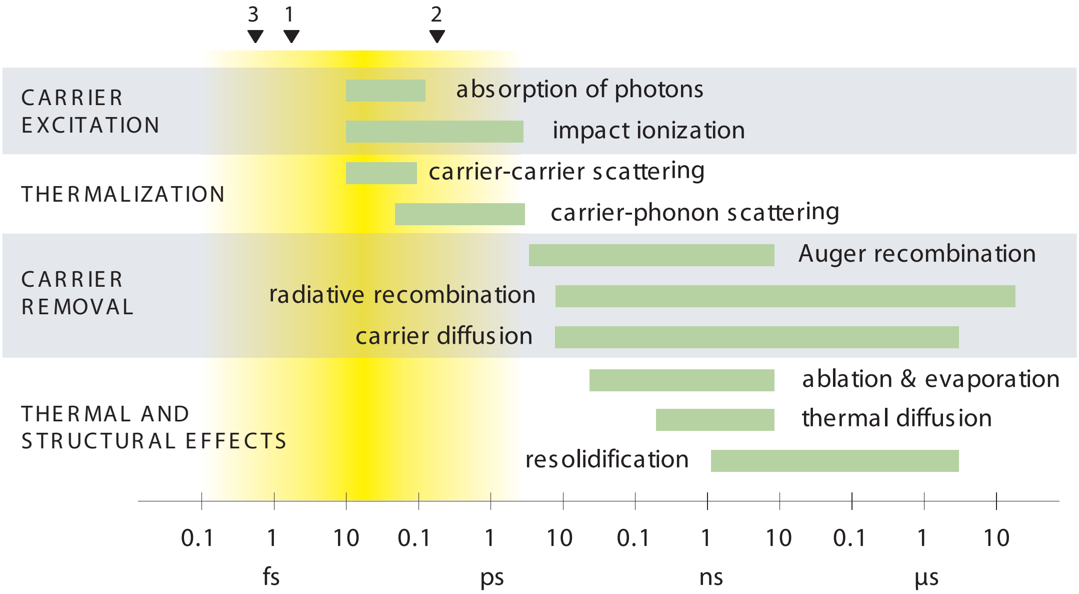

Figure 2.2: Four regimes of ultrafast excitation in semiconductors from Ref. [10].

Femtosecond-laser pulses generate large peak electric fields which are orders of magnitude larger than the 10^9 V/m coulomb fields that bind electrons to atoms. [11] Large peak pulse energies cause nonlinear absorption in short absorption depths from the irradiated surface, which limits the focal volume where laser energy is deposited.

The dynamics of sub-ps-pulse interactions with semiconductors is unique in two ways. First, the pulse delivers energy to the material on a timescale shorter than the electron-phonon coupling relaxation time. The incident pulse only delivers energy to the electrons, leaving the ions completely "cold." Thermal energy transfer to the lattice only takes place once the pulse is gone. Thus, decoupled optical absorption and lattice thermalization processes uniquely characterize sub-ps-pulse-semiconductor interactions. Second, extremely short pulse widths in time translate to very high peak intensities that can drive nonlinear and multiphoton absorption.

During multiphoton absorption electronic bonds in the irradiated sample are directly broken. This is a non-thermal process with minimal heating. Such cold ablation can be attained with non-ultrafast pulses but only by employing a deep UV wavelength. [12] Multiphoton absorption facilitates absorption in materials with low linear, optical absorption (i.e. wide band gap semiconductors) that are difficult to machine with traditional nanosecond lasers. [12] The sample surface absorbs the front part of the fs-laser pulse. The extreme electronic excitation creates a dense electron-hole plasma, which is responsible for the absorption and partial reflection of the remaining pulse. [13–15] The plasma then delivers energy to the lattice. Surface interatomic bonds are weakened due to the high degree of electronic excitation, and the lattice is disordered through cold atomic motion. The sample enters an extreme non-equilibrium state with a several thousand Kelvin electron gas inside a room-temperature lattice. [11] What happens post-absorption can vary dramatically, depending on the target material's relationship with pulse wavelength and energy. Three resulting regimes are possible: 1) non-thermal melting through an ultrafast phase transition, 2) thermal phase melting, and 3) ablation:

1. Non-thermal Melting: A pulse energy large enough to rip 10–15% bonded valence electrons and achieve a critical density of conduction band electrons (10^{22}

cm^{-3}) will induce a non-thermal ultrafast phase transition. [11]

2. Thermal Phase Melting: If the pulse energy does not cause such sudden disordering of the lattice, the plasma energy will spread via electron-phonon coupling to the lattice over several picoseconds. [10] This heat from the excited surface diffuses inward, raising the lattice temperature. If the solid temperature exceeds its melt temperature, a thin layer near the surface transitions to a liquid state, called the melt. The melt depth increases with laser energy.

3. Ablation: Large pulse energies cause boiling at the melt surface. The resulting superheating of the liquid phase and high nucleation rates of the gas phase eject material from the surface in a process known as ablation.

Specific experimental parameters, primarily laser wavelength and pulse length, determine the fluence thresholds for melting and ablation for a given material system.

2.2.1 Melting and resolidification

After irradiation, a thin molten layer forms atop the room temperature substrate. The corresponding heat gradient drives heat away from the molten layer and initiates a fast moving resolidification front, which advances from the substrate towards the molten layer. The time interval between irradiation and resolidification is several nanoseconds. [10]

The resolidification-front speed determines the crystal quality of the resolidified layer. For silicon, a front speed faster than the liquid to crystal relaxation rate ($\sim$15 m/s) will deprive atoms enough time to find their equilibrium positions, yielding an amorphous material. A slower resolidification front will cause a longer lasting molten phase and epitaxial regrowth with a crystalline resolidified layer. [16]

Higher laser fluences lead to longer melt durations and slower resolidification fronts. Laser pulse exposure just above the melting threshold causes the material to resolidify as an amorphous solid. At higher fluence thresholds, melting is typically followed by crystalline regrowth.

2.2.2 Ablation

The process of ablation occurs when the fluence of the laser light exceeds that of the ablation threshold. For fs-laser-matter interaction, the laser pulse duration is much shorter than the electron-cooling rate, which has been shown to be on the order of 1 ps. [17] With high laser fluences, energy from the surface of the material causes some of the surface melt to evaporate in the form of an ablation plume. Research into the ablation process has shed light on the mechanism. By modeling the fluidic movements of the melt, it has been shown that the ablation occurs from fragmentation of a supercritical volume expansion in a short time frame. [18]

When the laser fluence exceeds that of the ablation threshold, we can achieve laser-induced periodic surface structures (LIPSS). [19] For femtosecond-laser texturing, the LIPSS formed consist of semi-periodic nanometer- and micrometer-scale structures. [20–22] The LIPSS are independent of the crystal orientation and exhibit a wide range of feature sizes and shapes. The formation of LIPSS in the shape of ripples occurs when surface waves in the melt develop as the incoming light interferes with the scattered light off of the material. As more pulses impinge on the ripples, self-focusing occurs in the valleys and can result in larger structures that go deeper into the material. For this process, LIPSS are created that are dependent on the wavelength of the incoming femtosecond laser and the index of refraction of the host material that is being textured. [23]

When it comes to ablation, we see that femtosecond lasers can damage even the hardest of materials. [24] Because ablation is such a destructive process for the irradiated material, we can use ablation to our own advantage across industries. Ablation is one of the easiest ways to cut and scribe hard materials. Since fs-laser ablation acts on a faster timescale than the time it takes for the thermal energy to diffuse into other areas of a material, we can use ablation to act in very precise ways in three dimensions. We will discuss the positive attributes of fs-laser ablation in many applications in the section below.

Timescale comparison

Nanosecond pulses excite electrons in a distinctly different process than fs-excitation. When a ns-pulse delivers energy to a material, excited electrons transfer energy to the lattice during the time of the electron excitation. Electrons and the lattice thus remain in equilibrium throughout the excitation process. The ns-laser heats the solid to its melting temperature during the length of the laser pulse. [10] Ns-absorption processes are linear with a much larger absorption length than fs-absorption. Linear absorption can lead to deeper melt depths. Compared to the fs-laser case, the ns-induced temperature gradient between the molten layer and the solid substrate is smaller and distributed over a longer distance. Consequently, the melt duration is longer, and the resolidification front speed is slower, which for silicon typically yields a crystalline structure.

The longer ns-pulse widths translate to lower peak powers compared to fs-lasers. Operating at lower peak powers, ns-lasers ablate materials by a thermal process. [12] This thermal ablation causes a large heat-affected zone that may induce melt redeposition and shockwaves, leaving behind thermally-induced defects like cracks and chipping. [25]

2.3 Applications

There are a wide variety of applications when it comes to fs-laser processing of semiconductors. In this paper, we will explore three types of applications: (1) surface modification, (2) bulk modification, and (3) deposition techniques. We will focus on electrical and energy applications and not touch on the bioapplications due to the breadth of the disciplines covered. [26] Femtosecond lasers are also operated as material characterization tools, and many other studies detail their uses in femtosecond pump-probe spectroscopy [27,28], laser-induced breakdown spectroscopy (LIBS) [29], and surface-enhance Raman spectroscopy (SERS) [30].

2.3.1 Surface modification

One of the main applications of fs-lasers is surface modification. In this section, we first discuss texturing the surface for applications including light trapping and hydrophobicity. Next we discuss machining applications in which the laser is employed to scribe, dice, and drill through semiconductors. Lastly, we will discuss the use of femtosecond lasers to hyperdope, or dope beyond a material's equilibrium solubility limit.

Surface texturing

The surface structures made from femtosecond laser texturing of semiconductors can be applied to a variety of applications, including light trapping and hydrophobicity. Femtosecond lasers have been used to produce a wide variety of surface structures including conical peaks [11, 31], periodic gratings [32, 33], and ripples [34, 35]. Light trapping is most important when absorption is the main application, such as in a solar cell or photodetector. For this reason, light trapping has been studied mostly in silicon, as it constitutes the vast majority of solar cells and photodetectors produced. In order to maximize the light absorption for a device, light trapping takes advantage of the photons that are energetic enough (above bandgap) for the host material to absorb but have scattered from the surface and hence are unusable. The common solution to light trapping is to use an antireflective coating, usually silicon nitride, with a chemical texture, but that still leaves about 10% unabsorbed light. [36] It is for this reason, that using femtosecond laser texturing of silicon has become an important field of study.

By comparing many different types of texturing on silicon, research has shown that femtosecond-laser textured silicon has less overall scattering than chemically-textured silicon with silicon nitride. [36, 37] However, the internal quantum efficiency of the chemical texturing plus silicon nitride is still higher than the laser-textured sample, which shows that the texturing aids light trapping but also hurts the overall efficiency. A device optimization study has shown that laser-texturing silicon in SF_6 allows for the creation of thin film solar cells because more photons can be absorbed with a thinner absorption layer ($\sim$20 μm). [38] The study also found that the absorption from laser texturing approaches the theoretical limit for solar cell absorption, or the Yablonovitch limit, and have worked on making a solar cell with the laser texturing as a basis for the solar cell's light trapping. [38, 39]

In addition to light trapping, the same laser-irradiated silicon surfaces have been shown to be quite hydrophobic, with applications in biology and materials science. Femtosecond laser texturing of silicon in SF_6 yields micron-sized spikes, which many groups have used to increase the contact angle, which is the angle formed by a liquid placed on the surface of a material. Studies first showed that by varying the laser fluence, it was possible to control the resulting contact angle and hence the hydrophobic properties of the underlying silicon. [40] Through subsequently layering molecules, like fluoroalkylsilane, on the laser-textured silicon surface, it was later shown that the surface molecules increased the contact angle farther, making the surface even more hydrophobic. [41] With both light trapping and hydrophobic properties, laser-textured silicon yields a surface that can be used in a variety of applications—many of which remain unexplored.

Machining

Ultrafast lasers are one of the highest performing tools to perform surface modification machining. Micromachining refers to the creation of micron-scale features like holes, lines, and grooves within and on the surfaces of materials. Ideally, these features are produced with minimal peripheral damage. Historically, laser micromachining in semiconductors has been carried out with diode-pumped solid state or excimer lasers with ns-pulse durations. [1, 12] However, the effects of thermal diffusion that stem from ns-laser machining place a lower limit on the length scales that can be machined. Furthermore, thermal diffusion can lead to poor machining quality and a large heat-affected zone which can induce detrimental stresses, cracks, molten layer recast, and slag. [1]

Femtosecond lasers offer a new paradigm in machining quality with high spatial resolution and minimal thermal damage. With their ultrashort pulse lengths, fs-lasers can controllably deposit energy to a material on a time scale faster than ps-electron-phonon coupling processes. [42] Heat diffusion into the machined-area periphery is minimal and leaves behind a small amount of molten material. [25] This small heat affected zone contains a low level of the thermal defects, which are common in ns-laser processing like cracking and chipping.

Compared to traditional Q-switched solid state lasers and nanosecond lasers, fs-lasers have an overall higher cost of ownership. As such, industrial adoption of fs-lasers has been limited to high value-added applications where high precision is required. [1] Picosecond lasers land in the middle, delivering a machining quality that is less precise than fs-lasers but suitable nonetheless for many applications. [1] Their lower cost of ownership has made ps-lasers a preferred candidate for most commercial applications. In this section, we will discuss three main aspects of machining that are used in industrial applications: scribing, drilling, and dicing.

Scribing Laser scribing is the process in which a focused laser is scanned across a material surface to form a continuous line or groove, without completely vaporizing through the material. Laser scribing is used to shape a variety of brittle semiconductors across industries. Here we discuss two applications in the photovoltaic industry: scribing of thin film photovoltaic modules to achieve series interconnections and edge isolation of crystalline silicon modules to remove shunt paths.

Scribing thin film solar photovoltaic modules is one particular application that can benefit from the small heat affected zones associated with fs-laser ablation. A thin film solar module consists of hundreds of series-connected cells, or mini-modules, atop a glass substrate. [43] Mini-modules limit module ohmic losses and. are interconnected by multiple steps of depositing and scribing an individual thin material layer. [44] Directly after each material layer is deposited, it is scribed before the next layer is deposited. The complete scribing process is shown in Fig. 2.3. [44] This scribing process series connects the mini-modules as desired, but it also forms detrimental electrically inactive dead-zones between adjacent mini-modules. Reducing dead zone size, which is fundamentally limited by the area of each scribe, is critical to increasing overall module efficiency. [44]

Due to their precision, repeatability, and small heat affected zones, pulsed lasers are well suited to achieve effective scribing and minimum-dead zone size. Today most thin-film PV manufacturers use ns-lasers for their scribing processes. [44] In the last decade, many groups have demonstrated that ultrafast lasers deliver better scribing performance than ns-lasers for thin film material layers, including CIGS [45–47], CdTe [43], and ITO [48]. Ultrafast scribing inflicts smaller thermal effects, which minimizes dead zone size, laser-induced defects, and unwanted ablation-induced redeposition on the scribed channel walls that leads to electrical shunts. While ultrafast scribing has been shown superior performance to ns-scribing, industry adoption has been limited by the ultrafast laser's higher cost, lower output frequency (reducing throughput), and Gaussian profile (which can lead to non-uniform ablation relative to a top hat profile). [44, 49]

Another photovoltaic application of scribing is edge isolation. Most crystalline silicon photovoltaic manufacturers form cell pn-junctions by coating a p-doped silicon wafer with an outer n-doped layer via phosphorous diffusion. The edge surface n-doped layer may form an unwanted electrical connection between the front and back contacts of the device. This shunt short circuit path allows the flow of an internal current, robbing photogenerated current from an external load. Edge isolation is the process of forming a continuous groove through the n-edge layer that electrically isolates the shunt path.

Various methods, including lasers, plasma etching, chemical etching, are used to achieve edge isolation. [50] Photovoltaic manufacturers employing laser-grooving typically use green or UV ns-lasers, but scribing with ultrafast lasers offers several advantages. [44, 50] The narrower and closer to the edge a groove is, the more cell active area will be preserved which leads to higher overall device efficiency. [12] Furthermore, precisely forming the groove without unwanted effects, like edge surface roughness or microcracking, gives rise to higher processing yields and long lasting module lamination and reliability. Several studies of edge isolation using high power ps-lasers have shown cleaner isolation grooves compared to traditional ns-processing. [51–54] Simulations also suggest such ps-processing can be scaled to industry levels at throughputs faster than current industry standards. [53]

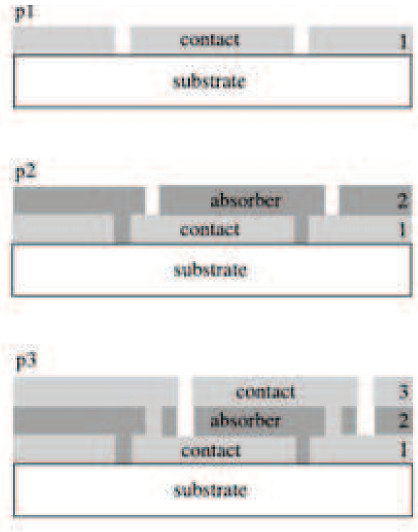

Figure 2.3: Scribing diagram from Ref [55].

Drilling Another application of fs-laser machining is drilling, or milling, materials for industrial applications. After the formation of LIPSS within the laser focal volume, as shown in Fig. 2.4, we see that the introduction of more pulses, on the order of thousands, leads to drilling a hole with relatively vertical sidewalls. [17] Although most work in this field has been done on metals, the method can be extended easily to semiconductors. [56] Due to fs-laser ablation not involving thermal effects, we can achieve much better micromachining characteristics than with other methods. In comparison to nanosecond lasers, femtosecond laser drilling yields much more precise holes with less residual damage or redeposited material. [57]

This circular ablation can be performed on a wide variety of materials, including silicon and titanium nitride. In silicon, we see that it is the lack of a liquid phase

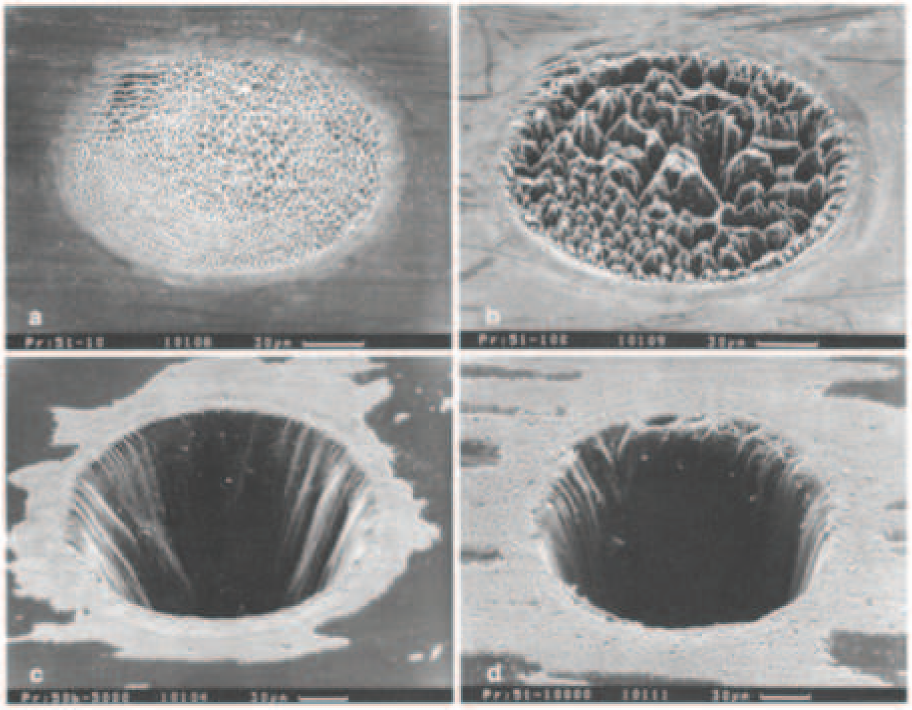

Figure 2.4: Scribing diagram from Ref [58].

created with fs-lasers that leads to much better hole creation. For ns-lasers, a liquid phase is created and leads to unstable drilling and ultimately produces a poorer quality material. [17] In titanium nitride (TiN) evaporated on silicon, TiN can be drilled efficiently with the fs-laser. With additional pulses, the underlying silicon can also be structured. [58] It is interesting to note that the drilling can work with a power just above the ablation threshold and that the depth of the hole is linearly dependent on the number of pulses applied. [58] This linear dependence shows that it is the overall number of pulses applied that determine the overall hole depth, and that it does not take large peak powers for drilling in semiconductors to occur. Because the underlying silicon was structured as the number of pulses (and hence the depth of the hole) increased, this method shows that multiple materials in a stack can be drilled with a femtosecond laser.

Dicing Ultrafast lasers are not only used to machine grooves or holes in semiconductors, but can also cut, or dice, straight through the same materials. Ultrafast dicing is being investigated to cut thin silicon substrates in the microelectronics industry.

In the microelectronics industry, dicing is used to separate the many individual integrated circuit chips that are written on a lithographically processed wafer. Historically the microelectronics industry has used thick wafers (i.e. greater than 150 μm) that could be effectively diced with diamond-coated wire blades that cut via mechanical abrasion. Now the industry demands 50 μm or thinner wafers that could crack, chip, or delaminate in response to mechanical stress from wire dicing. Non-contact laser dicing, however, can effectively dice these thin wafers with higher precision and throughput. Laser dicing offers additional benefits like reduced dice tool ware, reduced dice contamination, and the ability to curvilinearly form rounded corners on individual dies, which increase die mechanical strength. [59]

Studies have found that laser dicing cut quality is dependent on pulse width. [59] Poor-cut quality is largely due to thermal melting and molten layer redeposition for pulse widths larger than 1 ns. [59] Recognizing the minimal thermal effects of ultrafast processing, many groups have investigated high quality dicing with fs-lasers. [60–62] Furthermore, small cut lines from ultrafast dicing are advantageous in that they allow for more circuit chips to be placed on a lithographically processed wafer (produced at a fixed cost), reducing the average cost per chip. Different fabrication procedures like the use of line foci or employing double pulses have been explored to find optimal conditions that minimize cut widths and maximize cutting speed. [62, 63] Currently, the major barrier to wider industrial adoption of fs-dicing is concern about low fs-laser repetition rates and dicing throughput. [59]

Hyperdoping

One unique application of femtosecond-laser processing of semiconductors is the ability to hyperdope target materials. Hyperdoping refers to doping semiconductors at concentrations beyond their equilibrium solubility limit without forming compounds or secondary phases. [64, 65] Doping can be achieved through the introduction of dopants, either in the gaseous environment or as an evaporated thin film, while target semiconductors are laser-processed as described above. The fundamental mechanism behind hyperdoping is that molten liquid phases can host more dopants than equilibrium solid phases. Hyperdoping has also been achieved by ion implanting samples and subsequently using a nanosecond laser to remelt the sample and recrystallize the lattice. [66] The hyperdoping process was originally developed by irradiating silicon with a train of amplified fs-laser pulses in the presence of a wide variety of dopant precursors. It has been shown that silicon can be hyperdoped to more than 1 at. % sulfur in a 300-nm thin layer. [67, 68] In addition, the process produces semi-periodic surface textures that have excellent anti-reflection and light-trapping properties as shown in Fig. 2.5. At a high chalcogen (S, Se, Te) doping concentration, femtosecond laser-doped silicon exhibits near-unity light absorptance from the ultraviolet to the near infrared, which is far beyond silicon's bandgap of 1.1 μm (Fig. 2.5, right). [69,70]

Using fs-laser fabrication, research has shown the ability to incorporate dopants at concentrations thousands of times above the solid solubility limit. [69] Femtosecond-

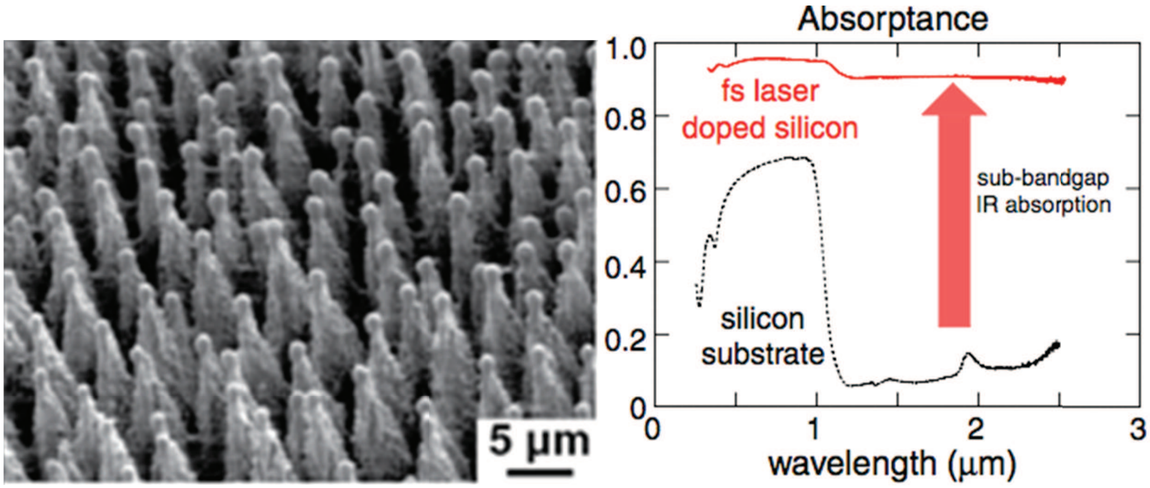

Figure 2.5: Femtosecond laser irradiation of silicon in SF_6 shows surface structures (left) and enhanced absorbtion (right) from Ref [71].

laser hyperdoping achieves this through a process called solute trapping. [16,72] Laser pulses that have energies greater than the melting threshold transform the surface into a molten layer, which enables dopants to diffuse in. As the deposited energy diffuses into the substrate, the molten layer resolidifies with a speed greater than the dopants can diffuse out (> 1 m/s), which obtains supersaturated concentrations. [73] Such high dopant concentrations should yield an intermediate band in the semiconductor bandgap. [74] In addition to doping, the creation of conical surface structures as discussed previously aids in light-trapping for the hyperdoped materials, and work in silicon has recently identified laser parameters for independently tuning the hyperdoping and texturing processes. [11]

The work with ion implantation and subsequent nanosecond laser melting has been extended to a variety of transitions metals, where an infrared silicon photodetector hyperdoped with gold has been successfully achieved. [75] This ns-hyperdoping method produces hyperdoped layers with better crystallinity versus fs-produced hyperdoped layers, albeit at lower dopant concentrations with less sub-bandgap absorption. The method has been used to produce silicon-based photodiodes with a large response to photon energies down to 0.7 eV, which is below that of commercially-available silicon-based photodiodes which are limited by silicon's 1.1 eV bandgap. [76] SiOnyx, Inc. is currently commercializing infrared photodetectors for military and consumer electronic applications. [77]

Fs-hyperdoping has also been recently demonstrated in larger bandgap oxide semiconductors TiO_2 and ZnO. Both demonstrations have shown the incorporation of defect atoms into the oxide lattice. [78, 79]. In the ZnO case, antimony was even incorporated in a single crystalline portion of the laser-modified surface region. [80] By utilizing both the hyperdoping and surface texturing process of femtosecond laser processing, many new fields can be explored across many material platforms.

2.3.2 Bulk modification

After discussing many applications in surface modification, we now will move onto techniques using femtosecond lasers to modify the bulk of the material. The two applications we will discuss in the next section will cover (1) annealing to crystallize the lattice and (2) direct patterning. As with the surface modification, many different groups use femtosecond lasers to fundamentally change the bulk properties of a material and ultimately create substances that cannot exist using other known methods.

Ultrafast bulk annealing

Semiconductor annealing refers to heat treating a material to alter its microcrystal structure and resultant physical properties. Annealing traditionally refers to a series of equilibrium kinetics processes that heat a material beyond its melting temperature, maintain the temperature, and subsequent material cooling. Here we focus on highly non-equilibrium ultrafast annealing, which is used to improve crystal structure and material performance.

The microelectronics and photovoltaic industries have historically used furnace thermal annealing and rapid thermal annealing to improve the crystallinity of polysilicon grown from deposited amorphous silicon. [81] However, because they operate via bulk heating, both methods cannot selectively heat a specific layer within a multilayer stack, places constraints on the type of material layers and substrates that can be used. To overcome these limitations, the microelectronics industry has begun using microsecond-annealing, via flash lamps or continuous wave diode lasers, to achieve selective heating and to activate shallow dopants following host lattice ion implantation damage. [82]

Laser annealing on ultrafast time scales allows for even more precision in selectively heating a stack of materials. Aside from being confined to a more precise focal volume, ultrafast crystallization is advantageous in that it can be done while simultaneously ablating a surface. This stems from the nonlinear absorption and non-equilibrium light matter interaction discussed above.

The low fs-ablation threshold has been exploited to demonstrate simultaneous crystallization and surface texturing of 1.5–2.5 μm thick a-Si films deposited on glass. [83] Further studies have characterized the effect of laser parameters on resulting spike formation, absorption, and crystallinity on similarly processed amorphous samples irradiated in air and water environments. [84] One study reports that the crystallization forms a blend of hydrogenated nanocrystalline (nc-Si:H) and a-Si:H that improves material stability in the face of light degradation. [84] The high amount of resulting structural defects, however, currently limits this technique from being deployed in photovoltaic applications.

Crystallization with picosecond lasers has also been recently explored to potentially make a-Si:H/nc-Si:H micromorph tandem cells. [85] Such a tandem cell is shown in Fig. 2.6a. In this process, a deposited a-Si:H layer is partially converted to a polycrystalline layer via ps-laser annealing as shown in Fig. 2.6b. Such a fabrication procedure would simplify and complement the current multistep chemical vapor deposition growth process.

Direct patterning

One of the most transformative fs-laser applications is to utilize the two-photon process to micromachine materials in the bulk of the material yielding structures in three dimensions (3D). [86] Femtosecond laser processing allows for the direct patterning of a variety of materials and the creation of large structures in 3D. Micromachining was first developed in transparent materials, such as SiO_2. [87, 88] Due to using two- or multi-photon processes, most research in micromachining has focused on polymers and soft materials.

However, it has been shown that it is possible to pattern TiO_2 by irradiating

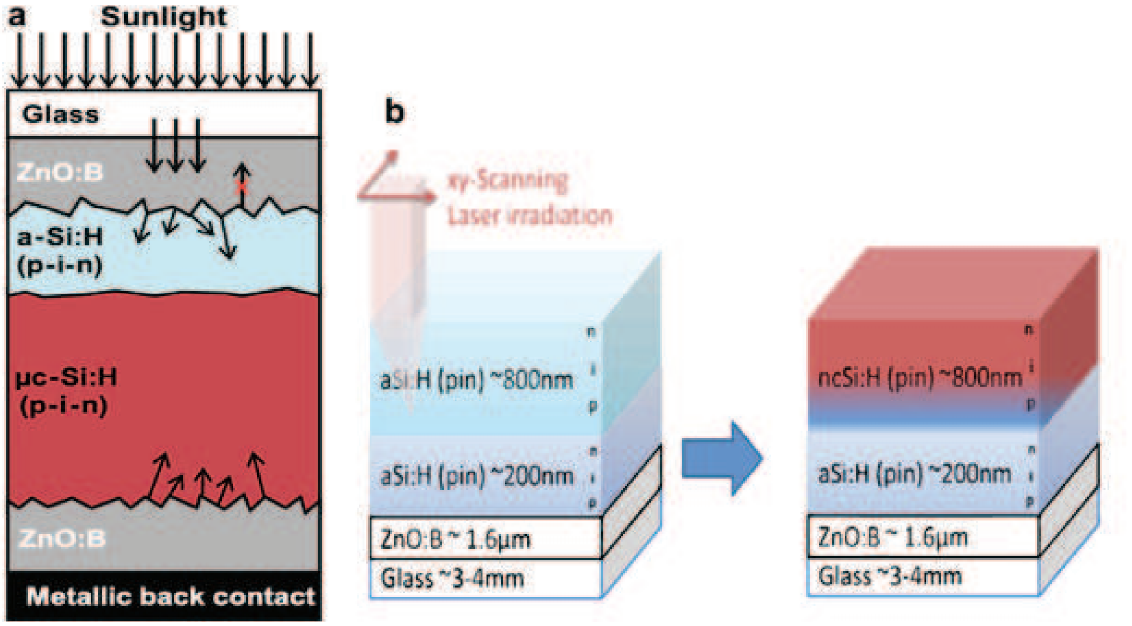

Figure 2.6: Bulk annealing from Ref [84].

a photosensitive sol-gel TiO_2 with below bandgap light. The incoming light initiates a multiphoton process that is able to break down the resist. The resulting structure can be quite complex, such as the woodpile shown in Fig. 2.7. [89] Silicon has also been micromachined with femtosecond lasers. Research has shown that femtosecond lasers have a reduced heat-affected zone when compared to nanosecond lasers, which translates into less induced stress. [90]

Another use of micromachining in semiconductors makes use of the proliferation of 3D-patterened polymers by coating the resulting polymer 3D structure with semiconductors to form 3D semiconductor patterns. Recently, chemical vapor deposition was used to deposit a thin silicon layer over an underlying 3D polymer pattern to create a 3D silicon woodpile photonic crystal structure. [91] By coating semiconductors onto polymer patterns, we can access a much larger range of materials and structures that are normally too complex to make from mainstream semiconductor processes.

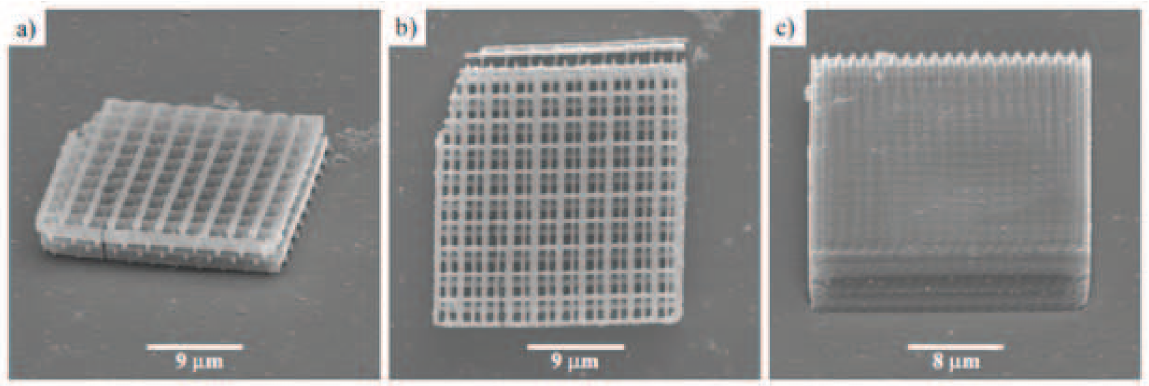

Figure 2.7: Micromachining of TiO_2 from Ref [89].

2.3.3 Deposition techniques

Lastly, we will cover various applications in deposition techniques that make use of femtosecond lasers to ablate various materials and then redeposit the ablated material onto additional substrates. By altering the target material and the surrounding environment that the ablation occurs in, many different types of semiconductors can be formed. Here, we will discuss (1) nanoparticle formation from the ablated particles, (2) pulsed laser deposition, which creates films from the ablated particles, and (3) laser-assisted growth, where the ablated particles are used as seed material to deposit other materials. In each of these cases, femtosecond laser ablation helps to create materials that other deposition techniques struggle to make with high precision.

Nanoparticle formation

Femtosecond laser irradiation of semiconductors beyond the ablation threshold produces ablated particles and we can utilize this material in the form of nanoparticles. [92] In order to gather the nanoparticles, the setup usually involves positioning a target material at a 45 degree angle in relation to the incoming laser beam with a collection substrate positioned parallel to the target material. [93]

For silicon, nanoparticles can be formed in a vacuum [94] or surrounded by a background gas, such as H_2 [21]. It has been shown that the ablation of silicon nanoparticles has a large size distribution that cluster into aggregates and webs that are 5–300 nm in size. [21] By changing the background gas to H_2S, the size of the ablation plume cone also changes. The phase of the formed nanoparticles can either be crystalline or amorphous, which is determined by the cooling rate of the ablated silicon in the liquid phase. When a background gas is present, the gas forces some nanoparticles to cool through a thermal process and hence not go through a non-thermal phase transformation. [21] For silicon ablated in a vacuum, the nanoparticles cool at a much faster rate and do not have the background gas to compete with, which leads to only nanoparticles and clusters and not the formation of webs. Hence, the resulting nanoparticles are dependent on many factors in the ablation and subsequent cooling process.

Pulsed laser deposition

By extending the process of nanoparticle formation, we can make thin films of materials through pulsed laser deposition (PLD). Through a similar setup as for nanoparticle formation, complex materials can be deposited onto a variety of substrates. [95] The main advantage of PLD over other deposition techniques is its ability to repeatedly grow thin films with precise and complex stoichiometries.

The most common use of PLD is for deposition of thin films. In order to deposit an oxide, the femtosecond laser is used to excite plasma on the target material and then the nanoparticles fly off onto a flat substrate. To deposit SnO_2, the amount of background oxygen gas was instrumental in producing high quality epitaxially-grown films, even though they started with a target that already contained the correct amount of oxygen, SnO_2. [96] Another example of thin film PLD is the creation of CdS, where it was shown that the substrate used, between silicon and quartz, determines the quality and grain size of the material deposited. [97]

A variety of photovoltaic absorber materials (e.g. CdTe, ZnS) and transparent conductive electrode materials (ZnO, ITO) have been produced with PLD. [55] There is a an especially large amount of activity in using PLD to test a variety of up and coming higher mobility p-type transparent conductive oxide materials for thin film photovoltaic and thin film transistor applications. [98] Repeating these results at larger scale in a low cost PV industrial setting is unlikely, however, due to the low throughput and nanoparticle ejection problems associated with PLD. [98, 99]

Laser-assisted growth

The use of lasers to help start nanowire growth is a relatively new field and has been applied to a variety of semiconductors. Nanowire growth was first discovered using a nanosecond laser acting on a $Si_{1-x}Fe_x$ target, where they found a large size distribution of the resulting nanowires. [100] The growth mechanism proposed that the formation of the nanowires occurs while the ablated nanoclusters are still in the liquid phase and that the length of the nanowire growth is determined by the time that it takes for the nanowire to be pushed out the "hot reaction zone" by the flowing carrier gas in the chamber. [100] The nanowires created consist of a single crystalline Si core with a SiO_x sheath on the outside and are on the order of tens of nanometers. It has also been shown that it is possible to extend their method to other materials, such as germanium, but unlike the Si nanowires, the Ge nanowires tend to have no amorphous outer shell and have a nanocluster at the termination end, showing that the nanowire formation is a complicated procedure and is still not completely understood for all materials.

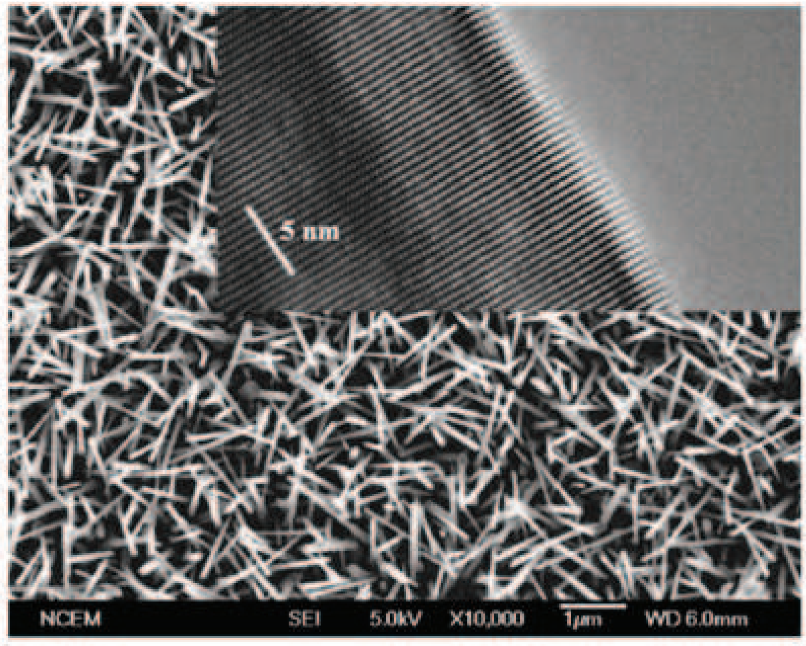

Figure 2.8: Laser-assisted growth from Ref [101].

By moving to femtosecond lasers, researchers found it was possible to apply this process to oxides. Using a ZnO target, they showed it was possible to control the size distribution of the nanowires due to the lack of overall thermal effects and smaller particulate creation with the nanoparticles flying off of the target. [101] They were also able to control the photoluminescence properties by changing the ambient oxygen partial pressure parameters. [101] They used a ZnO target and focused the laser inside the growth chamber with oxygen flowing. By using a femtosecond laser instead of the nanosecond laser used prior, there is no real melting in the ablation process, and they use Coulomb explosion to produce precise nanowires that have a small size distribution. With the femtosecond lasers, there is less particulate formation, leading to a superior nanowire product. [101] The nanowires are shown with a TEM insert showing their crystallinity in Fig. 2.8. By applying these methods to other materials, it should be possible to grow various materials and control their size and makeup.

2.4 Conclusion

In this chapter, we present the various applications of femtosecond laser processing on many different types of semiconductors. We show that the femtosecond laser leads to finer structure formation and more precise machining when compared to the ns-laser regime, which can be utilized in a variety of applications. In addition, we show that ultrafast lasers can be used as the basis for a few deposition techniques. With advances in how femtosecond lasers operate, we believe that they will be used even more in the coming years as the applications become more diverse and the lasers become smaller and more cost-effective.

CHAPTER 3

FEMTOSECOND-LASER FORMATION OF NANOSTRUCTURED TIO_2 AND TIN

In this chapter, we use femtosecond laser irradiation of titanium metal in an oxidizing environment to form a highly stable surface layer of nanostructured amorphous titanium dioxide (TiO_2). We study the influence of atmospheric composition on these surface structures and find that gas composition and pressure affect the chemical composition of the surface layer but not the surface morphology. Incorporation of nitrogen is only possible when no oxygen is present in the surrounding atmosphere.

3.1 Introduction

Femtosecond laser pulses provide a way to simultaneously structure and change the chemical composition of a number of materials, including titanium. [17,102,103] Laser structuring of titanium surfaces has been investigated because the topography of the titanium surface contributes to its biocompatibility [104], tribology, and hydrophobicity [105]. Femtosecond lasers have been used to produce a wide variety of surface structures on titanium including conical microstructures [106], periodic gratings [33], and nanoscale pores [107].

Laser processing also makes it possible to insert nitrogen and oxygen atoms into titanium while creating surface structures. [108, 109] Experiments involving titanium surfaces irradiated by nanosecond lasers show that the surrounding gas atmosphere can have a large impact on the surface chemical composition and the surface morphology. [110]

Because titanium, known for its durability, mechanical properties, and stability, is used in many biomedical applications [111], the effect of laser irradiation on biocompatibility is particularly important. While surface structures enhance cell-adhesion [112], the chemical composition of structured titanium surfaces also contributes to their biocompatibility. For example, the biocompatibility of titanium is improved by a thin layer of TiO_2 on the surface of a titanium implant. [113] Nitridation of titanium also has applications in biomaterials and microdevices for improvements in wear resistance and hardening. [111]

Although a high degree of control over femtosecond laser-formed titanium surface morphologies has been developed, the chemical composition of the resulting films has not been studied in detail. In this work we investigate the influence of oxygen and nitrogen gas composition on the surface morphology, chemical composition, and stability of femtosecond laser irradiated titanium surfaces.

3.2 Experimental Procedure

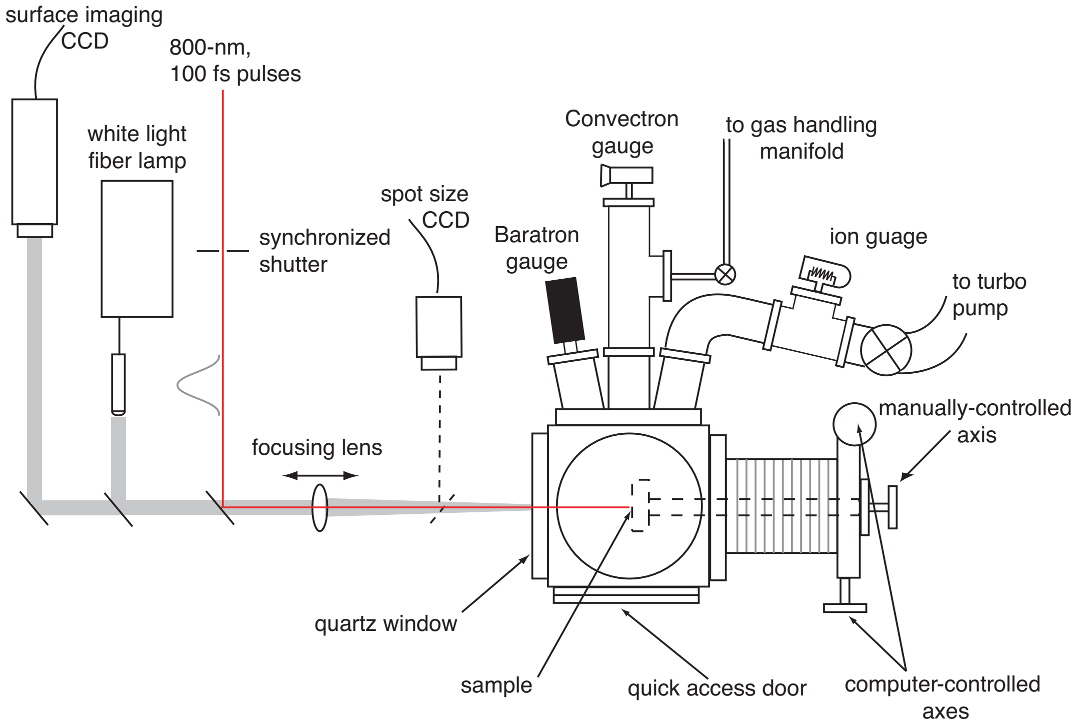

Figure 3.1: A schematic diagram of the fs-laser hyperdoping apparatus using a stationary laser beam and two-axis stepper motors to translate the sample.

We produce samples by irradiating a 99.99% titanium plate with a 25–33.33-Hz train of 100-fs, 805-nm laser pulses from an amplified Ti:sapphire laser, as shown in Fig. 3.1. The pulses have a fluence of 2.5 kJ/m^2 and are polarized in the x direction (x-y axes shown in Fig. 3.3). [69] We mount the samples on an $x-y$ stage in a stainless steel chamber that is evacuated to less than 0.1 Torr and then filled with a background gas. To irradiate the sample, we raster scan in the x direction and step in the y direction at the end of each row, uniformly exposing each spot on the sample to 50 laser pulses. The resulting sample is shown in Fig. 3.2.

We take images of the samples with a Zeiss Ultra55 scanning electron microscope

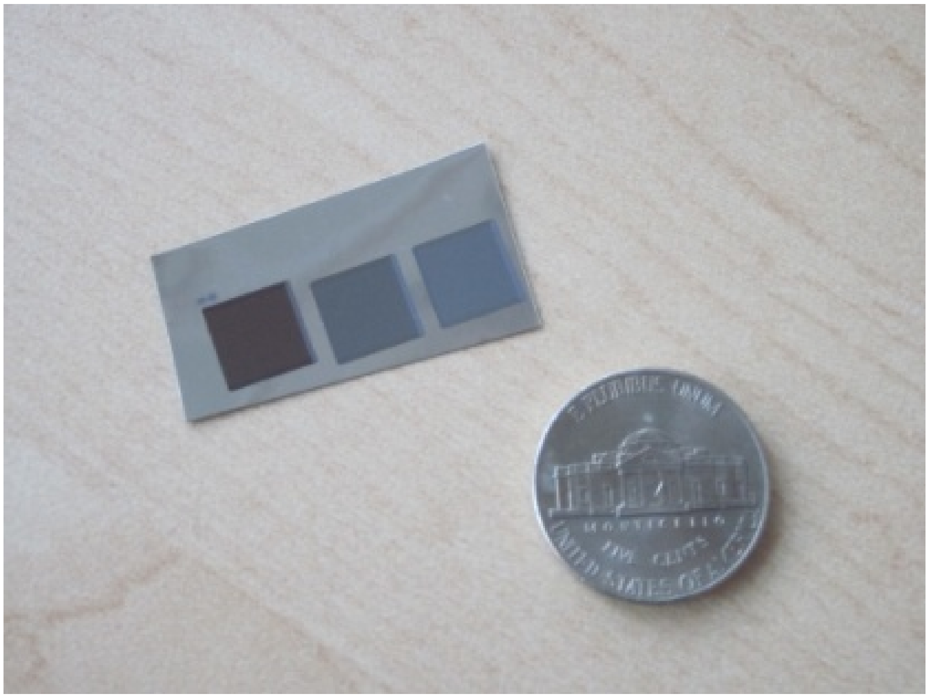

Figure 3.2: Laser-irradiated titanium metal with three 1-cm^2 areas. The samples were irradiated in 100 Torr of O_2 (left), air (middle), and N_2 (right).

(SEM) with a beam energy of 2 keV. We perform elemental analysis using X-ray photoelectron spectroscopy (XPS), which we collect on a Surface Science SSX-100 ESCA spectrometer. We use Ar+ sputtering for cleaning and depth profiling analysis at 2.7 keV. We collect survey spectra with an 800-nm spot size at 1 eV per step and high-resolution scans with a 300-nm spot size at 0.065 eV per step. We then perform XPS peak fitting using Casa XPS, and peaks are fit with Shirley background-corrected Lorenzian functions.

We also collect X-ray diffraction data (XRD) on a Bruker D8 Discover. The XRD experiments are performed on samples made from a 450-nm thick layer of titanium, evaporated onto a glass slide to minimize background from the unstructured underlying titanium and then irradiated with the same conditions detailed above.

We collect Raman spectroscopy on a Renishaw inVia microscope using an excitation wavelength of 633 nm, produced by a 5-mW, s-polarized Helium-Neon laser. We record the Raman spectra through a 50X microscope objective which is projected onto a thermoelectrically cooled, charged-coupled device (CCD) array using a 1200 groove/mm diffraction grating.

We collect electrochemistry data using a CH Instruments Electrochemical Analyzer CHI600D. We use a three-electrode setup with the untreated and treated titanium surfaces individually isolated as the working electrode, a BASi Ag/AgCl reference electrode, and a Pt coil counter electrode. We fill the electrochemical cell with an electrolyte, BioWhittaker Hanks' Balanced Salt Solution (HBSS), which is purged with argon for 60 minutes before use. All measurements are performed at room temperature.

We take reflectivity measurements with a Hitachi U-4100 spectrophotometer with a $BaSO_4$ integrating sphere.

3.3 Results and Discussion

Scanning electron microscopy (SEM) images of the films irradiated with a total atmospheric pressure of 100 Torr (Fig. 3.3) show laser-induced periodic surface structures (LIPSS) [71] that do not vary with the atmospheric composition of oxygen and nitrogen. The lines of the grooved pattern are oriented along the y direction, perpendicular to the laser polarization. This grooved pattern of the LIPSS is expected for near-damage-threshold laser fluences and multiple laser pulses. [114] The formation of LIPSS on metals has been attributed to the interference of the incident laser light

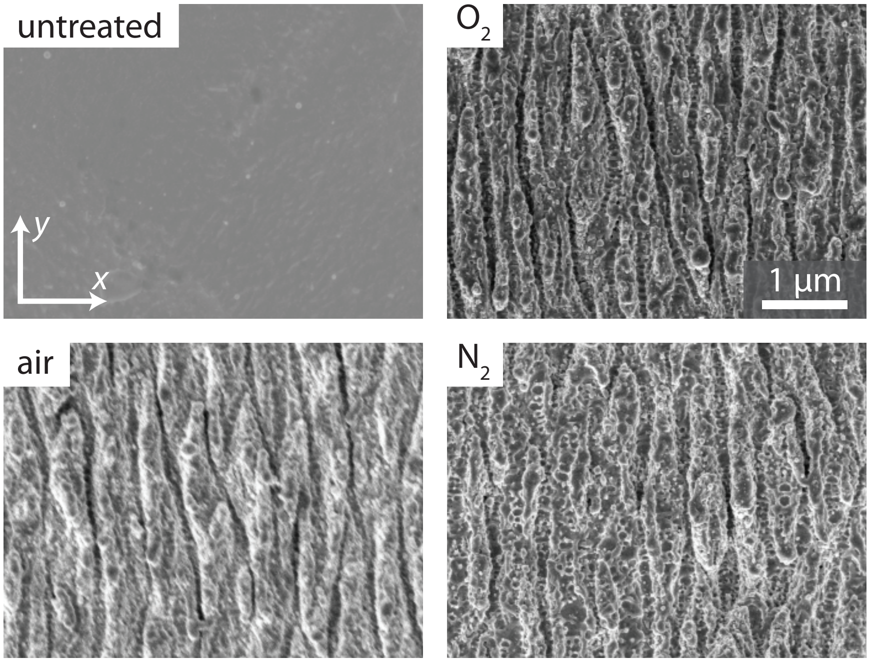

Figure 3.3: Scanning electron micrographs of titanium metal surface before (untreated) and after laser irradiation in the ambient gases shown, with a total pressure of 100 Torr in each case. The air mixture consists of a 1:4 ratio of O_2:N_2.

with excited surface plasmon polaritons. [19] Varying the total pressure of oxygen and nitrogen between 0.01 and 500 Torr does not change the surface morphology of the titanium structures. The same surface structures are visible after irradiation with 1, 10, or 50 laser pulses, regardless of the chemical composition of the background atmosphere.

Fourier transformations of the periodic surface structures confirm that samples formed in different atmospheric conditions all have a periodicity of 268 ± 15 nm. The periodicity of the surface grating formed from the interference between the incident laser light and excited surface plasmon waves is λ/n where λ is the wavelength of the incident light and n is the index of refraction. [115] The index of refraction of titanium at 805 nm is 2.883, producing a periodicity of 279.2 nm, in agreement with the measured periodicity of 268 ± 15 nm.

The X-ray photoelectron spectra (XPS) in Fig. 3.4 show that the ambient gas composition and pressure affect the chemical composition, and hence the physical properties, of the titanium surface structures. Surfaces irradiated in atmospheres containing only oxygen show significant amounts of only titanium and oxygen with more oxygen incorporated than in the untreated films. The films were measured after argon sputtering to remove surface atoms and reveal subsurface composition. The chemical shift of the Ti 2p peaks, shown in Fig. 3.4b, can be used to identify the oxidation state of the titanium atoms. The sample structured in 100 Torr oxygen has Ti $2p_{3/2}$ and Ti $2p_{1/2}$ peaks at 458.7 and 464.6 eV respectively, which correspond to Ti^{4+}, the oxidation state found in TiO_2, as seen in Fig. 3.5.

TiO_2 forms as a native oxide on titanium metal so we compare our results to

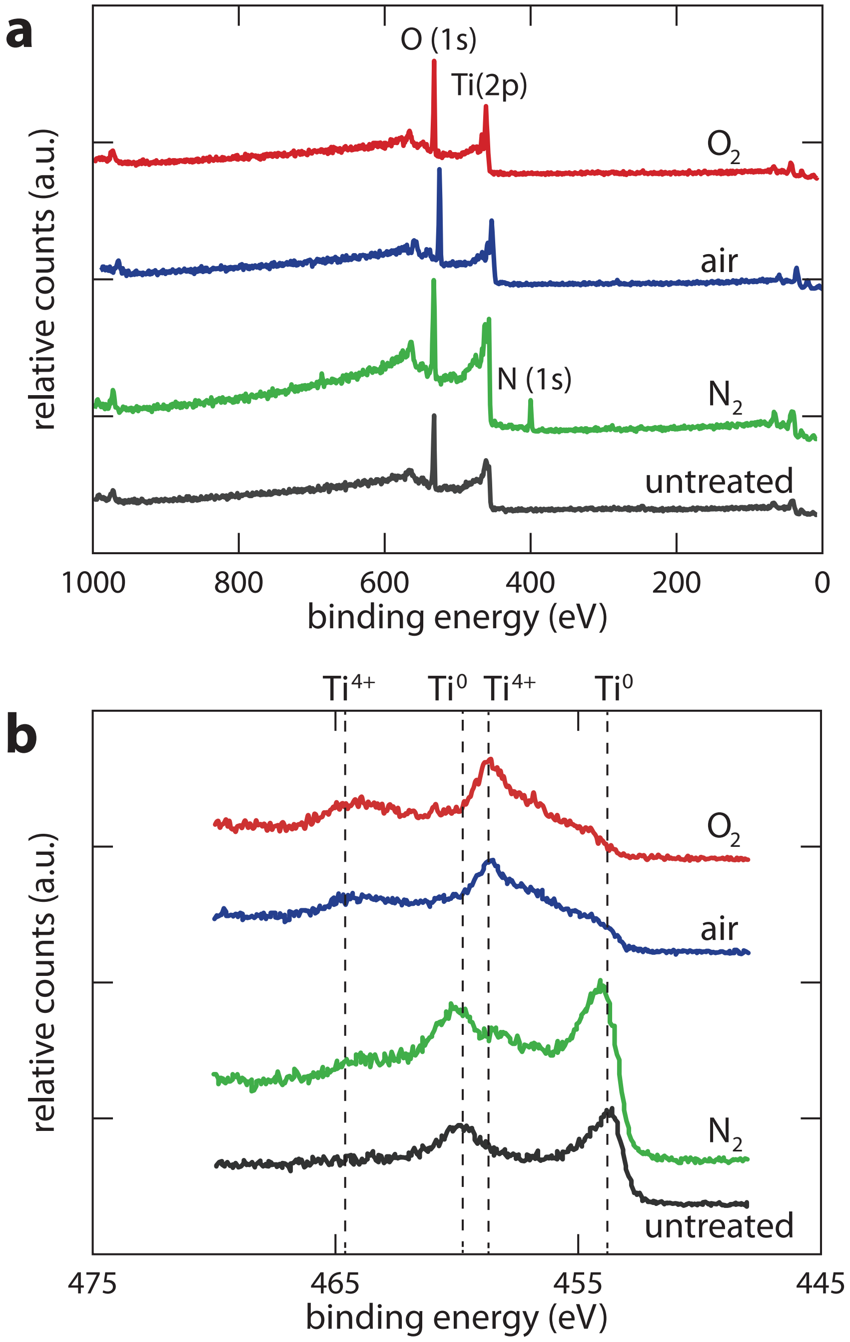

Figure 3.4: (a) X-ray photoelectron spectroscopy (XPS) of untreated titanium and laser-structured samples. The samples were Ar+ sputtered for 10 minutes immediately before measurement. (b) High resolution XPS of the Ti (2p) region of untreated and laser-structured titanium. The samples were Ar+ sputtered for 20 minutes before measurements.

an argon sputtered, untreated titanium sheet. The untreated titanium control has Ti $2p_{3/2}$ and Ti $2p_{1/2}$ peaks at 453.8 and 459.8 eV, which correspond to metallic titanium and confirm that the argon sputtering treatment is sufficient to remove the native oxide layer. The O:Ti ratio for a film structured in 100 Torr O_2 is 2.3 before argon sputtering treatment and 1.9 after 10 minutes of sputtering, which shows that the sputtering preferentially removes oxygen atoms. To quantify the bulk reduction caused by the argon ion sputtering, we also compared the laser-oxidized samples to a sputter deposited TiO_2 thin film. The sputter-deposited TiO_2 film is slightly more reduced following the argon sputtering treatment than the TiO_2 films formed by irradiating in oxidizing atmospheres after the same treatment. This may indicate that the sputter deposited TiO_2 film is thinner than the irradiated films. This observation, combined with the predominant Ti^{4+} oxidation state, shows that laser irradiation of titanium metal in an oxidizing atmosphere forms a surface layer of TiO_2. Due to the bulk reduction caused by sputtering, it is difficult to quantify the presence of additional titanium oxidation states in the laser-structured samples. While predominantly TiO_2, it is possible that the samples also contain smaller amounts of the less oxidized Ti_2O_3 or TiO.

As shown in Fig. 3.4a, titanium surfaces irradiated in a nitrogen atmosphere contain titanium, oxygen, and nitrogen. The amount of nitrogen does not decrease with argon sputtering, showing that it is incorporated into the titanium lattice. By integrating the area under the peaks we find that the N:Ti ratio is 0.34. The samples formed in only nitrogen have Ti $2p_{3/2}$ and $2p_{1/2}$ peaks at 454.1 and 460.0 eV, 0.2 eV higher than the untreated titanium control. The expected binding energy

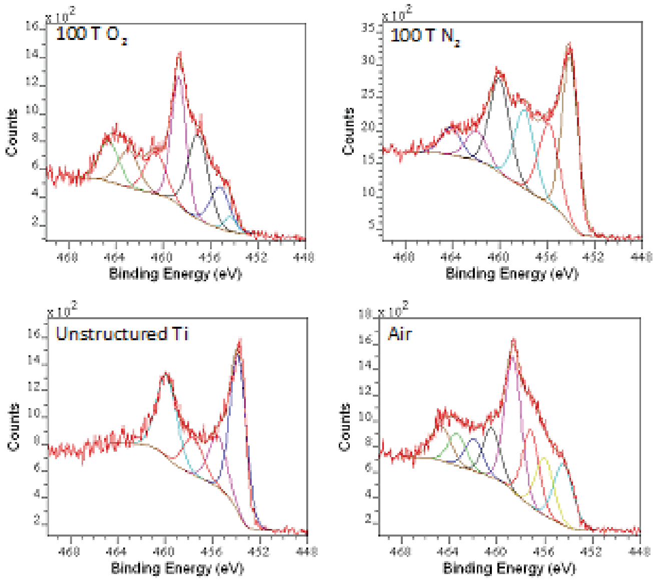

Figure 3.5: High resolution XPS of the Ti (2p) region of untreated and laser-structured titanium samples showing the separate peak fits. All samples were Ar+ sputtered for 20 minutes before measurements.

for Ti in TiN is 1.4 eV higher than the measured values. Previous studies of non-stoichiometric titanium nitride films with low nitrogen incorporation show Ti binding energies 0.3–0.4 eV above metallic Ti, similar to our samples. [110] Analysis of nitrogen incorporation as a function of nitrogen pressure incorporated during irradiation shows a slight decrease in nitrogen incorporation with decreasing nitrogen pressure. Nitrogen is only incorporated into the titanium lattice when surface structures are created, implying that the laser fluence necessary for nitrogen incorporation is above the melting threshold.

Titanium samples irradiated in 80 Torr N_2 and 20 Torr O_2, a composition approximating air, show incorporation of oxygen but not nitrogen. These samples also show the same Ti 2p peak placement as the sample irradiated in only oxygen, indicating the formation of TiO_2. We find that the presence of 0.1 Torr of oxygen in the chamber prevents the incorporation of nitrogen into the sample. The preferential formation of TiO_2 over TiN can be explained by considering the relative heats of formation (H_f) of the bulk materials. While the formation of both structures is exothermic, the heat of formation of TiO_2 is $H_f = -944.0$ kJ/mol, while the formation of TiN is less favorable at $H_f = -337.7$ kJ/mol. [111, 116]

We also used a variety of nitrogen- and oxygen-containing precursors, such as NO, NO_2, N_2O and NH_3, to address the chemical selectivity problem and see that no nitrogen incorporation occurs when oxygen is present.

We analyzed the crystal structure of the resulting films using both Raman spectroscopy and X-ray diffraction (XRD). XRD of the unstructured titanium film in Fig. 3.6 shows the characteristic peaks of α-Ti with a strong (002) peak at $2\theta = 38.3°$ and a smaller (103) reflection peak at 70.6°. This structure is expected for evaporated titanium films. [117] The laser structured samples do not show additional peaks that would indicate the presence of crystalline TiO_2 or TiN. We would expect peaks at $2\theta = 25.3°$ and 48.2° for anatase TiO_2 or at 27.5° and 54.3° for rutile TiO_2. [118] The structured films do have a small Ti (002) peak which can be attributed to the underlying unstructured titanium.

Raman spectroscopy confirms the amorphous nature of the structured films. As shown in Fig. 3.7, the samples structured in oxygen or air to form TiO_2 display a single broad peak at 240 cm^{-1} with a smaller broad hump around 450 cm^{-1}. The broad spectrum is consistent with an amorphous semiconductor. The peaks may be due to the presence of Ti_2O_3 because crystalline Ti_2O_3 has peaks at 269, 302, 347, and 452 cm^{-1}. [119] Spectra of a few nm-thick oxidized titanium films display similar

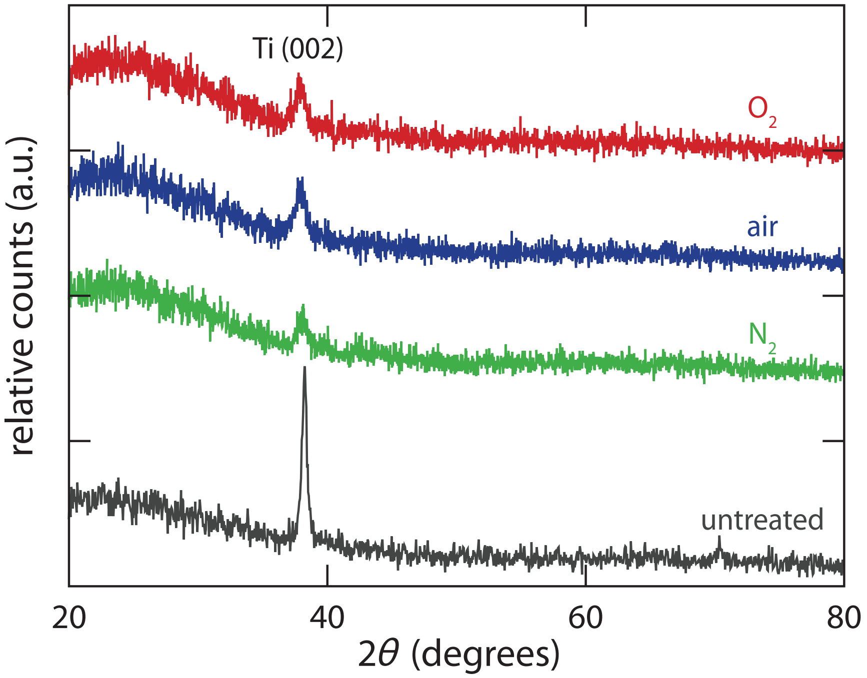

Figure 3.6: X-ray diffraction (XRD) of the untreated titanium and laser-structured samples. The films display only the (002) and (103) peaks expected for evaporated titanium.

broad peaks that have been attributed to a thin layer of Ti_2O_3. [120] These peaks indicate the presence of Ti_2O_3 species within the predominant TiO_2 shown in the XPS spectra. The presence of less oxidized species may be caused by preferential ablation of lighter oxygen atoms during laser irradiation. The absence of peaks at 447 and 612 cm^{-1} indicates that rutile TiO_2 is not present; similarly, anatase TiO_2 would lead to peaks at 144, 197, 399, 515, and 639 cm^{-1}, which are not observed. [118]

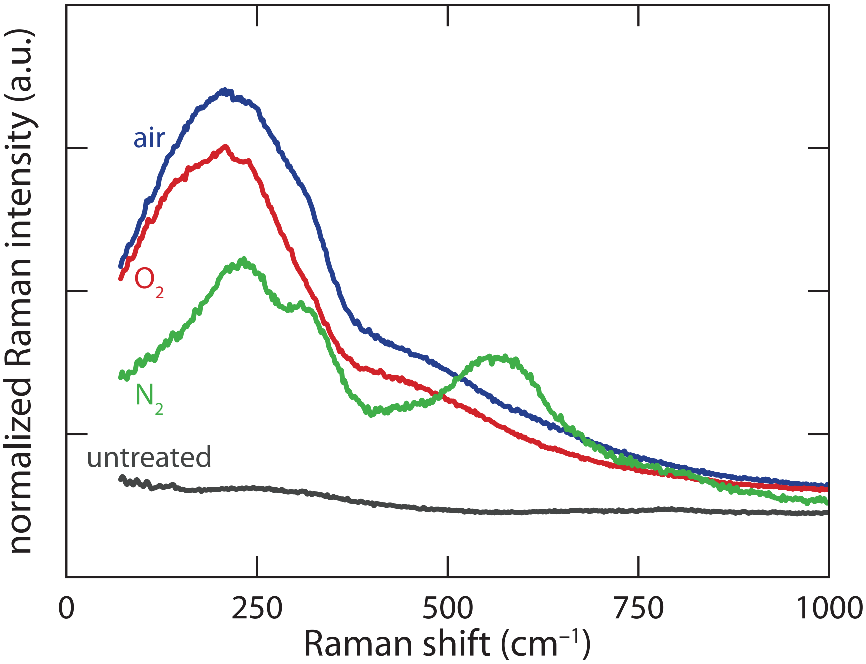

Figure 3.7: Raman spectra of the untreated titanium and laser-structured samples, collected from an excitation wavelength of 633 nm.

The sample structured in nitrogen resulting in non-stoichiometric TiN has broad Raman peaks at 240 cm^{-1}, 300 cm^{-1}, and 550 cm^{-1}. These are the expected peak positions for non-stoichiometric TiN; the lower-frequency peaks are attributed to acoustic phonons, and the high frequency peak at 550 cm^{-1} is attributed to optical phonons. [121] The peak positions are very similar to those observed for non-stoichiometric TiN formed by ns-laser irradiation of titanium in a nitrogen environment. [122] The Raman spectrum for the unstructured titanium film shows no significant peaks as expected.

Electrochemical stability tests performed in a solution used to simulate biocompatibility [115] demonstrate the stability of the TiO_2 films and their suitability for biological implants. For metal-based films, a high open circuit potential (OCP) indicates increased stability against oxidation. After two hours of stabilization, the samples irradiated in 100 Torr O_2 and 80 Torr N_2/20 Torr O_2 have open circuit potentials of 0.199 V and 0.092 V (vs. Normal Hydrogen Electrode, NHE) [123] respectively (Fig. 3.8a). Both oxidized samples have a higher OCP than the titanium plate, which has an OCP of –0.044 V, indicating their higher stability against oxidation. On the other hand, the sample structured in nitrogen shows lower stability against oxidation than the titanium plate with an OCP of –0.061 V.

We also measured the stability of the samples by applying a potential difference of 494 mV (vs. NHE), which is a standard benchmark for dental implant stability. Lower current densities are indicative of higher stability against chemical reactions such as ion release, and thus a higher stability of the oxidized films. As shown in Fig. 3.8b, we observe an immediate decrease in current when the potential is applied, indicating the formation of a passivation layer. The current of the laser-irradiated films stabilizes after about 10 minutes, and the oxidized films formed in both air and oxygen stabilize at current densities of 86 nA/cm^2. The titanium nitride films stabilize at a higher current density of 150 nA/cm^2. The unstructured titanium surface has the highest current density of 220 nA/cm^2 and takes longer than the irradiated films

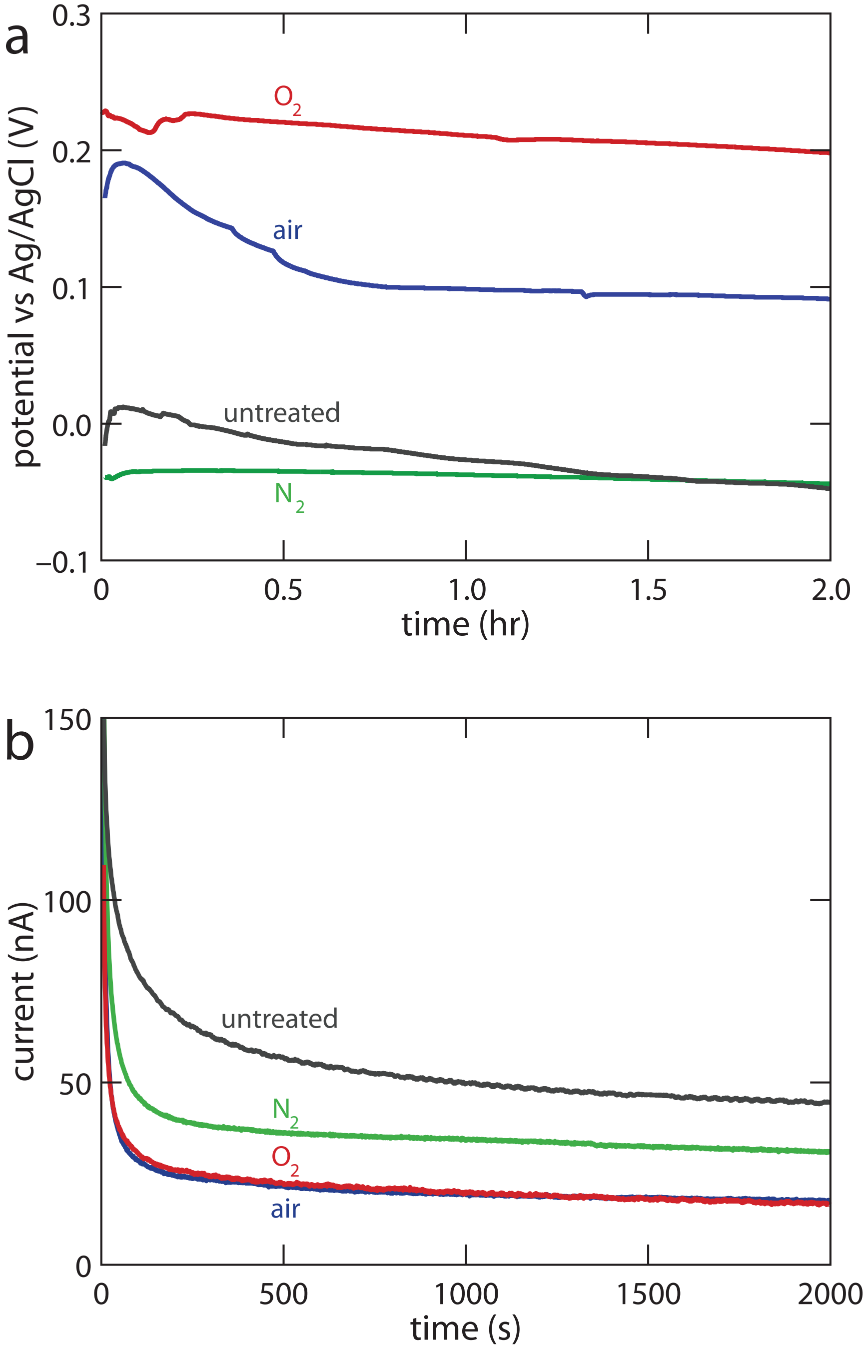

Figure 3.8: (a) Open circuit measurements before and after laser irradiation collected at room temperature in a solution to simulate biocompatibility (HBSS), measured vs. Normal Hydrogen Electrode (NHE). (b) Current density changes of untreated and laser-structured samples at 494 mV vs. NHE.

to stabilize, indicating that the passivation layer forms more slowly.

Because the surface morphology does not depend on gas composition and pressure, the chemical composition of the surface can be changed independently of the surface morphology. Our findings are in contrast to earlier published work showing a strong dependence of the surface morphology on gas composition and pressure when titanium is irradiated with nanosecond pulses below the ablation threshold. [110] As Fig. 3.9 shows, the reflectivity of the samples irradiated by femtosecond pulses does depend on gas composition—untreated titanium and surfaces irradiated in nitrogen and oxygen all have different reflectivities. Our work thus shows that femtosecond laser irradiation makes it possible to create films of varying chemical composition and optical properties while maintaining consistent surface structures.

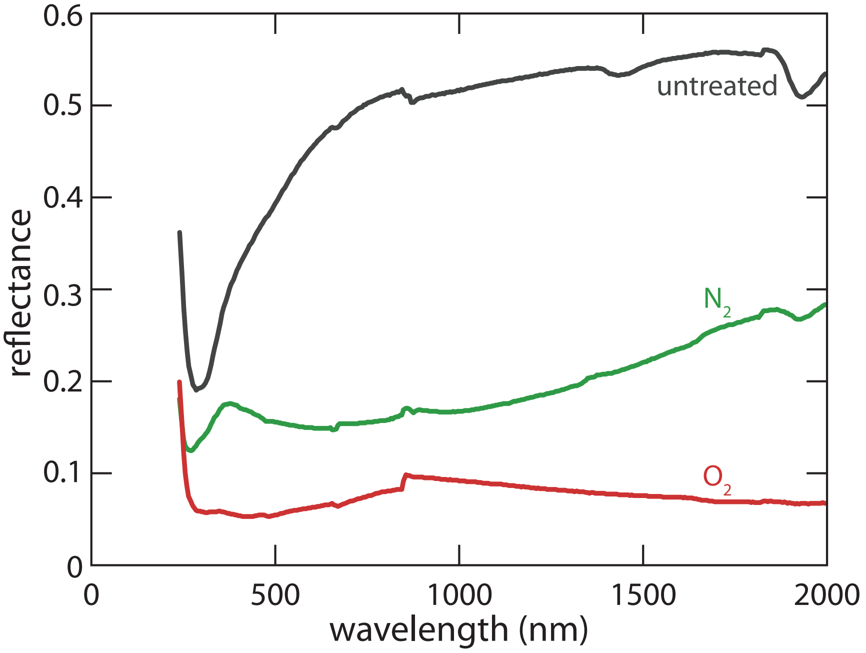

Figure 3.9: Reflectivity of samples measured with a spectrophotometer with an integrating sphere.

3.4 Conclusion

We form nanostructured TiO_2 and non-stoichiometric TiN films by femtosecond laser irradiation of titanium in oxygen and nitrogen, respectively. We demonstrate that oxygen and nitrogen are incorporated in these films when the laser fluence exceeds the ablation threshold. Furthermore, laser-formed TiO_2 is more stable than untreated titanium in biologically relevant solutions, making femtosecond laser-formed TiO_2 a good candidate for biomedical devices, which we explore further in Chapter 6.

CHAPTER 4

PHOTOELECTROCHEMICAL WATER OXIDATION OF LASER-PRODUCED RUTILE TIO_2

We demonstrate the use of femtosecond laser structuring of titanium metal in oxygen at room temperature, as a two-step method to produce a TiO_2 photoanode for photoelectrochemical water splitting. Annealing the laser-processed TiO_2 in an oxygen-containing atmosphere nearly triples the rate of photocatalytic oxygen evolution (external quantum efficiency = 12.0% at 354 nm) compared to thermally oxidized titanium or sputtered TiO_2. Sample characterization and temperature-programmed reaction spectroscopy experiments show that the photocatalytic enhancement of the oxygen-annealed, laser-processed TiO_2 is due to a complete oxidation of titanium, an absence of TiO_x phases, and a reduced number of surface or oxygen vacancy defects.

4.1 Introduction

Solar-driven water splitting uses photons to drive the energy-storing oxygen and hydrogen evolution reactions. A photoelectrochemical cell (Fig. 4.1) accomplishes this task by absorbing above-bandgap light and exciting an electron-hole pair. The hole is used for the oxygen evolution reaction and the electron is used for the hydrogen evolution reaction. [124] To allow the photo-excited electron-hole pair to drive the water splitting reaction, a photoelectrode material must have a bandgap that straddles the reaction potentials for the hydrogen evolution reaction (H_2/H^+) and the oxygen evolution reaction (H_2O/O_2). [125] In addition to this criterion, a good candidate material must also exhibit stability in a harsh and aqueous environment (usually at an extreme pH) over a long period of time and be cost-effective to produce in bulk.

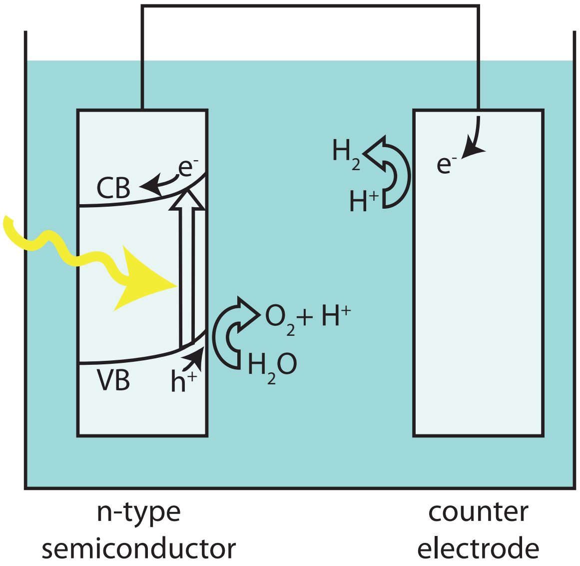

Figure 4.1: Photoelectrochemical cell with an n-doped semiconductor as the photoanode. Adapted from Ref. [124].

Titanium dioxide (TiO_2) is one of a few wide bandgap semiconductors (bandgap energy $E_g = 3$ eV) that fulfill many of these requirements. Due to its stability and bandgap placement, TiO_2 has been used for the past 20 years in water-splitting devices for hydrogen production. [124, 126] However, methods for producing TiO_2 for photocatalytic applications have many processing steps, such as with grown nanowires, or pose problems in controlling the crystal growth, such as with sol-gel or growing thin films.

Our objective is to manufacture a TiO_2 photoanode directly from titanium metal foil in a two-step process. We have previously demonstrated the use of femtosecond laser fabrication to incorporate dopants at concentrations over three orders of magnitude above the solid solubility limit in silicon [69] through a process called solute trapping. [16, 72] Laser pulses with energy greater than the melting threshold transform the surface into a molten layer, enabling dopant precursors in the vicinity to diffuse in. [71] Our motivation is to utilize the femtosecond-laser treatment method to oxidize the titanium metal and with annealing, produce a simple, cost-effective TiO_2 photoanode for efficient water oxidation that enables direct photoelectrolysis, as shown in Fig. 4.2.

In addition to doping, femtosecond-laser texturing can also originate from the formation of laser-induced periodic surface structures, which consist of semi-periodic nanometer- and micrometer-scale structures. [20–22] These laser-textured surfaces are independent of the crystal orientation and exhibit a wide range of feature sizes. We envision that femtosecond-laser texturing will increase water oxidation by providing greater surface area for light trapping and for surface reaction sites. With the stronger optical density afforded by the light trapping, we anticipate a reduction in the amount of the material required to absorb the solar spectrum, which will help reduce the dis-

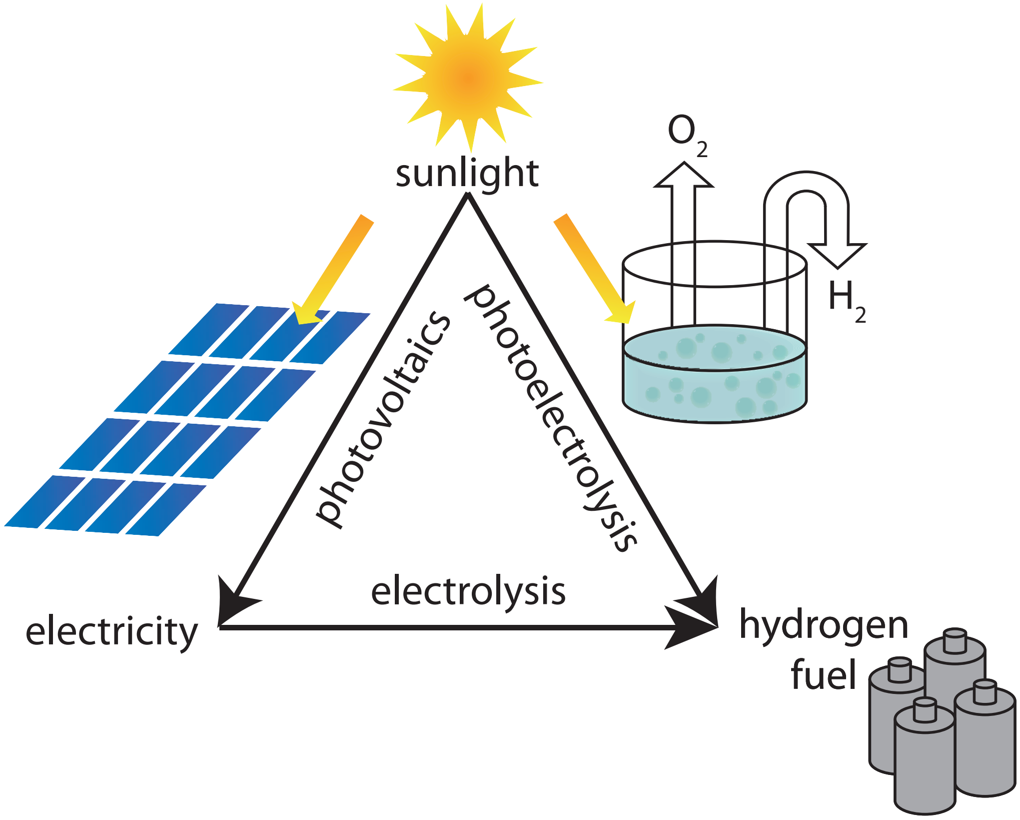

Figure 4.2: Energy diagram that shows the production of hydrogen from either photovoltaics with electrolysis or direct watersplitting through photoelectroysis.

tance that the minority carrier must diffuse in order to drive the photoelectrochemical water oxidation.

We have shown previously that it is possible to use a femtosecond laser to oxidize a surface while creating surface structures by laser treating titanium metal in oxygen. [35] The objective of this paper is to show that we can utilize ultrafast laser processing and annealing to produce a photoelectrochemically active surface of TiO_2 that has a higher conversion of water oxidation from incoming UV light. In this chapter, we first apply femtosecond laser processing to titanium. We then characterize the material, both before and after annealing, and compare the samples to two control samples in terms of their material properties and photoelectrochemical activity.

4.2 Experimental Procedure

We produce TiO_2 in square areas of 1 cm^2 by laser treating a 99.6% titanium foil with a 1-kHz train of 100-fs, 805-nm laser pulses from a Ti:sapphire laser with a fluence of 2.5 kJ/m^2 and a coverage of 50 shots per area using the setup shown in 4.3. [35] We mount the samples in a stainless steel chamber that is filled with oxygen at a pressure of 100 Torr and raster scan the laser over the sample using a scanning mirror setup that focuses a Gaussian-shaped pulse to a spot size of 800 μm on the surface. To anneal the sample after laser treatment, we place the laser-treated sample in a tube furnace heated to 1000 K for one hour with a flow rate of 300 sccm of high purity air.

To compare our laser-treated samples, we also produced two 1 cm^2 control samples. The first control is an annealed foil, produced by annealing an untreated

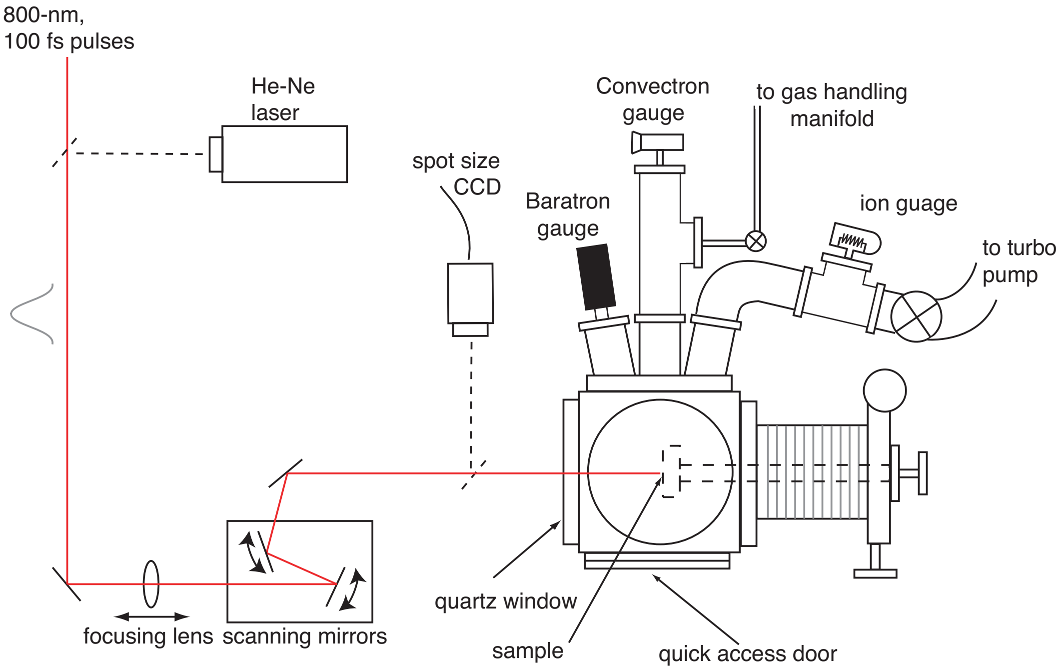

Figure 4.3: A schematic diagram of the fs-laser hyperdoping apparatus using a scanning mirror that translates the laser beam in relation to a stationary sample placed in the chamber on the right.

titanium foil under the same annealing conditions as the laser-treated sample. For the second control, we reactively sputtered 100-nm of amorphous TiO_2 onto titanium foil and annealed it in the same conditions as above. The process and subsequent material made from sputtering is discussed in Ref. [127].

We image the samples with an atomic force microscope in AC tapping mode and with a scanning electron microscope with a beam energy of 2 keV and a secondary electron detector.

We measure the emitted Raman spectra excited with 325 nm light, produced from a HeCd laser. We record the Raman spectra in a backscattering geometry through a 20X microscope objective, where the data is projected onto a charge-coupled device array using a 2400 grooves/mm. The spectra are reduced by the Bose distribution and fit using independent damped harmonic oscillator spectral profiles with a linear baseline and the Unifit procedure. [128, 129]

We collect and analyze the elemental content on a monochromatic aluminum-Kα (1486.6 eV) X-ray photoelectron spectrometer equipped with a 180° double focusing hemispherical analyzer. We perform high resolution scans with a 400-μm spot size, a bandpass energy of 50 eV, and a step size of 0.1 eV. We calibrate the samples with the adventitious carbon 1s peak (284.6 eV). [130]

We also perform X-ray diffraction measurements by scanning $\theta/2\theta$ in the 2θ range from 10 to 90 degrees to examine the crystallinity and phase composition of our samples. The $\theta/2\theta$ spectra are recorded using a four circle diffractometer with Cu-Kα radiation (1.5418 Å). After collecting our data on each sample, we compare the data to the database of the International Centre for Diffraction data in order to identify the observed diffraction peaks.

After laser treating and annealing the samples, we back-contact all of our samples individually. [131] We produce multiple sets of each sample in order to test for the surface reactivity and the photoelectrochemical efficiency in parallel and to ensure reproducibility of results.

The surface reactivity of the laser-treated samples is assessed by temperature-programmed reaction spectroscopy using formaldehyde as a probe molecule. The samples are mounted on a liquid-nitrogen cooled manipulator/sample holder by attaching a layer of ceramic glue to the backside of the sample. A tungsten filament and a K-type thermocouple embedded in the ceramic glue allow for resistive heating and accurate temperature control. Temperature-programmed reaction spectroscopy is performed in a stainless steel ultrahigh vacuum chamber with a base pressure of about 1×10^{-10} Torr. The sample is cleaned by multiple annealing cycles to 800 K and annealed at 700 K prior to each experiment. For the temperature-programmed reaction spectroscopy, we applied a linear heating rate of 2 K/s from 200 K to 700 K. We acquire mass-to-charge (m/z) traces of relevant masses with a pulse ion counting quadrupole mass spectrometer. Formaldehyde was dosed in excess at 250 K via a directed doser, which on TiO_2 (110) single crystal leads to a coverage of 0.4–0.5 monolayers. [132] No rise in chamber pressure was observed during the dosing of formaldehyde. Molecular oxygen was also dosed at 2×10^{-7} mbar for 10 min at 300 K via a directed doser.

For the photoelectrochemical measurements, we modify the 1 cm^2 samples by back-contacting and testing the samples individually. We must roughen the back of each sample with a diamond scribe to cut through the native oxide layer and provide better contact to the underlying metal. After scribing, we apply GaIn paint to the sample and place titanium wire on the paint. [131] We then apply high purity silver paint on the titanium wire to form a good contact. After the silver paint hardens, we apply an epoxy to the entire backside of the sample and on the titanium wire and allow the epoxy to cure for 24 h.

To test the water oxidation, we place each sample into a photoelectrochemical cell, which consists of 0.1 M KOH solution in a quartz cell in a three-electrode configuration. In our setup, the reference electrode is Ag/AgCl, which we calibrate against a hydrogen electrode using a platinum wire and find that the reference is 0.96 V versus the Reversible Hydrogen Electrode. We also use platinum as the counter electrode and take the measurements at room temperature. To operate the photoelectrochemical cell, we use a potentiostat to apply a bias while measuring the photocurrent created during the oxidation reaction. We compare the current-voltage data measured with and without illumination by a UV LED light centered at 354 nm. The difference in current with and without illumination gives the photocurrent as a function of voltage. The maximum power, as drawn from maximizing the product of the potential and the photocurrent, also gives a direct quantification of the external quantum efficiency.

4.3 Results

In this section, we present results on the four prepared samples we described above, which consist of two laser-treated samples and two control samples. We will refer to the laser-treated sample as "laser-treated unannealed" and after annealing the sample at 1000 K, we produce a sample that we will refer to as "laser-treated annealed." As for the control samples, we will refer to the annealed titanium foil without laser treatment as "foil annealed" and the annealed sputtered TiO_2 on titanium foil as "sputtered annealed."

Atomic force microscope and scanning electron microscope images of the four samples are shown in Fig. 4.4. The laser-treated, unannealed sample (Fig. 4.4, top) shows laser-induced periodic surface structures that are similar to those produced in Ref. [35]. After O_2-annealing, the laser-treated, annealed sample shows a change in morphology and surface structure. Notably, the roughness increases substantially after annealing. To compare to the two controls (Fig. 4.4, bottom), we see that the annealed samples show large surface roughness and a collection of aggregate particles. We find that the laser-treated, unannealed sample has the lowest root-mean-square roughness and that the three annealed samples show similar surface roughness.

The UV Raman spectra for the four samples are shown on the left in Fig. 4.5. Due to the high absorption of TiO_2 below the optical bandgap around 400 nm, we calculate a probe depth of 130 nm for an excitation source with a 325-nm center wavelength. The Raman spectra indicate that the three annealed films exhibit mainly Raman modes of rutile, while the laser-treated, unannealed sample is amorphous (Fig. 4.5, bottom left). For the laser-treated, unannealed sample, we observe a nonlinear background with a large, broad mode around 550 cm^{-1}, which is consistent with our previous results [35] and which shows that the laser-irradiated material is amorphous. For all three annealed samples, we observe E_g, A_{1g}, and B_{2g} modes at around 450, 614, and 825 cm^{-1} respectively, which are indicative of the rutile phase of

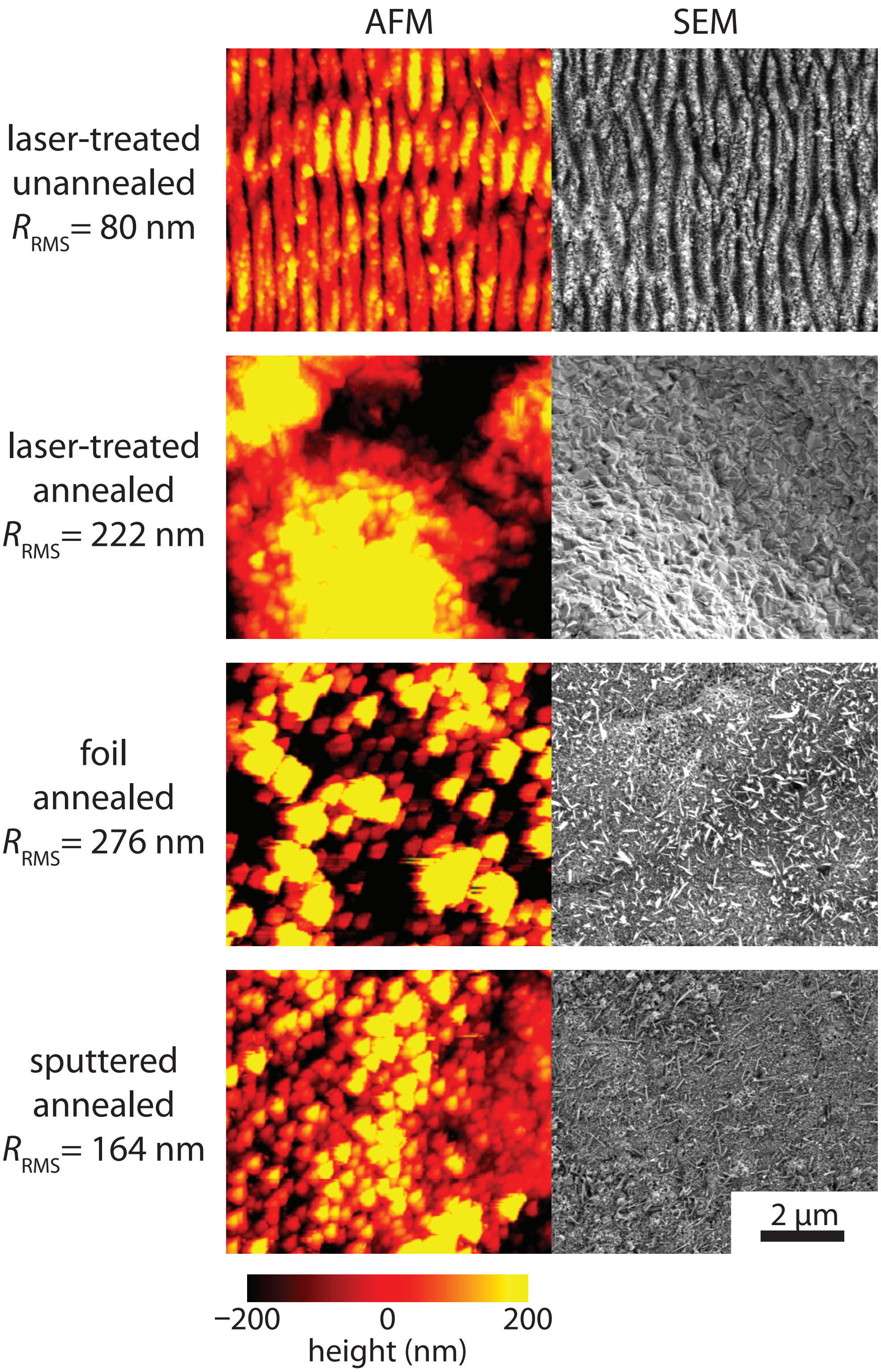

Figure 4.4: AFM and SEM of titanium metal surface after laser treatment before annealing (unannealed) and after (annealed) with RMS roughnesses. The two control samples are shown below.

TiO_2. [133] According to Raman polarization rules for the point group 4/mmm [134], the presence of E_g and B_{2g} modes (active in $Y(XZ)\overline{Y}$ (or $X(YZ)\overline{X}$) and $Z(XY)\overline{Z}$ polarization configurations, respectively) in the spectra of the annealed samples indicates that the rutile layers are polycrystalline. The Raman modes at around 320–365 cm^{-1} and 700 cm^{-1} also originate from the rutile phase. [133] Because the Raman intensity is reduced at around 230 cm^{-1} by an edge filter, we do not study the rutile mode at 235 cm^{-1} in this work. B_{1g} and A_{1g}/B_{1g} modes with low Raman efficiency of the anatase phase are observed at around 415–425 cm^{-1} and 513–523 cm^{-1} in the spectra of the three annealed samples, respectively. [133] Because of their low intensity and the overlap with the intense modes of the rutile phase, the positions of these modes are approximate.

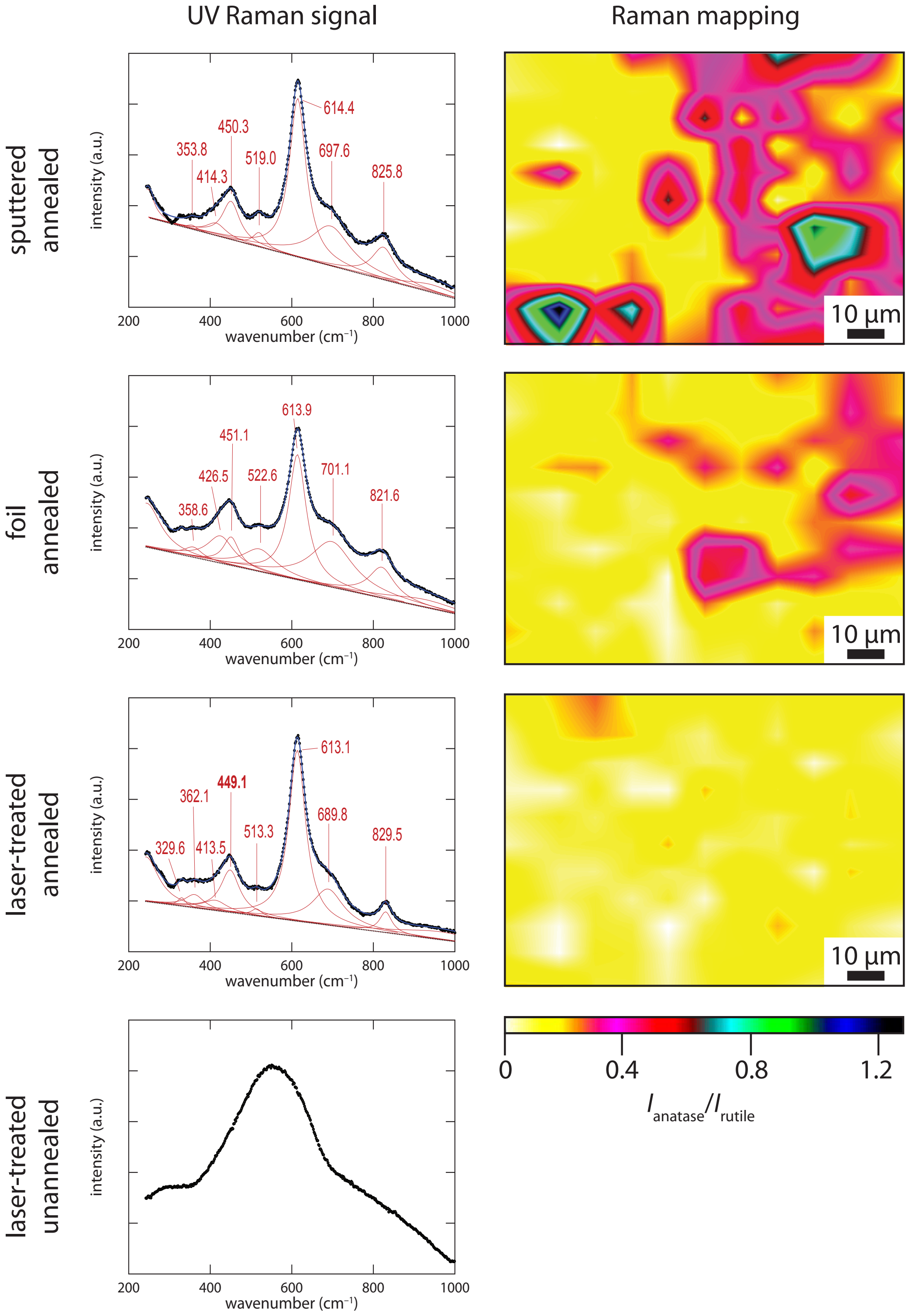
UV Raman signal
Raman mapping
sputtered annealed
foil annealed
laser-treated annealed
laser-treated unannealed
intensity (a.u.)
wavenumber (cm⁻¹)
200
400
600
800
1000
614.4
450.3
353.8
519.0
697.6
414.3
825.8
613.9
451.1
426.5
522.6
701.1
358.6
821.6
613.1
449.1
362.1
689.8
513.3
329.6
413.5
829.5
10 µm
0
0.4
0.8
1.2
I_anatase/I_rutile

Figure 4.5

Figure 4.5 *(previous page)*: (left) Unpolarized Raman spectra of laser-formed TiO_2, before and after annealing, compared to control samples (black dots). The linear baseline, damped oscillator profiles, and their wavenumbers, used for fitting the spectra, are presented in brown. The spectra generated by the fitting procedure is presented by blue line. (right) Mapping of the ratio of integrated intensities in the spectral ranges 500–550 cm^{-1} and 425–475 cm^{-1}, which corresponds approximately to the areas of anatase A_{1g}/B_{1g} mode and rutile E_g mode, respectively. The mappings are 100 μm × 100 μm^2 with steps of 10 μm in the x and y directions on the laser-treated, annealed, sputtered annealed and foil annealed samples. There is no area mapping for the laser-treated, unannealed sample due to the sample being amorphous so there are no peaks to fit.

Raman spectroscopy is a local analysis: the diameter of the probed area is around 2 μm. In order to obtain more information on the anatase to rutile volume fractions in the annealed samples, we performed two-dimensional Raman mapping. For this purpose the UV Raman spectra are mapped over an area of 100×100 μm^2 and with steps of 10 μm in the x and y directions. To illustrate the distribution of anatase and rutile phases, we plot the ratio of integrated intensities of the A_{1g}/B_{1g} mode of anatase around 523 cm^{-1} and the E_g mode of rutile around 446 cm^{-1} as a function of the location on the sample surface (Fig. 4.5, right). The anatase phase is distributed inhomogeneously on the surface of the three annealed samples. This inhomogenous distribution shows that anatase precipitates as the inclusions in the rutile phase matrix. The rutile phase is dominant over the anatase phase in all the samples annealed at 1000 K. The quantitative estimation of the volume fraction of the two phases is possible only if the absolute intensities, measured at identical experimental conditions, of Raman modes of pure anatase and rutile phases are known. Thus, in this work we limit our interpretation to the relative comparison of the phase composition in the annealed samples. As can be seen in Fig. 4.5, the sputtered annealed TiO_2 contains an important fraction of the anatase phase. It is much less apparent in the TiO_2 layer formed by annealing titanium foil, and the fraction is even smaller in the laser-treated, annealed sample.

Damping of phonons indicates the imperfections in the sample's long-range order. The Raman modes of rutile, synthesized by annealing foil or by annealing sputtered TiO_2, show similar damping. For example, the damping of A_{1g} mode (at 614 cm^{-1}) is around 50 cm^{-1} and does not vary much across the surface of these two samples. The Raman modes in the laser-treated, annealed sample show an increase in the damping by 2–3 times in some locations on the surface. The Raman modes with the lowest and highest damping observed in the spectra of this sample are illustrated in Fig. 4.6. The damping of A_{1g} mode varies in the range of 48 cm^{-1} to 109 cm^{-1}. The variation in damping of the E_g mode of TiO_2 in the foil annealed and laser-treated, annealed samples is also mapped and presented in Fig. 4.6. The considerable variation of Raman mode damping in the laser-treated, annealed sample can be attributed to the presence of zones composed of well crystallized/ordered and nanocrystalline/more disordered rutile. About 50% of the laser-treated, annealed sample consists of disordered rutile. These disordered zones are not present in the sputtered annealed sample, which is also initially amorphous. The lack of disordered zones in the sputtered annealed sample shows that annealing for 1 h at 1000 K is sufficient for the crystallization of amorphous TiO_2 and that the formation of these zones is directly related to the laser treatment.

To further examine the surface of our materials, we present the X-ray photo-

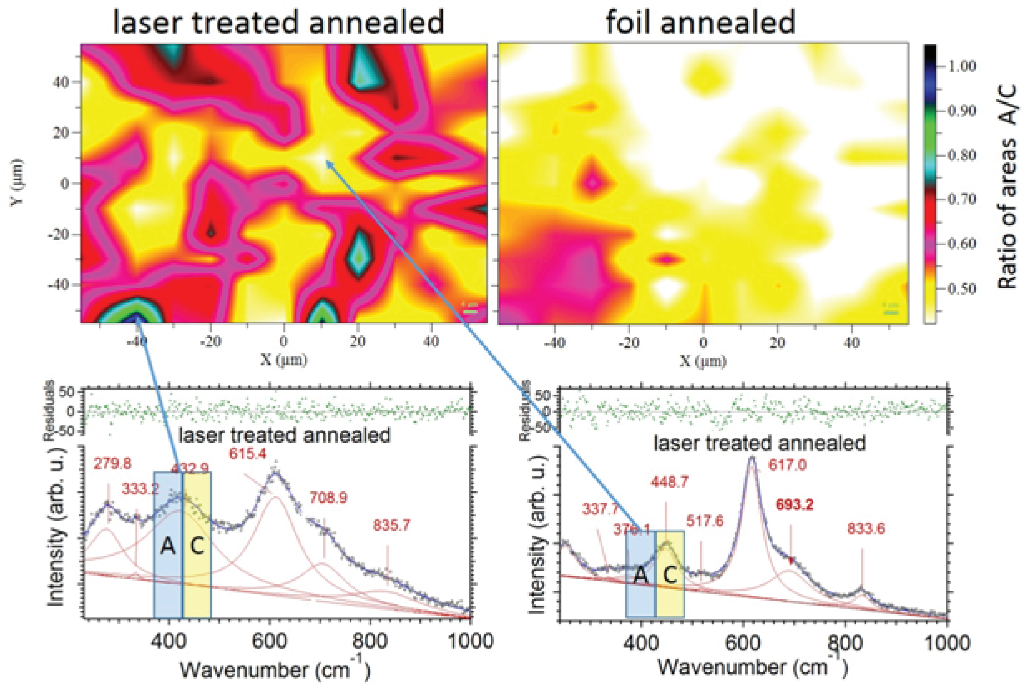

Figure 4.6: Mapping of ratio of integrated intensities in the spectral ranges 375–425 cm^{-1} (A) and 425–475 cm^{-1} (C), which represents the broadening of rutile E_g mode (top). The mappings are 100 μm × 100 μm^2 with steps of 10 μm in the x and y directions on the laser-treated annealed and foil annealed samples. The Raman spectra representing the surface zones of high crystalline quality and of highly disordered ones in laser-treated sample are given for illustration (bottom).

electron spectra for the Ti 2p peak for the four samples in Fig. 4.7. As in the Raman data, the three annealed samples show similar curves while the laser-treated, unannealed shows a significant low binding energy shoulder in the Ti $2p_{3/2}$ feature and a slight broadening of the $2p_{1/2}$ peak. By examining the binding energy values, we identify the oxidation state of the surface titanium ions to determine the chemical composition of our samples. For all three annealed samples, we see Ti $2p_{3/2}$ and Ti $2p_{1/2}$ peaks at 458.7 and 464.3 eV respectively, which correspond to Ti^{4+}, the oxidation state found in TiO_2. [135] For the laser-treated, unannealed sample, the shoulder observed at a lower binding energy in the Ti $2p_{3/2}$ peak is assigned to Ti^{3+}, which is commonly observed at 457.2 eV. [136] With the mix of oxidation states, we believe that the three annealed samples are similar in chemical composition within the probe depth of 5–10 nm. [137]

We perform X-ray diffraction to verify the composition of crystalline phases of our samples and compare the results to the background substrate, an unannealed titanium foil. The $\theta/2\theta$ patterns are shown in Fig. 4.8 for the four samples shown previously and the titanium substrate. Two ranges of 2θ angles are presented which are representative of the greater trends that we see in the entire X-ray diffraction data set. The $\theta/2\theta$ pattern of titanium foil consists of (002), (101), and (102) reflections of titanium (Ti) metal ($2\theta = 38.4°$, $40.2°$, and $53.0°$, respectively). [138] The reflections of titanium present highly asymmetric profiles towards small 2θ angles. These asymmetric profiles can be deconvoluted to the reflections of titanium metal and those of native oxides consisting of Ti-rich TiO_x phases with an oxidation state close to those of $TiO_{0.325}$ and Ti_6O phases. [139, 140] After laser treatment, the X-ray diffraction

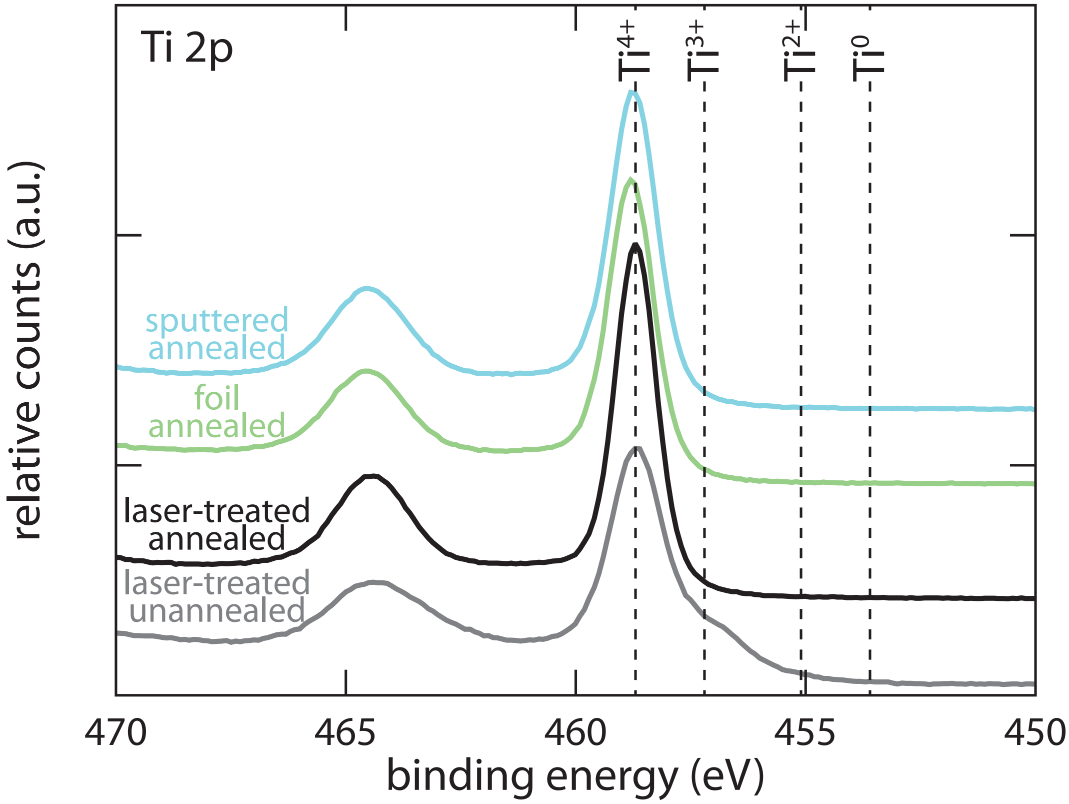

Figure 4.7: High resolution XPS of the Ti (2p) region of all four samples, showing a similar amount of Ti^{4+} signal with the unannealed sample showing the most Ti^{3+} signal.

reflections have more symmetric profiles than those of titanium foil observed before the treatment and are centered at the 2θ angles corresponding to the reflections of hexagonal structure of titanium. We explain thisy symmetry by the disappearance of crystalline TiO_x phases due to the incorporation of higher oxygen content in the surface layer and/or amorphization induced by laser treatment. After annealing, the $\theta/2\theta$ pattern of the laser-treated sample consists of (101), (111), and (211) reflections of rutile, indicating the polycrystalline nature of this phase and reflections of titanium metal. The X-ray diffraction signatures of the sputtered annealed and foil annealed samples are similar:

1. The diffracted intensity due to titanium metal decreases significantly compared to the pattern of the laser-treated, unannealed sample, showing oxidation of titanium during the annealing process. The titanium reflections are still present after laser irradiation and annealing, which reflect that the laser and thermal treatment modifies only the surface of the titanium foil.

2. The reflections with the highest intensity in the pattern are those of Ti-rich oxides TiO_x with $x < 0.5$, which show broad profiles related to having a gradient of titanium oxidation in the samples. [139, 140]

3. The reflections of the rutile phase have a low intensity and a broad profile compared to those of rutile in the laser-treated, annealed sample.

Therefore, we believe that the foil annealed and sputtered annealed samples contain a combination of many different species of partially oxidized titanium and that the rutile phase in these specimens has variations in oxidation state. The measured

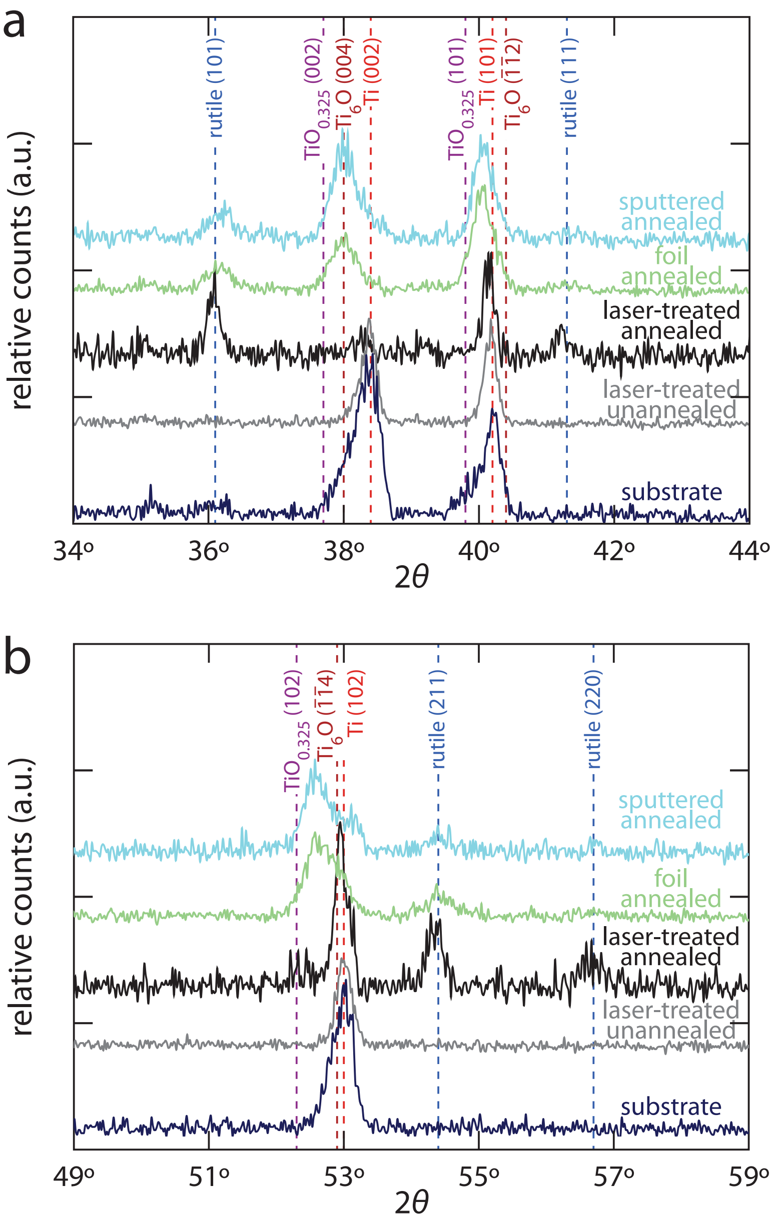

Figure 4.8: $\theta/2\theta$ XRD patterns of four samples with the titanium substrate over two ranges of 2θ angles. The indexation and 2θ angles of reflections of rutile, $TiO_{0.35}$, Ti_6O, and titanium phases indicated in the ICDD database are presented by dashed lines. (a) 2θ=(34–44) shows a higher rutile signal for the laser-treated annealed and (b) 2θ=(49–59) shows more rutile reflections and that the control annealed samples have a mixture of oxide states, while the laser-treated unannealed only shows the reflections of titanium and TiO_x $(x < 0.5)$.

diffracted intensity in our X-ray diffraction setup is very low, which explains why the reflections of the anatase phase, which has a small signal compared to the rutile phase in the Raman data, are not observed in the $\theta/2\theta$ patterns. To summarize, according to the X-ray diffraction data, the laser treatment and annealing afterward of titanium foil results in a homogenous TiO_2 layer on titanium foil, while the samples formed by simple annealing of titanium foil or by depositing amorphous TiO_2 on foil and then annealing, result in a mixture of different titanium oxides.

Because we fabricated the samples for water oxidation, it is important to understand the surface and its defects, which play a role in the photoelectrochemical reaction. In order to study the surface defects, we use temperature-programmed reaction spectroscopy to characterize the surface thermochemical behavior of the two laser-treated samples. We use formaldehyde as a probe molecule to assess the surface reactivity of the two laser-treated samples, shown in Fig. 4.9. Previous work has shown that a reductive coupling of two formaldehyde molecules to form ethylene is the dominant reaction pathway for formaldehyde adsorbed on highly defective TiO_2 (110). [141] The temperature-programmed reaction spectra of formaldehyde on TiO_2 is therefore a strong indicator for evaluating the defect concentration of a sample. Mechanistically, the reductive coupling of two adsorbed formaldehyde molecules via a C-C bond formation is governed by the availability of surface oxygen defects and oxophilic Ti^{3+} subsurface interstitials, which can form a surface complex with adsorbate molecules and successively react through removal of oxygen:

$$2H_2CO_{ad} + 4Ti^{3+} \rightarrow C_2H_4 + 4Ti^{4+} + 2O_{latt}. \tag{4.1}$$

The thermal (defect-driven) surface chemistry of the two laser-treated samples is compared by following mass-to-charge (m/z) traces 29 (H_2CO) and 27 (C_2H_4), as depicted in Fig. 4.9. Desorption of unreacted molecular formaldehyde ($m/z =$ 29, black and grey lines) is observed on both samples at approximately 300 K with slightly broader features for the laser-treated, unannealed sample. Notably, the overall amount of formaldehyde (and also other adsorbates such as water and methanol, data not shown) desorbing from the laser-treated, unannealed surface is 4–5 times that observed on the laser-treated, annealed sample, indicating that more adsorption sites are available on the unannealed sample. As evident from the $m/z = 27$ (ethylene) trace in Fig. 4.9, significant amounts of ethylene are formed on the laser-treated, unannealed sample (grey line, bottom), with a desorption peak maximum at 520 K, whereas the laser-treated, annealed sample shows little ethylene formation at 600 K. The small ethylene feature on the laser-treated, annealed sample is due to the presence of small amounts of defects (oxygen vacancies), similar to that observed on mildly reduced TiO_2 (110). With respect to the formaldehyde saturation dose at 250 K, the amount of ethylene formed on the unannealed sample is six times higher than on the laser-treated, annealed surface.

Compelling evidence for the role of oxygen vacancy defects in the ethylene formation comes from pre-dosing molecular oxygen prior to formaldehyde adsorption, which efficiently reduces the number of the oxygen vacancy defects present in reduced TiO_2. [142, 143] It is known from single crystal studies that oxygen can react with oxygen vacancies by filling the vacancy with one oxygen atom and leaving behind an adventitious oxygen adatom (O_{ad}) on the surface:

$$V_O + O_2(g) \rightarrow O_{latt} + O_{ad}. \tag{4.2}$$

The newly formed O_{ad} are notable for their interaction with Ti^{3+} subsurface interstitials, forming TiO_2 islands upon heating. [144] Therefore, the effect of the pre-dosing oxygen is to heal oxygen vacancies and to screen the excess charge of Ti^{3+} subsurface interstitials. The effect of oxygen pre-dosing is shown for both samples in Fig. 4.9 (black and grey dashed lines). On the laser-treated, annealed sample ethylene formation is completely quenched whereas for the laser-treated, unannealed sample, we observe a 95% reduction in overall ethylene formation and a temperature shift of 20 K towards higher T, which is commonly observed when defect chemistry is quenched by pre-exposure to oxygen. [145]

To explore the efficacy of the laser-treated, unannealed and laser-treated, annealed samples for photoelectrochemical water oxidation, we irradiate the samples with 354-nm LED light in a photoelectrochemical cell. We sweep the applied potential difference from –0.7 V to +0.7 V vs. Ag/AgCl and measure the current produced. The photocurrent, which is the difference between the data measured under dark (no illumination) and light (illumination) conditions, is calculated and shown as a function of applied potential difference in Fig. 4.10. We observe that the photocurrent is highest in the laser-treated, annealed sample and that there is hardly any photocurrent in the laser-treated, unannealed sample, showing that the annealing step is necessary for photocurrent generation. The two control samples, the foil annealed and the sputtered annealed, show very similar photocurrent outputs that are about around a third of the photocurrent of the laser-treated, annealed sample.

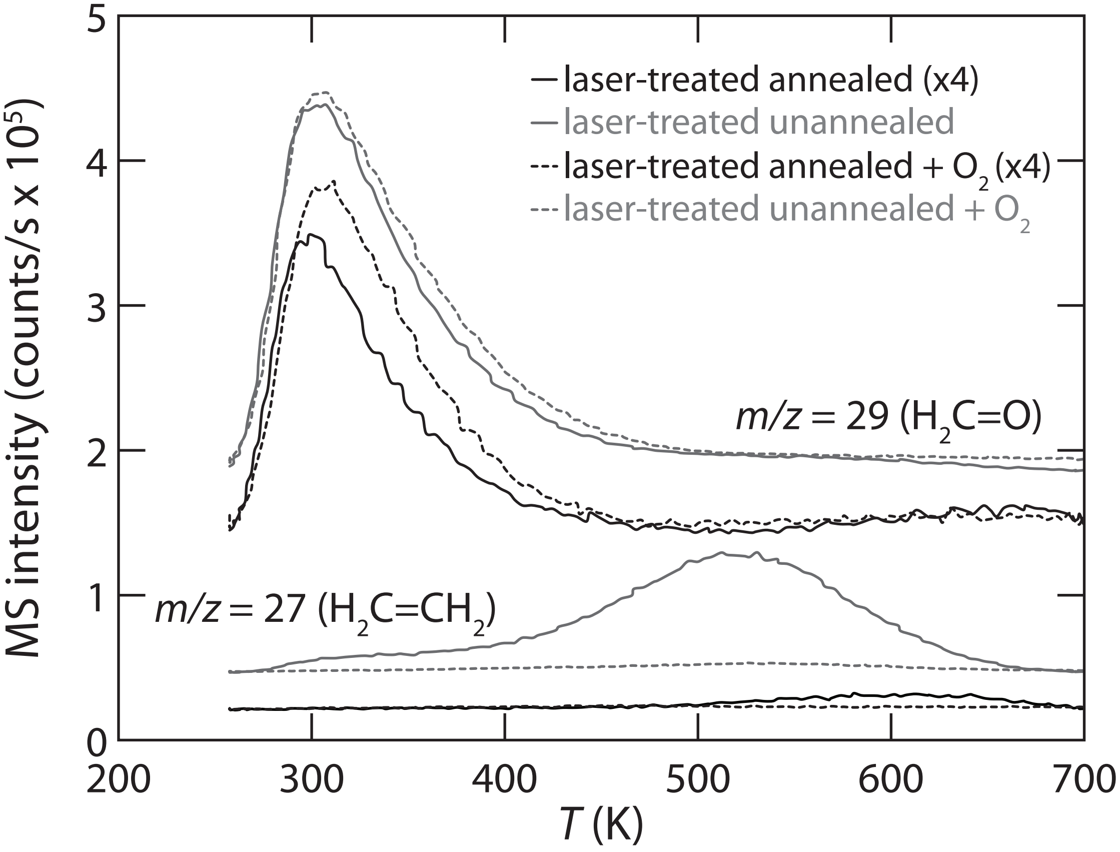

Figure 4.9: Thermal reaction spectra of formaldehyde adsorbed on the laser-treated, unannealed (grey), laser-treated, unannealed with O_2 pre-dosed (grey dashed), laser-treated, annealed (black), and laser-treated, annealed with O_2 pre-dosed (black dashed) samples. $m/z = 29$ is assigned to molecular formaldehyde (HCO^+), and $m/z = 27$ is representative of ethylene ($H_2C{=}CH^+$) formation. Molecular desorption of formaldehyde occurs on both samples at 300 K, whereas on the unannealed sample defect-driven formation of ethylene is observed at 520 K. Ethylene formation is due to reductive coupling of two formaldehyde molecules. Subsurface Ti interstitials migrate to the surface and strip the oxygen from formaldehyde, forming TiO_x on the surface and ethylene(g). Only very minor defect-induced coupling is observed on the annealed sample at 600 K, similar to the observations made on mildly reduced $TiO_2(110)$. O_2 adsorption heals surface defects and efficiently screens subsurface Ti-interstitials and therefore quenches ethylene formation in both cases.

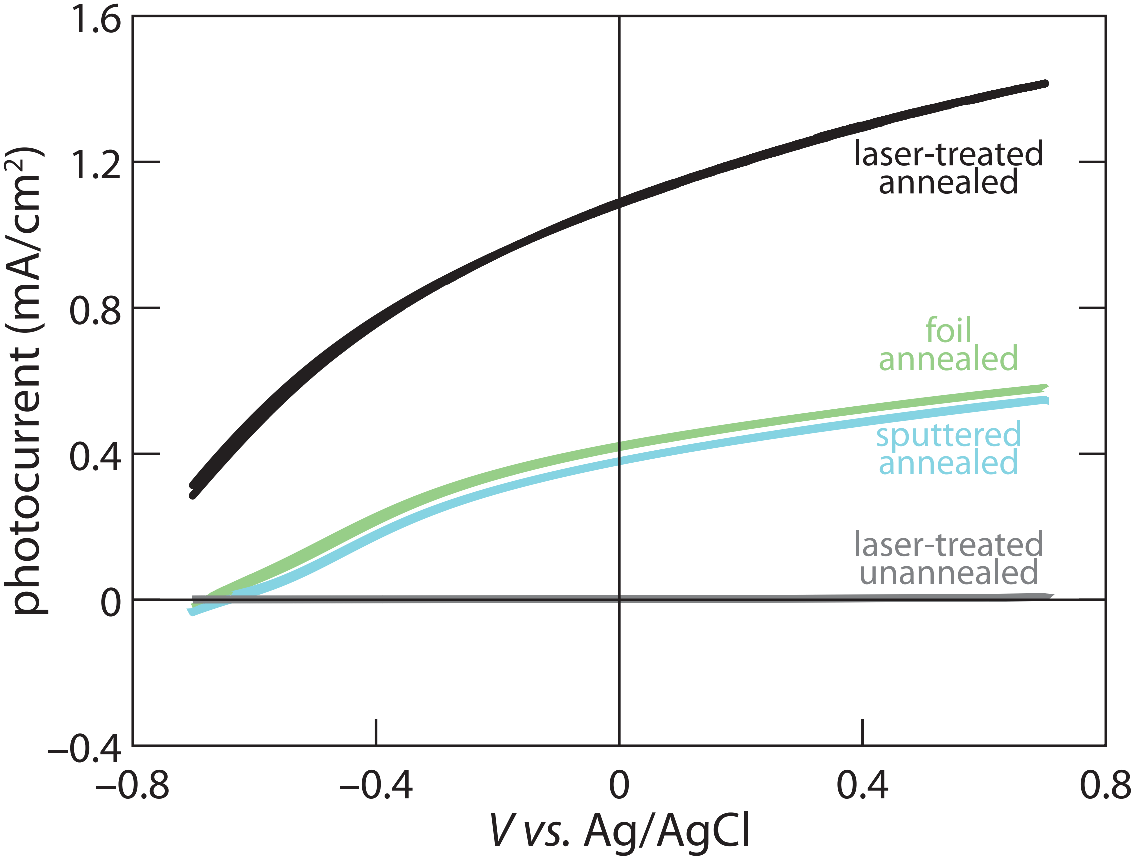

Figure 4.10: Three-electrode photoelectrochemical measurement with excited light from 354 nm LED in 0.1 M KOH solution.

Table 4.1: Photocurrent of four samples, including the laser-treated, annealed and the laser-treated, unannealed with the two control samples. We see the highest photocurrent and efficiency with the laser-treated, annealed sample.

Sample	Photocurrent (at 0.2 V vs. Ag/AgCl)	EQE
laser-treated unannealed	$< 0.01\ mA/cm^2$	$< 0.1\%$
laser-treated annealed	$1.2\ mA/cm^2$	12.0%
foil annealed	$0.48\ mA/cm^2$	4.8%
sputtered annealed	$0.44\ mA/cm^2$	4.4%

To calculate the external quantum efficiency (EQE), we take the maximum power from the product of the potential (versus the Normal Hydrogen Electrode) and the photocurrent for each sample and divide the product by the measured output power of the LED UV light that impinges on the sample's surface. We list the EQE in Table 1. The laser-treated, annealed sample has the highest EQE at 12.0% under 354-nm illumination.

4.4 Discussion

By laser-treating titanium foil and then annealing the laser-treated sample, we see that the photocurrent increases substantially compared to all of the other samples. The laser-treated, annealed sample is nearly three times more efficient at water oxidation when compared to the control samples due to its almost pure rutile form and homogeneous oxidation state. We show that the annealing step is also important in the process because the laser-treated, unannealed sample has such low photocurrent and has so many defects. Through laser-treating and annealing, we see the greatest increase in photocurrent due to producing a high quality TiO_2 layer with less oxygen defects.

From the perspective of fabricating a TiO_2 photoanode directly from titanium metal, our method is comparatively superior to both simple thermal oxidation of titanium foil and sputtering due to the enhanced photocurrent. The laser-treated, annealed sample is significantly more efficient due to the well-formed rutile TiO_2, the absence of TiO_x oxides where $x < 2$, and the disappearance of graduated oxidation states following the annealing step. The enhancement in the photocurrent should not stem from a light-trapping mechanism as all annealed samples display similar roughness, although electromagnetic field modeling would be essential to prove this hypothesis.

To understand the enhancement that we see from laser treatment and annealing, we begin our discussion with the issues that we see with the laser-treated, unannealed sample. The X-ray diffraction result shows no long-range order for the laser-treated, unannealed sample, suggesting the lack of any crystalline structure. This leaves two possibilities: a formation of amorphous titanium oxides or a mixture of amorphous titanium metal and amorphous oxide. The X-ray photoelectron spectrum reveals the formation of $Ti^{3+/4+}$, which supports the former possibility. Moreover, the laser treatment eliminated the possibility of crystalline native TiO_x ($x < 0.5$) phases. We therefore conclude that the majority of the surface of the laser-treated, unannealed sample is a film of an amorphous titanium oxide, with a mixture of $Ti^{3+/4+}$. In addition, the surface of the laser-treated, unannealed sample is filled with oxygen vacancies as suggested by the formaldehyde temperature-programmed reaction spectra, where significant formation of ethylene (suggestive of oxygen-vacancy-driven reductive coupling) is observed.

During the annealing process, the oxygen and titanium in the amorphous surface layer crystallize to produce a crystalline rutile structure. The formaldehyde temperature-programmed reaction spectra shows that the laser-treated, annealed sample resembles that of mildly reduced $\mathrm{TiO_2}$, with limited ethylene formation unlike the laser-treated, unannealed sample that is filled with defects. We therefore hypothesize that the laser-treated, annealed sample is essentially a low oxygen-defect rutile $\mathrm{TiO_2}$ material composed of highly crystalline zones and disordered zones resting on top of the original titanium foil. In fact, previous research has shown the disordered surface structure may increase the water splitting efficiency significantly. [146] When compared to the other annealed samples, we see that the laser-treated sample has more rutile phase while the foil annealed and sputtered annealed samples contain a variety of under-oxidized titania species. It is interesting to note that our result does not agree with previous work showing the formation of a single-phase, rutile $\mathrm{TiO_2}$ film with a heat treatment at a temperature above 850 K. [147]

We observe that the laser-treated, unannealed sample has almost no photocurrent. We explain the origin of the lack of photocurrent with the high surface defect concentration as observed in the formaldehyde temperature-programmed reaction spectra and the amorphous structure as indicated with Raman and X-ray diffraction data. Oxygen vacancy defects produce well-known mid-gap states [148, 149], which can facilitate the electron-hole recombination via the Shockley-Read-Hall mechanism. [150, 151] With all of these defects, it is not a surprise that the sample does not produce any photooxidation.

In contrast to the lack of the photoelectrochemical activity in the laser-treated, uannealed sample, the laser-treated, annealed sample shows a relatively high EQE for photoelectrochemical water splitting. In comparison to literature data for single crystal, rutile TiO_2, our EQE result at 354 nm is greater than for a mechanically polished TiO_2 sample (less than 5%) [152] when compared at an equivalent potential near the OER equilibrium but lower than the research that reported 80% EQE at a similar overpotential (η = 0.4 V). [153] Balancing the absorptive path and the minority carrier diffusion length will be essential to further engineer TiO_2 for better photoelectrochemical water splitting.

4.5 Conclusion

We produce photoelectrochemically-active TiO_2 directly from titanium metal by laser structuring titanium in oxygen and annealing in air. By laser-treating the sample, we incorporate oxygen deep into the material, which produces a rutile structure after annealing. Simple thermal oxidation and sputtering do not produce a pure rutile phase, effectively degrading their photoelectrochemical oxygen evolution activity. By laser-treating titanium metal and annealing, we have made a photocatalytically-active TiO_2 in two steps. Exploring this material platform further will be essential to understand the efficiency limit and how to design a photoelectrochemical electrode to push production of solar hydrogen with simple, low-cost manufacturing techniques.

CHAPTER 5

LASER DOPING OF WIDE BANDGAP SEMICONDUCTORS

Highly efficient photoelectrochemical water-splitting technology requires new semiconducting materials with three important photo-electrode properties: 1) high solar-to-fuel conversion efficiency; 2) efficient material utilization through light-trapping and high surface area surface structures; and 3) use of non-toxic and Earth-abundant materials to ensure sustainability. Femtosecond laser fabrication offers a promising route to address these challenges simultaneously by modifying the valence band of metal oxides via hyperdoping and structuring the surface of these materials. The surface texturing, which occurs simultaneously during laser treatment, increases the light trapping ability of the device and its reaction area. With more surface area and optical density, we can reduce the amount of the material required to absorb the solar spectrum while gaining a high catalytic area advantage. Finally, the femtosecond-laser processing technique is versatile and scalable; it can be applied to a wide range of Earth-abundant host materials and dopants, ensuring its long-term utility.

In this chapter, we describe a series of experiments using femtosecond laser processing techniques on a variety of wide bandgap semiconductors to produce photoanodes for light-induced water oxidation for solar energy storage. We discuss the incorporation of transition metals, specifically Mn, Cr, and Ni, into TiO_2 at high concentrations through femtosecond laser irradiation. After annealing, the resulting photocatalysis is lower for Cr and Mn doped materials and similar for the Ni dopant. We show through Raman and X-ray photoelectron spectroscopy that it is the oxidation state of the dopant that dictates the resulting water oxidation efficiency. We then translate this to other oxides and summarize the characterization of our materials through chemical and electronic techniques. Then we produce semiconductor photoanodes and test their viability in a photoelectrochemical cell.

5.1 Introduction

The fundamental scientific principles of our proposed work are based on improving two important aspects of the photoanode: 1) inclusion of dopants for more efficient visible-light utilization and 2) increased surface area for enhanced chemical reactivity and light trapping. Our group has extensive experience in femtosecond laser processing techniques, and here we specifically focus on the semiconducting oxide class of materials as they can withstand the strong oxidizing potential that is required to split water.

A photoelectrochemical cell (see Fig. 4.1) uses incoming light to perform water splitting. There are a variety of materials that are capable of performing the water splitting reaction. The main criteria for a good candidate material are:

1. correct placement of band positions to facilitate electron and hole injections in relation to the half-reaction potentials, as shown in Fig. 5.1.
2. a 1.5–2.0 eV bandgap to maximize the number of visible light photons that can be used from the solar spectrum.
3. stability in a harsh and aqueous environment over a long period of time.

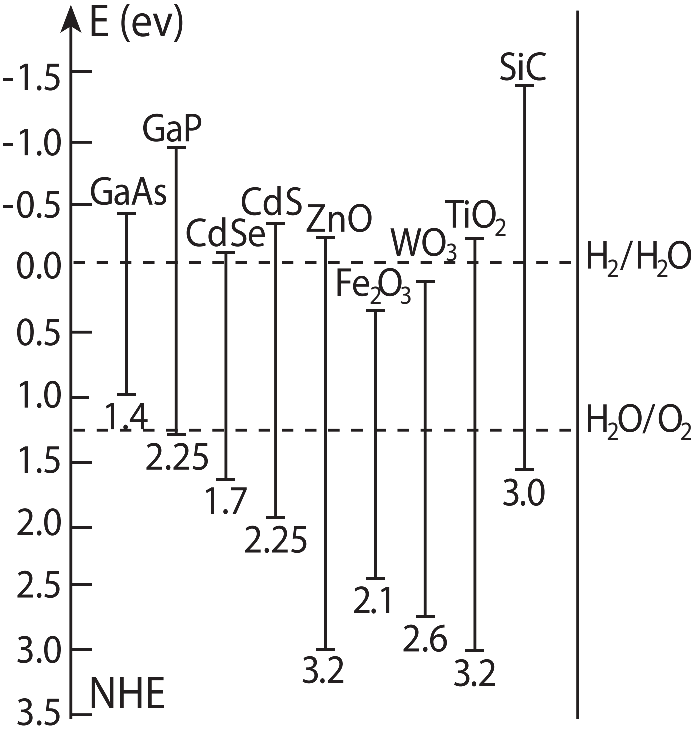

Figure 5.1: Comparison of various semiconductors versus the band potentials for the water oxidation and hydrogen reduction potentials.

The latter criterion is particularly important and we have focused on using lasers to dope and structure TiO_2 initially to meet the stability criterion. We will show our work with dopants and host metal oxides later in this chapter.

We have shown in Chapter 2 that femtosecond laser hyperdoping introduces high concentrations of dopant atoms into host materials, which can effectively change the electronic structure and creates large area surface structures. We envision the femtosecond laser texturing technique will provide greater surface area both for light trapping and for more reaction sites, thus increasing the photocurrent during water splitting even without the introduction of dopants.

Large bandgap, early transition metal oxide catalysts have been extensively studied as the photoanode in water splitting experiments. In Chapter 4, we discuss TiO_2 as being one a few materials that can be used in a photoelectrochemical (PEC) cell. We previously attempted doping with nitrogen in Chapter 3 but found that the chemical selectivity kept it from occurring. Another method of doping TiO_2 to alter the bandgap is to substitute another metal for titanium. [154, 155] The major contributor to the overall low efficiency is a lack of sub-bandgap photon utilization; our goal is to lower TiO_2's optical band gap into the visible via femtosecond laser processing.

Many researchers have attributed the failure of doped TiO_2 as a photoanode to a change in the structure, catalytic activity, or energy level. The goal of this chapter is to motivate that problem in the materials may be as simple as lifetime. We choose to focus on $3d$ transition metals, in particular, Cr, Mn, and Ni, as dopants. [156, 157] Our decision to focus on a series of $3d$ metals in this work is driven by our interest in studying the chemical selectivity that occurs during the hyperdoping process. [35] $3d$ transition metals have states that lie within the band gap of TiO_2; introducing the metals into the oxides is therefore expected to yield band gap lowering. [155, 158–160]

Driven by this prospect, we aim to reduce the band gap of TiO_2 by way of Cr, Mn, and Ni doping and determine the influence of these inclusions on light-driven water oxidation. [161–163]

After showing that transition metal doping in TiO_2 is effective, we plan to extend our method to a variety of other metal dopants and to other material systems, namely Fe_2O_3. In other materials besides TiO_2, where the band position is not properly aligned with the O_2/H_2O level, the change in the band position change afforded by femtosecond laser processing could also further boost the charge injection ability of the hole to the O_2/H_2O redox by realigning the valence band to match the O_2/H_2O level more favorably.

The ultimate goal of our research is to use solar radiation to efficiently drive the water splitting reaction. In order to demonstrate this function and quantify the efficiency, we built a photoelectrochemical (PEC) device using our doped metal oxide as the photoanode to test the benefit gained. We also study the chemical composition by using X-ray photoelectron spectroscopy to look at the dopant incorporation and chemical oxidation state.

5.2 Experimental Procedure

To produce metal-doped TiO_2, we first use electron-beam evaporation to deposit 30 nm of a dopant metal the titanium foil. After e-beam evaporation, we irradiate the entire metal stack in square areas of 1 cm^2 with a 1-kHz train of 100-fs, 805-nm laser pulses from a Ti:sapphire laser with a fluence of 1.5 kJ/m^2 for the Mn sample and 2.5 kJ/m^2 for the Cr and Ni sample with a coverage of 50 shots per area. All samples are irradiated in ultra-high purity oxygen at a pressure of 100 Torr. For the undoped sample, we irradiate the titanium foil with the same laser parameters as described above. [164] We use the same setup shown in Fig. 4.3 and described in Chapter 4. [35] We then anneal the samples after laser treatment in a tube furnace heated to 1000 K for one hour with 300 sccm of high purity air flowing.

We will use scanning electron microscopy for a direct visualization of the nanostructured surface.

We measure the emitted Raman spectra excited with 633 nm light, produced from a HeNe laser. We record the Raman spectra in a backscattering geometry through a 20X microscope objective, where the data is projected onto a charge-coupled device array using a 2400 grooves/mm diffraction grating.

We collect and analyze the elemental content on a monochromatic aluminum-Kα (1486.6 eV) X-ray photoelectron spectrometer equipped with a 180° double focusing hemispherical analyzer. We perform survey scans with a 400-μm spot size, a band-pass energy of 50 eV, and a step size of 0.1 eV. We calibrate the samples with the adventitious carbon 1s peak (284.6 eV). [130]

To test the samples in the photoelectrochemical setup, we first back contact our samples individually with titanium wire and epoxy (protocol in Ref. [131]) in order to only study the reaction occurring on the laser-processed areas. We examine our doped TiO_2 in a three-electrode configuration using reference (Ag/AgCl) and counter (Pt) electrodes, which allows precise kinetics extraction of the solar-to-water oxidation activity. We compare the current-voltage data measured in dark (no illumination) and light (illumination) condition using a UV LED, centered at 405-nm, and an

AM 1.5 filter-equipped solar simulator. The difference measured between the dark and light current gives the photocurrent as a function of voltage. In the quartz photoelectrochemical cell, we use 0.1 M KOH as an electrolyte, which emulates the alkaline electrolyzer condition widely used in industry for water splitting. We have already seen that the TiO_2 produced by femtosecond laser irradiation of titanium is electrochemically stable in a variety of different solutions. [35] To operate our photoelectrochemical device, we use a power supply (potentiostat) to apply a bias while measuring the photocurrent created during the oxidation reaction. From this information, we study how the photocurrent, which directly probes the photon-to-fuel conversion rate, varies with potential.

We combine this analysis with the external quantum efficiency measurement. In the quantum efficiency measurement, the monochromator splits the illumination light into individual wavelengths, as shown in Fig. 5.2. By comparing the photocurrent as a function of wavelength, we can systematically determine the efficiency in the ultraviolet region in comparison to that in the visible. If the dopant atoms act as expected in the theory, the incorporation of metal dopants should allow the doped TiO_2 to achieve higher quantum efficiencies than undoped TiO_2 in the visible region.

5.3 Results

In this section, we will first report on the doping of TiO_2 and the characterization of the materials made. We will then show photoelectrochemistry of the samples, including wavelength-dependent water oxidation. Lastly, we will extend the laser doping method to Fe_2O_3 by laser structuring iron films in oxygen and show its photochem-

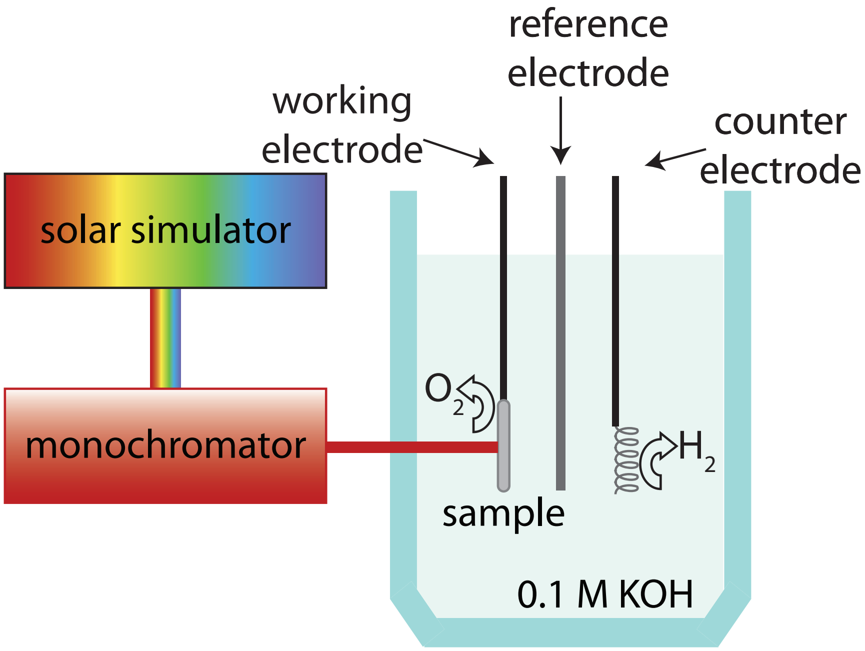

Figure 5.2: Wavelength-dependent photoelectrochemical cell with a three-electrode configuration.

istry.

5.3.1 Laser doping of TiO_2

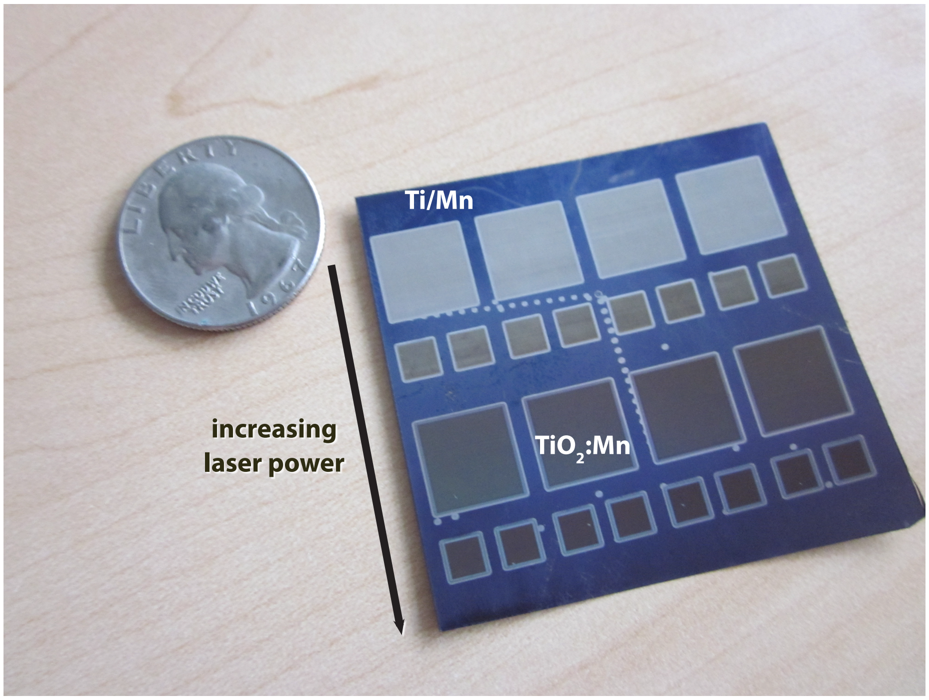

Figure 5.3: TiO_2 doped with Mn metal, shown with increasing laser fluence from top to bottom of the sample.

We first start with doping with manganese (Mn) as shown in Fig. 5.3. By increasing the laser fluence, we see that the absorbtance of the doped material increases and the squares become darker.

We then apply the same method to a variety of other metallic dopants, including Cr, Ni, and Mo. To see the surface structure formed from laser irradiation, we show four materials as produced in Fig. 5.4. We see that the surface structures appear very similar and the LIPSS are on the order of the undoped materials, shown in Fig. 3.3. [35]

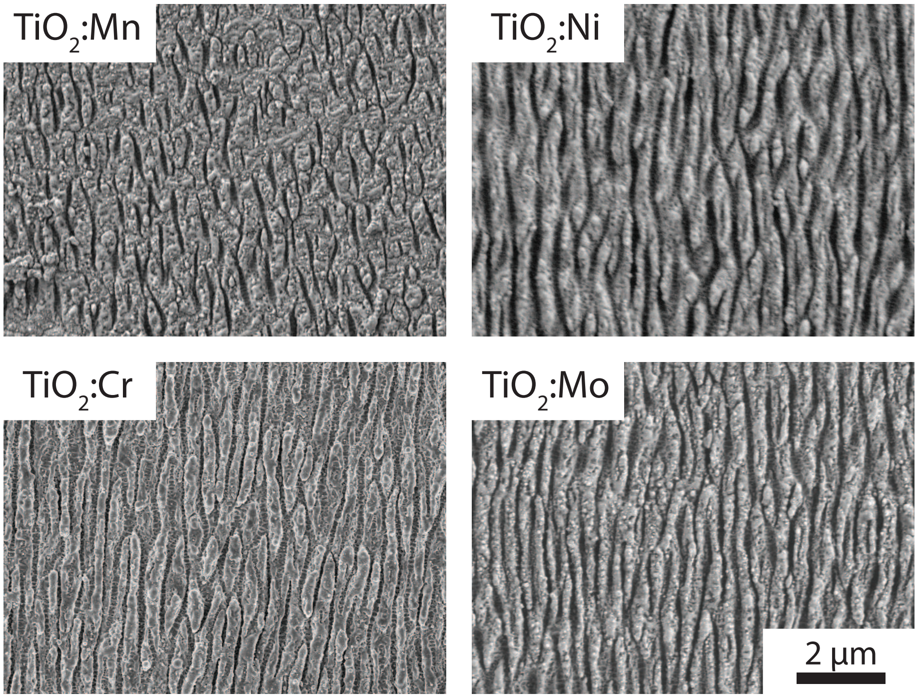

Figure 5.4: SEM images of different doped metals in TiO_2.

To present the chemical state of the samples, we present high-resolution X-ray photoelectron spectra for the 2p peaks of titanium and the dopant metals in Fig. 5.5. Through analyzing the binding energy values of titanium and the specific dopants, we can identify the oxidation state of the materials tested to determine their chemical makeup. For titanium (Fig. 5.5a), the doped and undoped TiO_2 look comparable with peaks for Ti $2p_{3/2}$ and Ti $2p_{1/2}$ peaks at 458.7 and 464.3 eV respectively, which correspond to the Ti^{4+} the oxidation state found in TiO_2. [135] Due to the doped materials' similarity with that of the undoped TiO_2, we believe that the majority of the Ti has been converted to TiO_2 irrespective of the dopant type within the probe depth of 5–10 nm. [137]

We now examine the specific peaks for each dopant in its respective doped material. In Fig. 5.5b, we show the Mn 2p spectrum to understand the nature of the manganese atoms in the TiO_2. Using the Advantage program, we deconvolute the $2p_{3/2}$ peak into three curves that are centered at 641.2, 642.5, and 645.1 eV. The 641.2 and 645.1 eV peaks correspond to two of the multiplet peaks for the +3 oxidation state, and the 642.5 eV peak corresponds to the +4 oxidation state. [165, 166] In Fig. 5.5c, we show the Cr 2p data. For the Cr $2p_{3/2}$ peak, we deconvolute the data into two peaks at 577.6 and 580.6 eV, which correspond to the +3 and the +6 oxidation states. [167] Specifically, for the 577.6 peak, we can attribute this specific binding energy to the hydroxide, as opposed to the oxide state, which sits at a lower binding energy at 575.7 eV. [167] Lastly, in Fig. 5.5d, we present the Ni 2p peaks. The binding energies for Ni $2p_{3/2}$ are quite complicated with each state having multiplets. We fit the peaks to multiplets at 862.0 and 855.9 eV, which correspond to the +2 state, specifically for $Ni(OH)_2$. [168] There is no peak at 852.6 eV, which is the major metallic Ni peak. [169] Along with the Ti 2p data, we show that the dopants are partially oxidized within a fully-oxidized TiO_2 material.

We see that each of the dopants occupies non-metallic oxidation states, although the oxidation states differ for each metal. Specifically, TiO_2:Mn (+3/+4) and TiO_2:Cr (+3/+6) consist of a mix of two oxidation states, which points to the non-equilibrium nature of these dopants' incorporation in TiO_2. Likely, the Mn and Cr dopants are distributed throughout the material in various positions, which allows a distribution of oxidation states to co-exist in the same material. For the TiO_2:Ni, we see only the +2 oxidation state, meaning that we have created a more stable material than that of TiO_2:Mn and TiO_2:Cr. Due to the possible mix of oxidation states formed in femtosecond-laser doping, we see the unique capability of the femtosecond laser treatment, which allows a synthesis of non-equilibrium material that would otherwise be unobtainable with bulk synthesis.

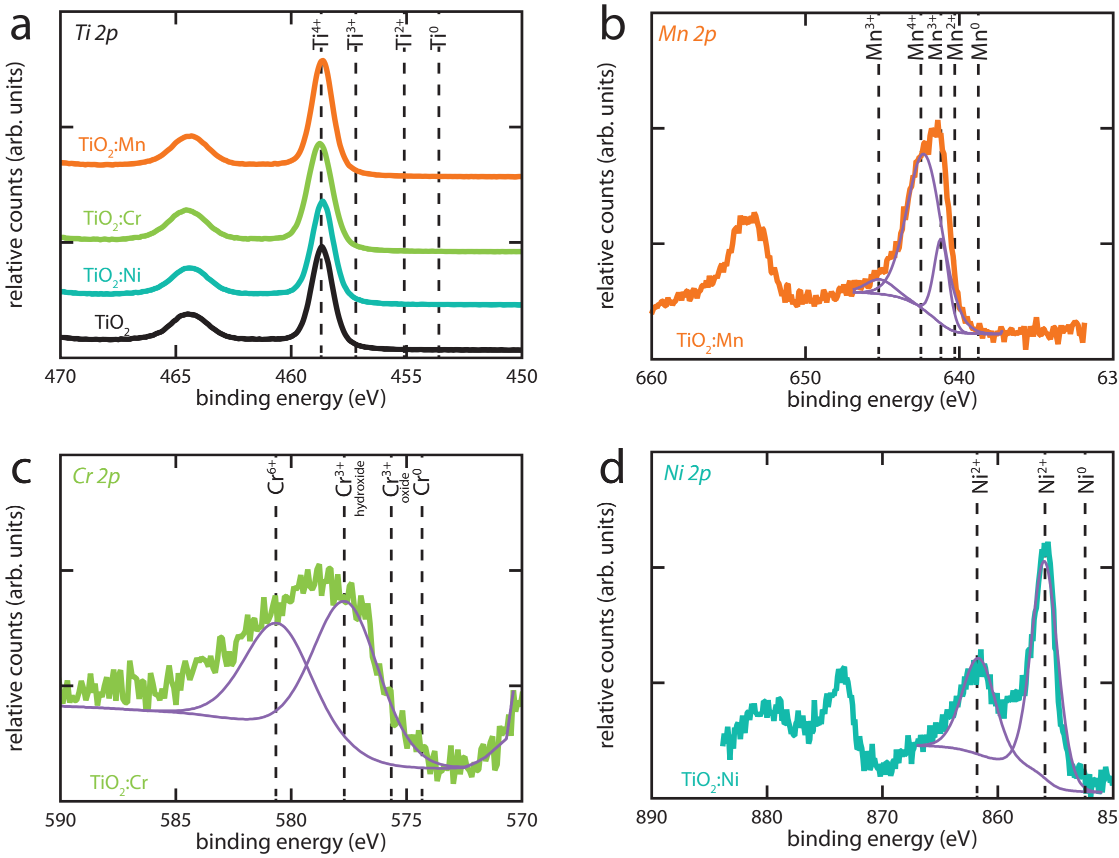

Figure 5.5: High-resolution XPS scans of all undoped and doped TiO_2 samples for (a) Ti 2p peaks and the various dopants in the respective samples measured: (b) Mn 2p in TiO_2:Mn, (c) Cr 2p in TiO_2:Cr, and (d) Ni 2p in TiO_2:Ni.

We have previously shown that our laser hyperdoping-processing technique results in amorphous films in Chapter 4. To control this aspect, we determine if annealing a sample can lead to a change in the crystallinity. As both grain size and orientation are critical to photocatalysis, we need to have a crystalline material to achieve a higher rate of water oxidation. [170, 171] We first started with the TiO_2:Mn samples and annealed the samples at different temperatures to see the formation of the rutile crystal phase in Fig. 5.6. We never see the anatase crystal structure form, which should have occurred above 250° C. [172]

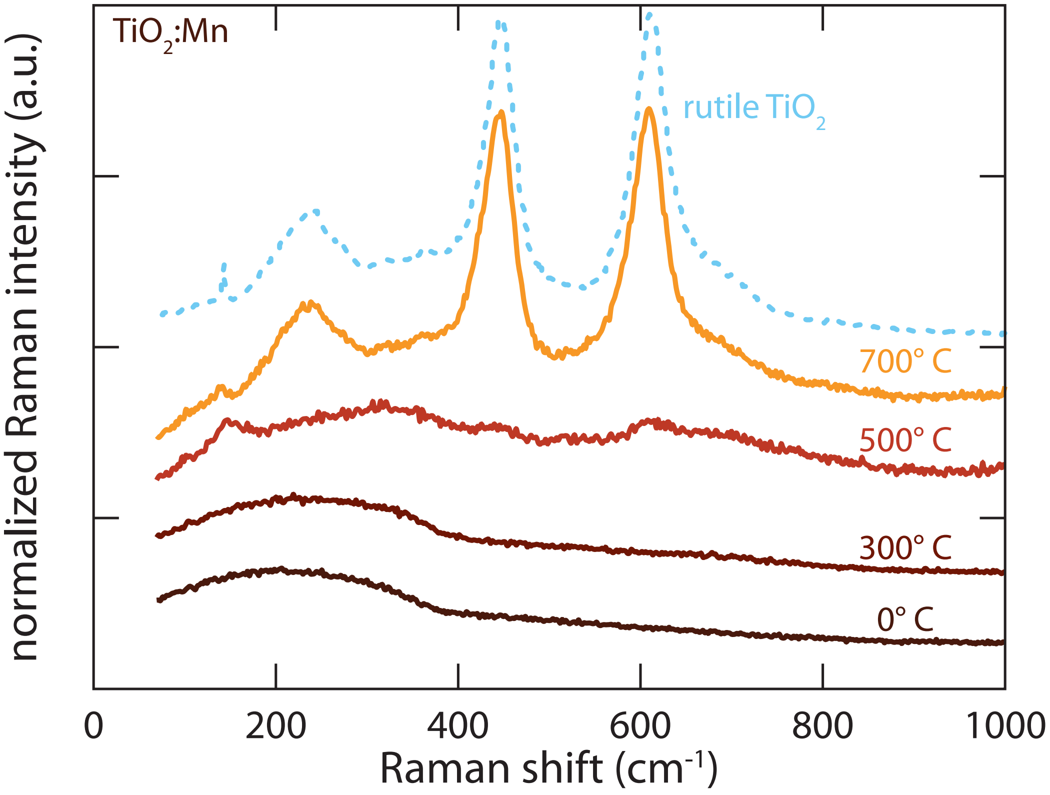

Figure 5.6: Raman spectra of various TiO_2:Mn samples, annealed to different temperatures, which shows the emergence of the rutile peaks at 700° C.

We see the Raman spectra in Fig. 5.7 for the doped and undoped materials, shown with a bulk rutile crystal (111) and unannealed titanium foil (Ti) for reference. For all of the other samples, which were annealed at a temperature that achieves the rutile structure (700° C), we observe broad peaks around 240, 447, and 612 cm^{-1}, which are indicative of the rutile phase of TiO_2. [118] We also observe a broadened peak around 135 cm^{-1}, which we attribute to titanium metal and shows that the 633-nm excitation wavelength is penetrating beneath the surface structures and probes the underlying titanium foil. [120] Due to the similarity in the doped and undoped materials, we believe that all of the materials laser-irradiated and annealed are composed of a surface rutile TiO_2 layer with titanium underneath.

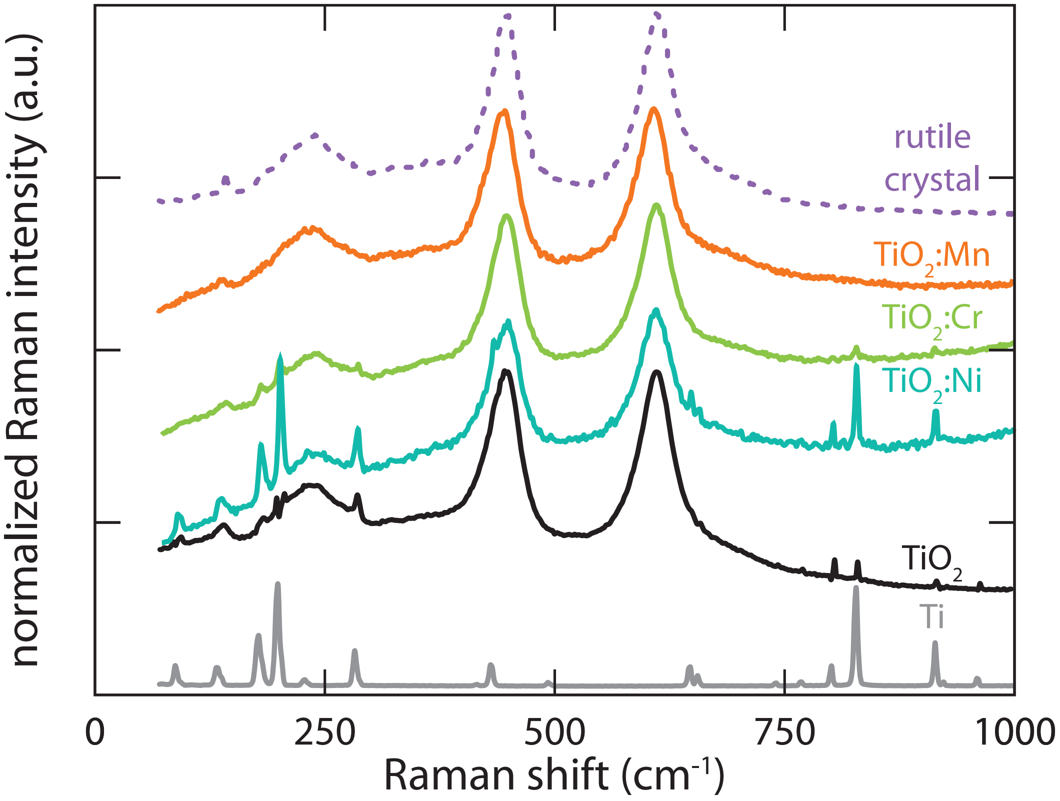

Figure 5.7: Raman spectroscopy of the laser doped samples, excited by 633 nm light. Rutile data is from a rutile TiO_2 (111) crystal.

We also see a few other low intensity peaks at 179, 200, 283, 800, 828, and 913 cm^{-1}, which we cannot attribute to any TiO_2 crystal groups but all appear in our titanium substrate and hence are background peaks that we will not consider further in this study. Interestingly, we see higher signal from the substrate peaks in the TiO_2:Ni than any of the other laser-irradiated samples which might suggest that there is more titanium in the Raman probe depth and hence that the surface layer of TiO_2:Ni is thinner than the other samples.

5.3.2 Photoelectrochemistry

To study the UV photochemistry, we irradiate the samples with 405-nm light and show the resulting photocurrent for each material in Fig. 5.8 by taking the difference between the current under illumination (light) and no illumination (dark). We sweep the applied potential difference from –0.9 V to +1.0 V vs. Ag/AgCl and measure the current produced. The undoped TiO_2 and TiO_2:Ni have similar photocurrents at 405-nm. By doping the material with Mn or Cr, we lower the overall photocurrent significantly.

To calculate the Incident-Photon to Conversion Efficiency (IPCE), we measure the photocurrent generated as a function of wavelength. We sweep the wavelength of the excited light using an AM1.5 solar simulator with a monochromator attached. The IPCE takes into account how many photons at wavelength are emitted from the AM1.5 lamp and shows how many of those photons are then converted to electrons, in the form of the photocurrent. The IPCE for the undoped TiO_2, TiO_2:Cr, and TiO_2:Ni are shown in Fig. 5.9. For the above bandgap light (λ<400 nm), the undoped TiO_2 and TiO_2:Ni are very efficient at photon conversion and show a high IPCE. At longer wavelengths, which correspond to below bandgap photons, there is some conversion of photons to current between 400–500 nm, which may be from oxygen vacancies in the material.

For the TiO_2:Cr sample, there is hardly any photocurrent for above-bandgap

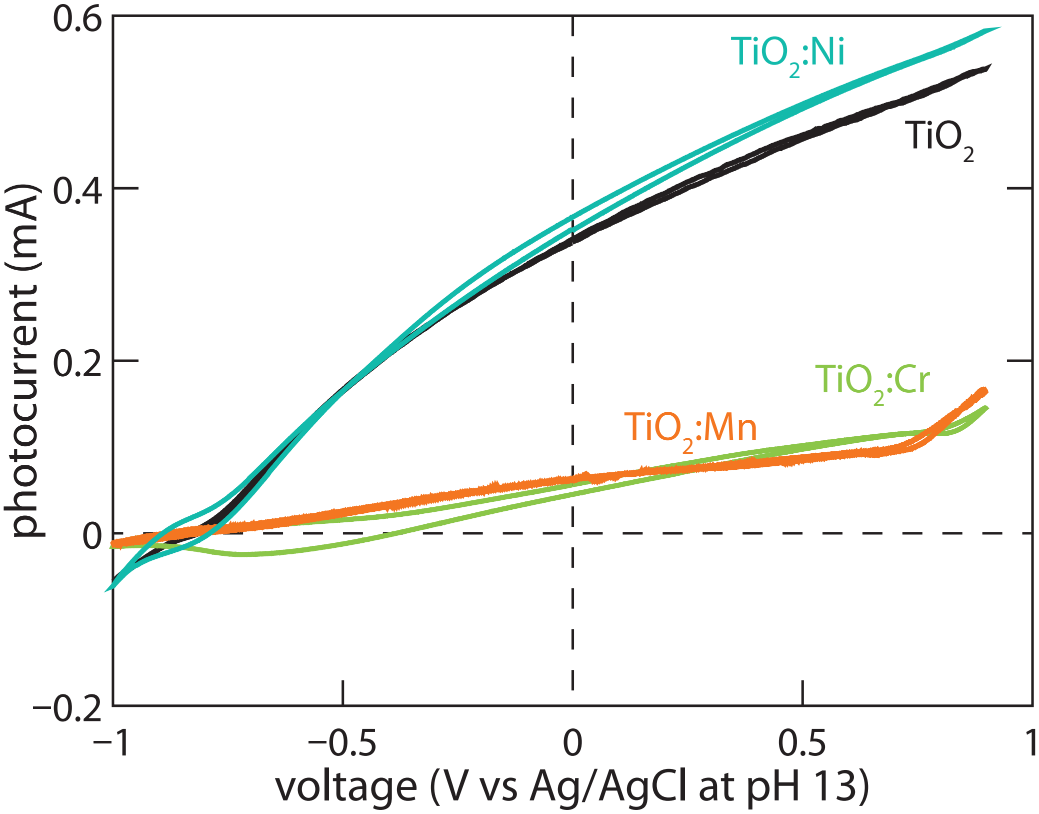

Figure 5.8: PEC measurement of laser doped TiO2. Three-electrode photoelectrochemical measurement with excited light from 405 nm LED in 0.1 M KOH solution.

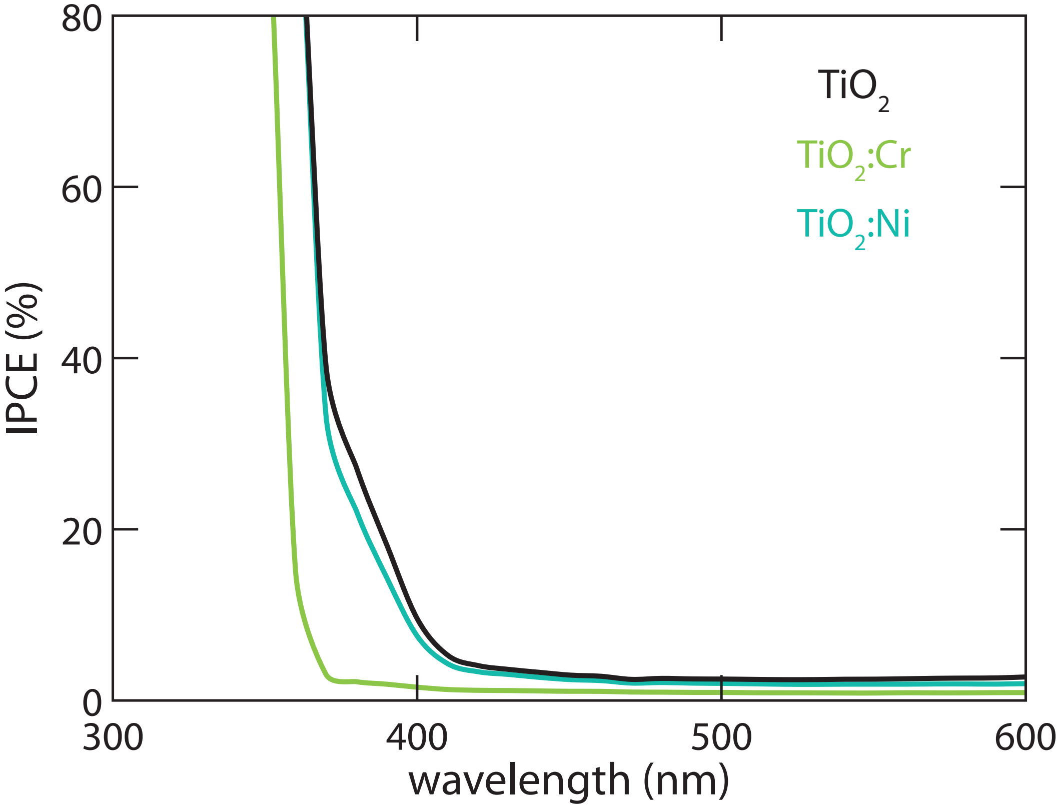

Figure 5.9: IPCE of various samples, calculated from wavelength-dependent PEC measurements.

energies, which we previously saw in the low photocurrent at 405 nm in Fig. 5.8. The IPCE is also very low for all wavelengths, including the above bandgap photons. This lower photocurrent shows that there are significant current losses when the Cr dopant is in TiO_2 and shows that there are drastic differences between using Ni and Cr as dopants.

Previous results have shown that the TiO_2 produced by femtosecond laser irradiation of titanium is electrochemically stable in a variety of different solutions. [35] Over the course of the experiment, there was no sign of TiO_2 degradation. This excludes the possibility that the photocurrent is due to self-oxidation. We therefore attribute the photo-oxidation current to be due solely to the oxygen evolution reaction (OER):

$$4OH^- \rightarrow O_2 + 2H_2O + 4e^-. \tag{5.1}$$

In addition to the simple doping above, we also pre-annealed the TiO_2:Cr and TiO_2:Ni by annealing the two-metal layer stack after evaporation but before laser treatment. The resulting water oxidation is shown in Fig. 5.10. By pre-annealing the samples, we hoped to diffuse the dopants farther into the titanium metal and hence increase the photocatalysis. In actuality, the pre-annealing helped the TiO_2:Cr sample while hurting the TiO_2:Ni sample. Due to the decrease in the Ni samples water oxidation, the pre-annealing must have affected the final dopant oxidation state.

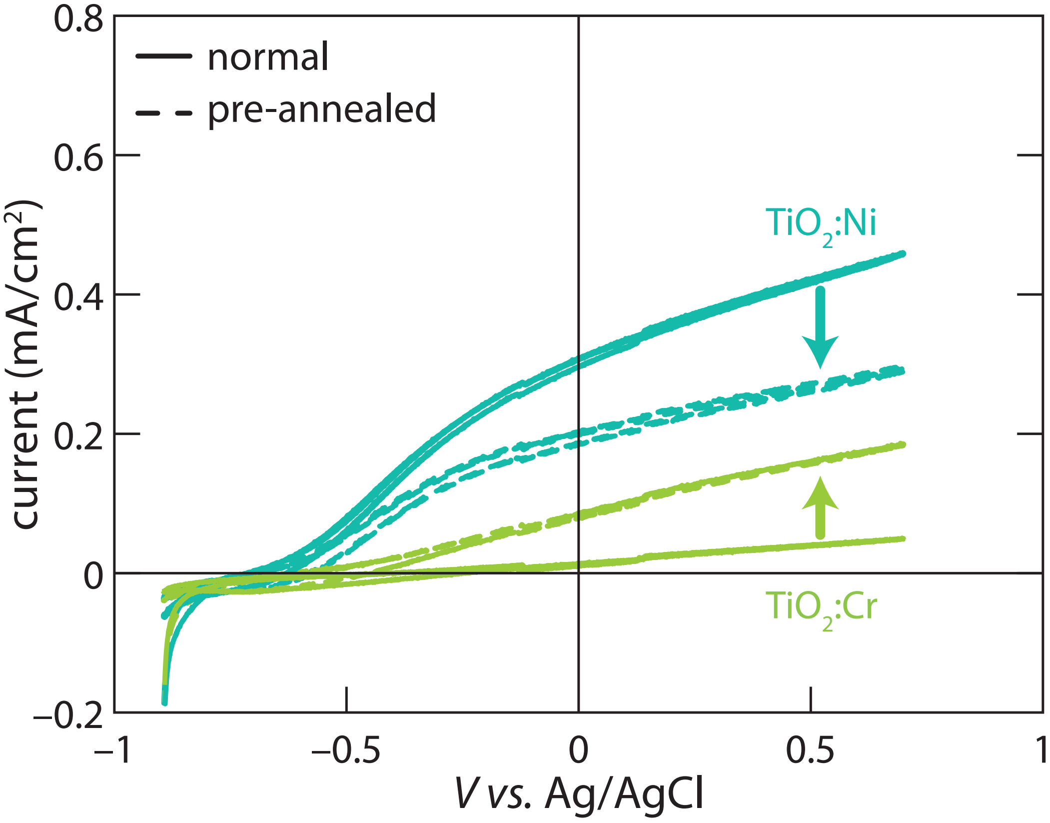

Figure 5.10: PEC measurements of different doped materials in TiO_2 with pre-annealing of 700° C for 1 hour versus the normally-produced samples

5.3.3 Doping of other oxides

After focusing on TiO_2, we extend the method to oxidizing a variety of metal foils. We work with copper, iron, and niobium films and were able to oxidize each of the films with femtosecond laser irradiation. For the photochemistry experiments, we back-contacted each sample as described above and tested the samples in the same photoelectrochemical setup in Fig. 5.2. The photocurrent was extremely low for the laser-treated copper and niobium films, but we saw immediate bubble formation (Fig. 5.11) for the laser-treated iron film.

Figure 5.11: Bubble formation on laser-formed Fe_2O_3.

Due to the bubble formation, we decided to study the iron films further. After chemical analysis, we found that the iron foil laser-irradiated and then annealed forms iron oxide, Fe_2O_3. Iron oxide (Fe_2O_3) has received substantial attention as a candidate for water-splitting but has suffered from its extremely short hole lifetime. [173] To improve the material, we dope Fe_2O_3 with Ti by laser structuring an iron film that had titanium metal evaporated on it in the presence of oxygen gas. After annealing, we compare the water oxidation in Fig. 5.12 and see that the Fe_2O_3:Ti has a lower photocurret at the oxidation potential (H_2O/O_2) than the undoped Fe_2O_3.

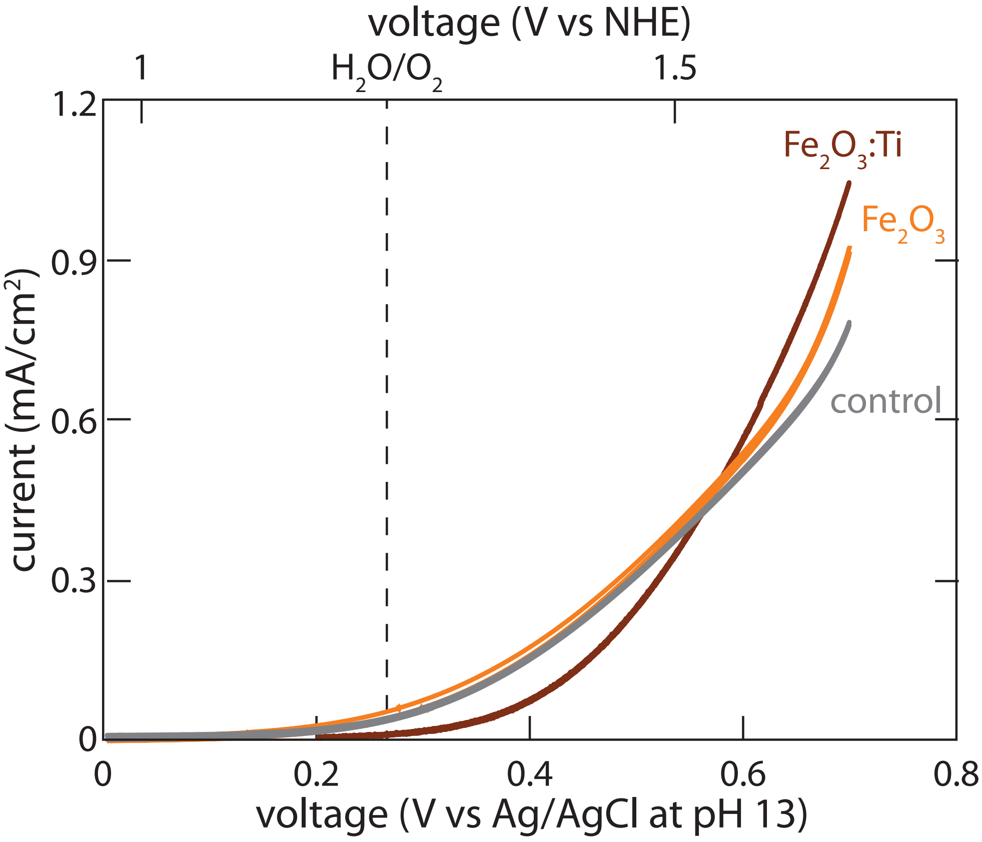

Figure 5.12: PEC measurements of doped and undoped Fe_2O_3.

In fact, we do not see the same overall water oxidation that we see in the laser-doped TiO_2; however, with the bubble formation at high overpotentials, water oxidation is occurring. Both the laser-doped TiO_2 and Fe_2O_3 show water oxidation but with doping, we see that the oxidation decreases, even with above-bandgap excitation.

5.4 Discussion

Our result has shown that the incorporation of dopants does not lead to significantly higher water oxidation when illuminated but that the type of dopant incorporated does lead to a change in water oxidation efficiency for both TiO_2 and Fe_2O_3. Specifically for TiO_2, with the incorporation of Mn and Cr, we see a drastic reduction in the photocurrent at 405 nm, which translates to a very low IPCE in the visible. With Ni as a dopant, we see a similar water oxidation rate at 405 nm when compared to the undoped TiO_2, but the overall IPCE is lower across many wavelengths. The importance of the composition of the catalytic materials on the water oxidation activity is well-known in the catalysis community. [174] To ensure the high catalytic activity of doped TiO_2, it is critical that we precisely control the dopant, which is challenging with the femtosecond laser doping process.

The placement of the dopant oxidation state in the bandgap is critical to the overall water oxidation because the dopant state must be below the OER energy to ensure that the reaction occurs. According to Mizushima et. al., only the $Ni^{+2/+3}$ ions have the correct placement in the bandgap. [156] Studying the oxidation states of the dopant metals from the X-ray photoelectron spectra shows that the $Mn^{+3/+4}$

and $Cr^{+3/+6}$ do not lie in the correct band placement. The Mn states are above the OER so water oxidation should be impaired with Mn as a dopant. For Cr, the Cr^{+3} state is placed right above the valence band and could be well situated if it was the only state that exists. With the addition of Cr^{+6} states, we see that the oxidation rate plummets. Therefore, it is the specific dopant oxidation state and its placement in the TiO_2 lattice that dictates the resulting water oxidation rate.

The challenge in developing doped TiO_2 lies in the possible instability of the dopant in the host TiO_2. [175, 176] As a result of this instability, the dopant may segregate and form a secondary phase. The phase separation is deleterious for the intended electronic structure control of TiO_2, where instead of doped TiO_2, we arrive at a two-component metal oxide, such as $Cr_2(OH)_3$ and TiO_2 mixture instead. In the non-interacting, diluted doping limit, each dopant should be ionized and thus each Cr atom is expected to contribute one hole. This assumption however relies on obtaining proper stoichiometric control, which must be optimized to minimize the contribution from oxygen defect. [177] Nonetheless, in the diluted doping limit, we expect that the conductivity of doped TiO_2 should increase, reflecting improved state availability due to dopant state formation.

5.5 Conclusion

To summarize, we extend the innovative femtosecond laser processing technique to fabricate photoelectrochemical materials. (1) We utilize femtosecond laser hyperdoping and texturing to dope metal oxides—specifically titanium dioxide and iron oxide. (2) We test our newly created materials in a photoelectrochemical cell to determine which dopants and host materials yield the highest water oxidation rate.

We incorporate Mn, Cr, and Ni into TiO_2 and Ti into Fe_2O_3 but do not see enhanced photocurrent from the addition of the dopants. Although metal dopants can be incorporated into the lattice, it is the specific oxidation state of the dopant and its placement in the oxide that dictates the overall water oxidation rate. More research is needed to explore the material properties in doping that affect the water oxidation reaction further into the visible.

CHAPTER 6

FEMTOSECOND LASER TEXTURING FOR BIOLOGICAL APPLICATIONS

Many advances have been made in surface structure and treatment titanium for implantology. However, higher levels of cell integration are needed to improve the predictability and longevity of implants, especially for dental applications. This chapter shows a new method for improving the surface structure of titanium through irradiation with a femtosecond laser. The main goal is to determine if cells can adhere and then proliferate on a new nanostructured titanium surface as compared with unstructured surfaces for applications in the dental industry.

6.1 Introduction

Chapter 3 examines the influence of oxygen and nitrogen gas composition on surface morphology, chemical composition, and stability of femtosecond laser irradiated titanium surfaces. Scanning electron microscopy show laser-induced periodic surface structures that do not vary with the background gas. [35] *Sul et. al*. concludes that the optimal oxide thickness of a porous surface structure is in the range of 1–5 microns with an optimum porosity of in the range of 19–30% with a pore size of less than 2 microns. [178] With the laser-treated TiO_2, we have found the surface strutures periodicity to be on the order of 268 nm, which is below the necessary pore size for cell adhesion.

In addition, electrochemical stability tests are used to simulate biocompatibility, and we found that the TiO_2 films are very stable in Hank's solution, which is a solution that simulates the body's pH. [35] Specifically, we see in Chapter 3 that there is an immediate decrease in current when the potential is applied for laser-formed TiO_2, which indicates the formation of a passivation layer. Samples treated in oxygen stabilize at lower current densities than that of the unstructured titanium, which shows that the formation of a passivation layer is slower for the bare titanium than the laser-treated samples. Therefore, the laser-treated TiO_2 is more stable than untreated titanium in biologically relevant solutions.

The implications for improved cell adhesion and viability are extensive. Currently there are limitations to the diameter and length of dental implants due to the possibility the implant will not stick and need to be regrafted in the mouth, which is a more complex process the second time where the cells have grown back without attaching to the implant. Because it is harder to set an implant the second time, it would be ideal to improve the cell adhesion in the first implant surgery. Better cell adhesion in implants would yield an improved survival and success rate of implants and allow for less-invasive (shorter) implants that have a faster recovery time.

6.2 Experimental Procedure

Samples are prepared as described in Chapter 4 for non-doped TiO_2. Once the titanium is laser-irradiated, there is no annealing in order to keep the surface structures intact for testing. To compare the laser-treated sample, we use the titanium foil without laser treatment as a control. The samples are individually epoxyed to glass petri dishes and then seeded with approximately one million HeLa cells per sample in a biological cell media. The media consists of DMEM with 10% FBS and 1% Penicillin Streptomycin, which is a base media with nutrients and an antibiotic. The cells sit in this pink-colored media with the samples for 24 hours to grow onto the surface, as shown in Fig. 6.1.

To tag and identify viable cells, we use Calcein AM, which allows the viable cells to fluoresce green. We add Calcein before imaging with the following protocol:

1. Heat up HBSS for washing.
2. Reconstitute the Calcein AM dye. Add 20 μL DMSO to 1 vial containing 50 μg of Calcein AM, stored in the –20° C freezer.
3. Just before use, add the 20 μL of stock dye solution to 10 mL of HBSS.
4. Heat up the dye.
5. Remove cell media.
6. Wash cells in warm HBSS.

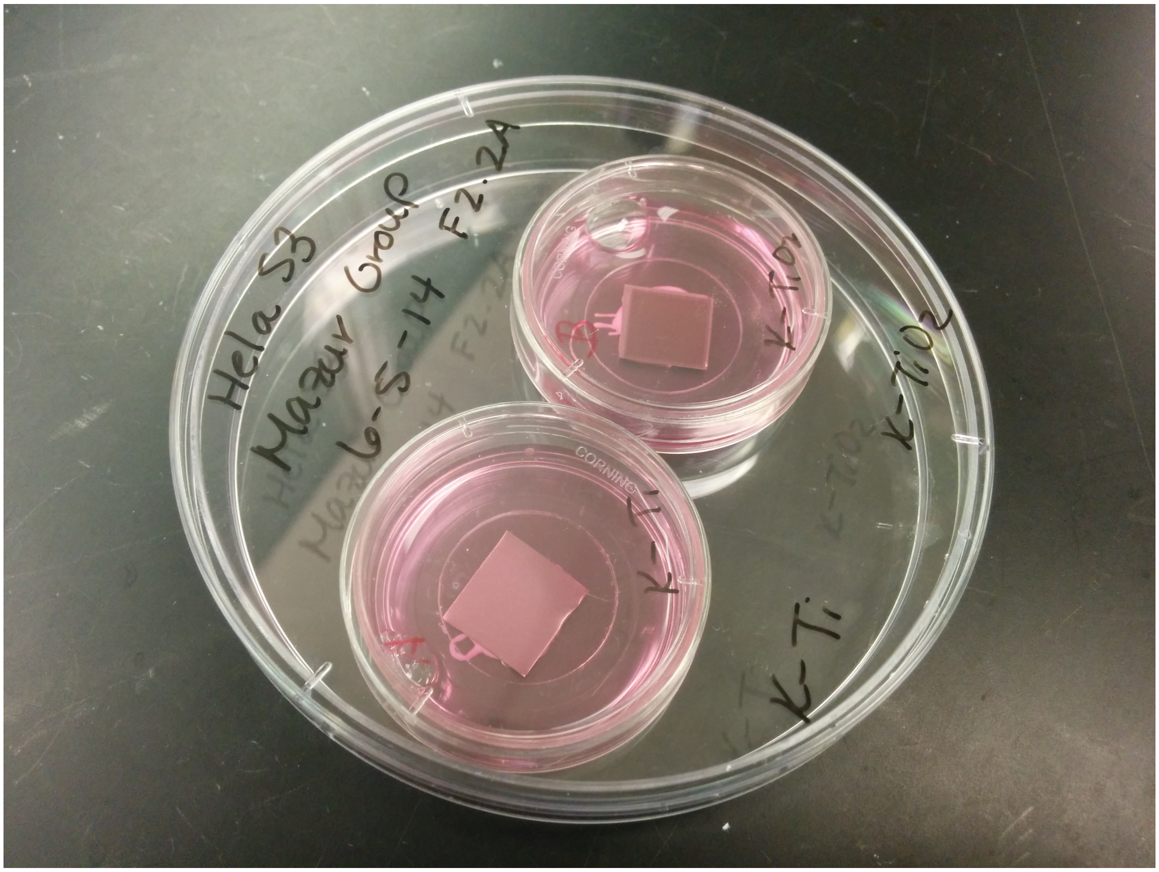

Figure 6.1: Titanium (left) and laser-treated titanium (right) in petri dishes plated with cell media.

7. Add 2 mL of Calcein AM solution to each 35 mm dish.
8. Incubate at 37° C for 20 minutes.
9. Remove the Calcein AM solution and wash with HBSS.
10. Place the cells in warmed HBSS or DMEM without phenol red.

To tag and identify non-viable (dead) cells, we use Propidium Iodide (PI), which allows the dead cells to fluoresce red. We add PI before imaging with the following protocol:

1. Make 3 μM PI stock solution from 4 μL stock (0.5 mg/mL) and 996 μL of fluorobrite DMEM.
2. Add 300 μL of PI stock solution in 2 mL of fluorobrite in petri dish.
3. Pipette 300 μL of PI working solution into sample with cells.
4. Cover samples and let sit for about 5 minutes for dead cells to show red nuclei.

We image the cells with a Nikon AZ 100M microscope with a 40X zoom, which consists of a 8x eyepiece with a 5x objective. We image in bright field and with two filters to see the green and red fluorescence separately. After imaging, we switch out the clear media with the cell media used above and allow them to sit for 24 more hours, in order to image again after 48 hours total.

6.3 Results

The surface structures formed by laser irradiation are shown in Fig. 3.3 with a cross-section, produced from Focused Ion Beam, shown in Fig. 6.2. From the cross-section, we see that the surface structures penetrate at least 500 nm into the material, giving good evidence that the oxide penetrates deeper than the untreated titanium foil's native oxide layer. From X-ray photoelectron spectroscopy, we are able to determine the thickness of the oxide layer is a minimum of 50 nm after Argon milling and subsequent measurements.

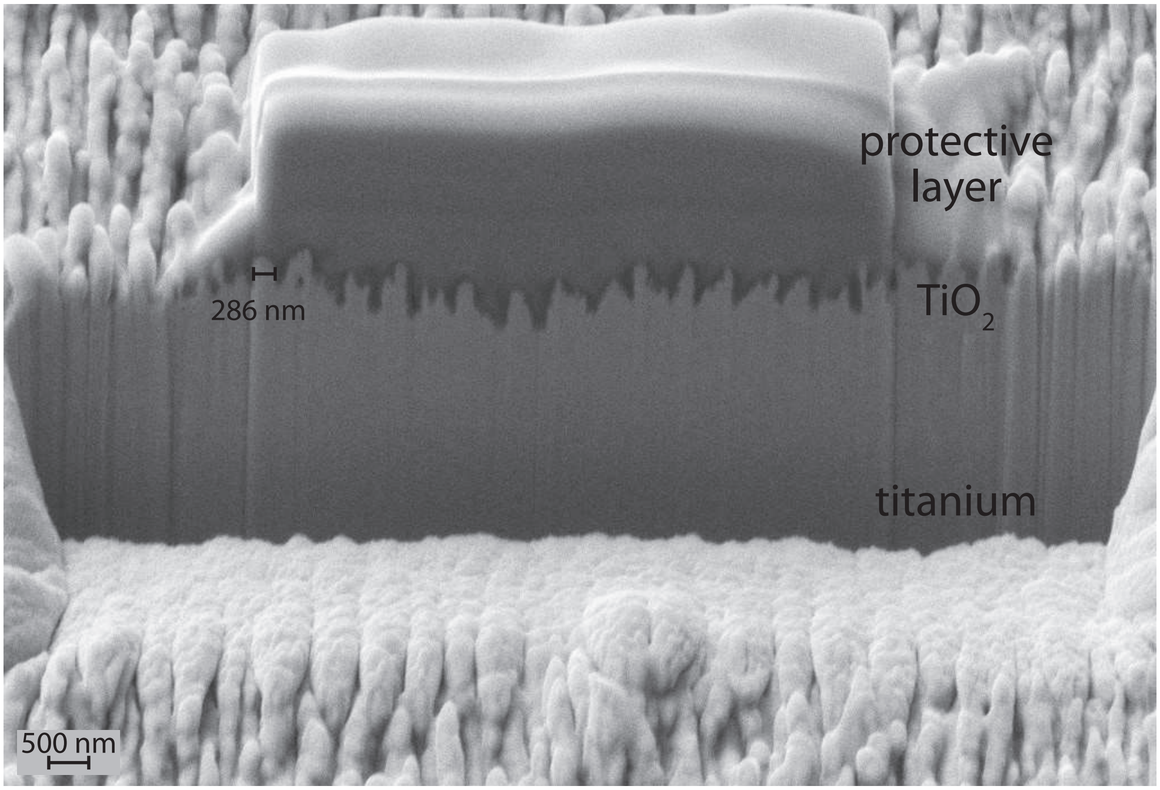

Figure 6.2: Cross-section of LIPSS on TiO_2, produced from samples similar to those in Ref. [35].

Pictures of the untreated titanium and laser-treated TiO_2 taken 24 h after the cell adhesion process are shown in Fig. 6.4. The top row shows the bright field image with the cells attached to the substrate surface. The middle row shows the alive cells stained in green dye, and the bottom row shows the dead cells stained in red dye (schematic of imaging setup shown in Fig. 6.3).

The laser-treated sample has a significant amount more of alive cells than the untreated titanium, showing that the cells prefer the laser-treated areas to grow. We also looked at the samples after 48 h, and the trend remains the same, though the total number of cells is lower.

In the bottom pictures in Fig. 6.4, we see that the untreated sample has more dead cells than the untreated but in relation to the proportion of alive cells, it would seem as if the total number of adhered cells is much lower in the untreated sample.

We also performed the same experiment with a sample with higher fluence (5.0 J/cm^2) and a doped, laser-treated sample from Chapter 4, TiO_2:Ni, and found that both samples exhibited cell viability levels similar to the laser-treated sample in Fig. 6.4. An average cell count for each sample is shown in Table 6.1. This helps to show that it is the laser treatment process that is keeping the cells alive and not the specifics of the laser power used.

As titanium metal forms a native oxide of TiO_2 naturally, we know that the untreated sample will have a thin layer of TiO_2 on its surface; however, in Chapter 3, we show that it is still not as stable in HBSS as the laser-treated samples. It can be concluded from this prevous experiment that the laser-treated samples provide a more stable environment while in the cell culture media for the 48 h they are not being imaged because the measurements in Fig. 3.8 were performed in the same HBSS

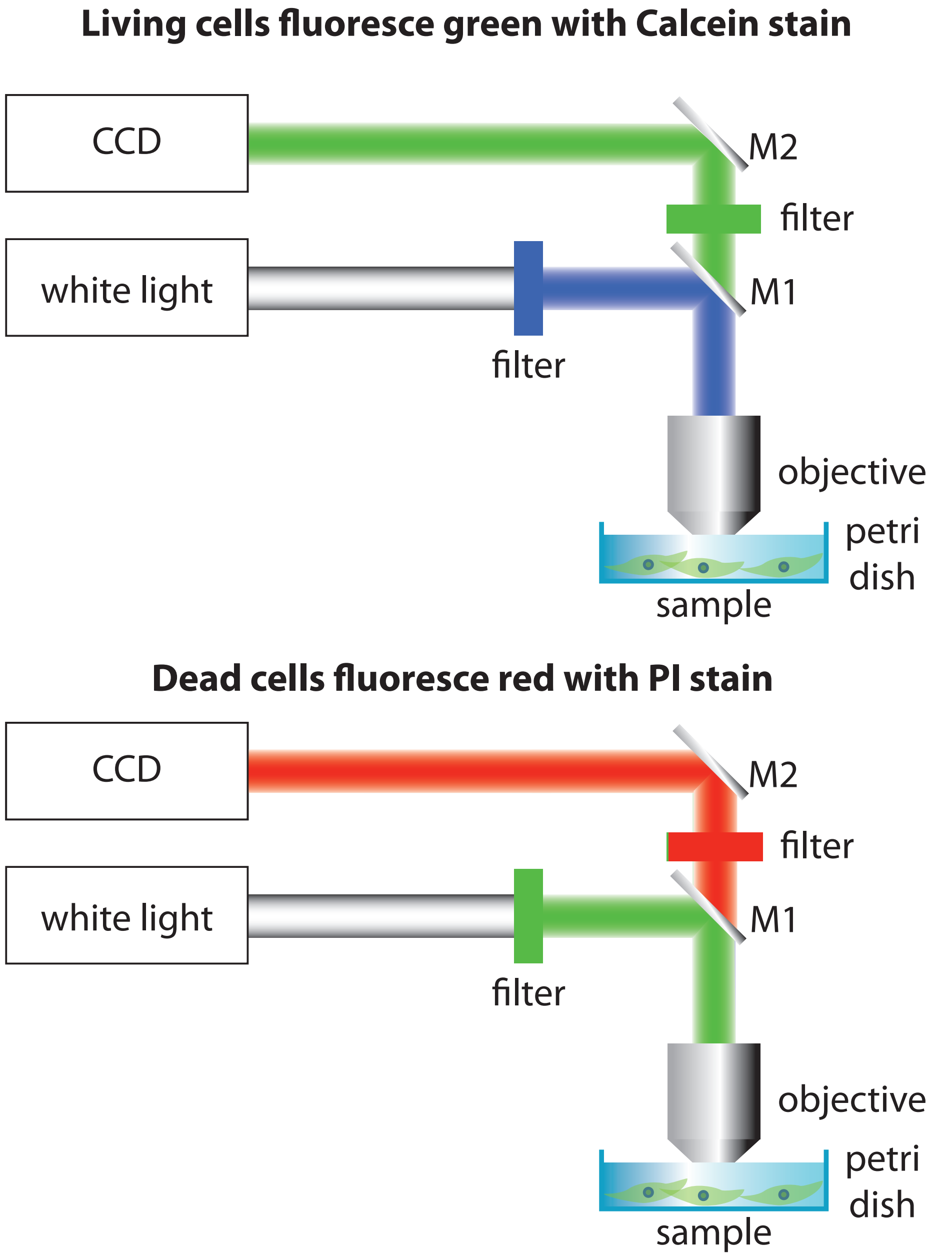

Figure 6.3: Imaging setup used for fluorescence pictures with both Calcein (top) and PI (bottom) stains.

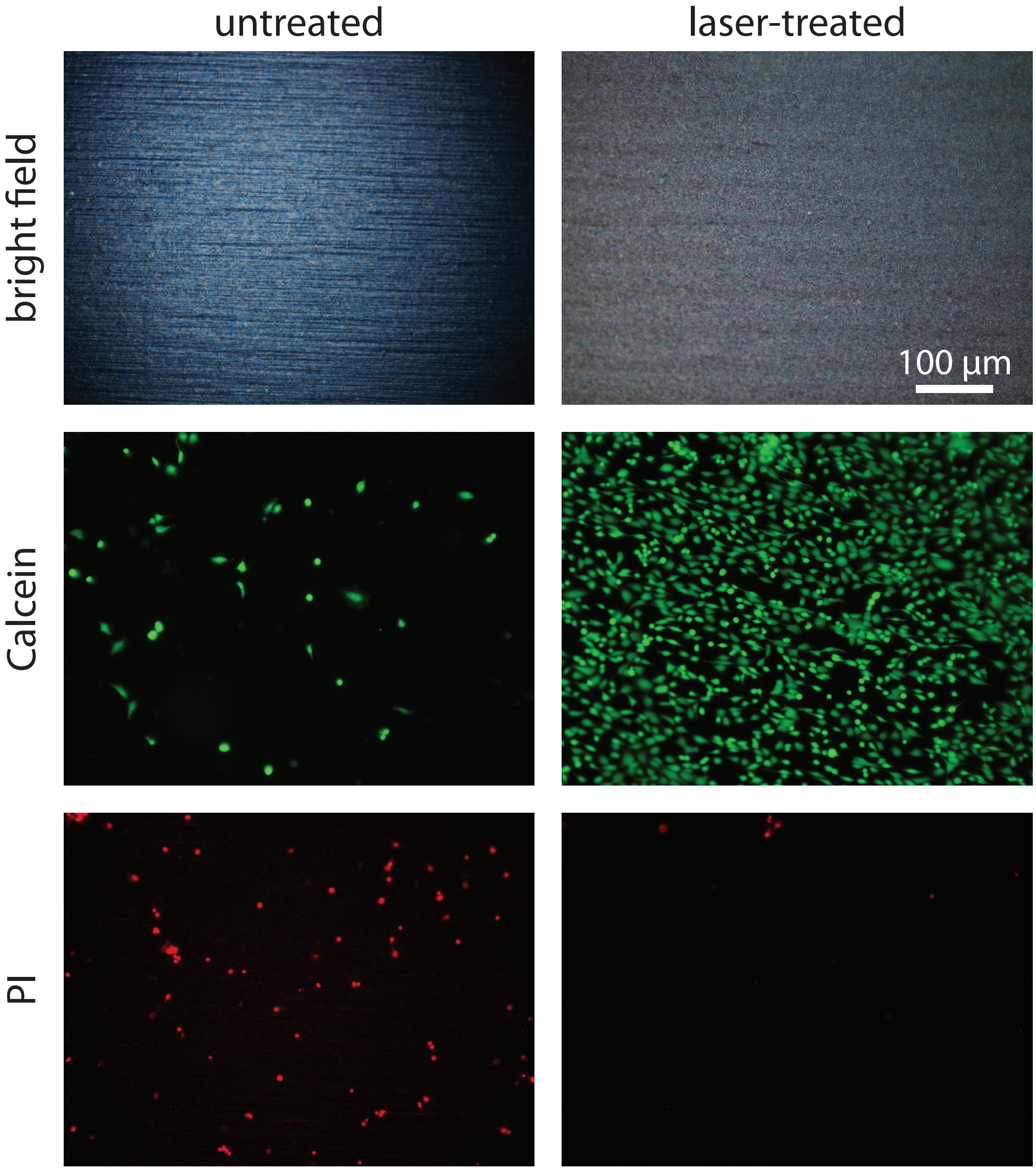

Figure 6.4: Same-area images of untreated (left) and laser-treated TiO_2 (right) with three filters: bright-field showing surface structure (top), a filter showing alive cells in green (middle), and a filter showing dead cells in red (bottom).

Table 6.1: Cell counts of three samples, including two laser-treated samples and untreated titanium. The cell counts are averaged over three images taken at various positions on the sample.

sample	living cell count	dead cell count
untreated	131	151
laser-treated	1047	31
higher fluence laser-treated	1169	61

solution used in the cell media.

Because we see a much higher total number of cells adhered on the laser-treated samples, we can conclude that it is the surface texturing that is most important in the cells' adhesion to the surface. By increasing the fluence of the laser and hence making the surface structures more defined, we do not see a huge improvement in the adhesion, showing that it is the formation of the LIPSS on the order of a few hundred nanometers that provide the most benefit for total cell adhesion.

6.4 Conclusion

This chapter shows how we can take advantage of our novel method of surface modification to create a surface architecture that cells thrive on. The results show that laser-treated titanium is an ideal substrate for implants. The laser treatment allows for more cells to adhere to the surface and live within a 48 h window. In addition, one of the main difficulties in other surface treatment methods for dental implants is a lack of reproducibility. With the laser treatment, a highly reproducible surface structure and composition can be fabricated. To move forward, we need to compare these results to sand-blasted titanium alloys that are used in the dental industry today and then test the laser-treating procedure on the titanium alloys to see if we can achieve similar results with FDA-approved dental implant materials.

CHAPTER 7

CONCLUSION

There is tremendous demand for novel water splitting materials and devices as we look for efficient, carbon-free energy storage methods. We believe that the laser-treating and nanostructuring of wide bandgap semiconductors like TiO_2 has promise as a platform for scalable and sustainable water splitting. Through this thesis, we present research to show that doping of TiO_2 and other oxides is possible but not completely controllable and that the resulting water oxidation is not as efficient with our laser-produced materials. Furthermore, because of TiO_2's stability, biocompatibility, and abundance, we show that there are applications both in chemical reactivity and implantology.

In this thesis, we first give an overview in Chapter 2 of the many methods of utilizing femtosecond lasers to process and change semiconductors across a variety of disciplines. We also explain the laser doping process, including the melting and ablation regimes. In terms of applications, we focus on surface modification, bulk modification, and deposition techniques. By describing how ultrafast lasers are operated in various industries, we present how using femtosecond lasers yields more precise and defined results across many disciplines and materials. We also briefly touch on the hyperdoping technique and how it relates to a variety of materials, including wide band gap semiconductors.

In Chapter 3, we first fabricate TiO_2 by laser irradiating titanium in the presence of oxygen. The samples created show enhanced absorption due to the creation of laser-induced periodic surface structures. We present a novel method for fabricating TiO_2 by beginning with a metallic titanium foil as our substrate and laser irradiating the foil in the presence of oxygen, yielding TiO_2 already back-contacted to the titanium substrate.

We also explore the incorporation of nitrogen into TiO_2 by irradiating both bulk TiO_2 and titanium metal in an oxygen- and nitrogen-rich environment with a femtosecond laser. We study the influence of atmospheric composition during femtosecond laser irradiation of titanium and find that changes in the gas composition alter the chemical composition of the resultant films, but the surface morphology is insensitive to gas composition and pressure. We demonstrate that irradiation of titanium in oxygen-containing environments forms a highly stable surface layer of nanostructured, amorphous titanium dioxide. However, our hyperdoped TiO_2 has a significant selectivity toward oxygen incorporation (Fig. 3.4), which displays strong competition against nitrogen incorporation. As a result, we are only able to incorporate nitrogen when there is no oxygen in the chamber. With the addition of air to the chamber, which is a combination of 20% oxygen and 80% nitrogen, there is no nitrogen incorporation. Even with only 1% oxygen and 99% nitrogen, there is still no nitrogen incorporation. We attribute this phenomenon to the stability of TiO_2 being much greater than that of TiN, implying that thermodynamics plays a significant role in determining the final structure of laser-doped materials.

In Chapter 4, we utilize the laser-treated and annealed TiO_2 as a photoanode for photoelectrochemical water splitting. When compared to two control samples, the resulting TiO_2 yields nearly triple the rate of photocatalytic oxygen evolution with a measured external quantum efficiency of 12.0% at 354 nm. Through detailed sample characterization with Raman spectroscopy, X-ray diffraction, and temperature-programmed reaction spectroscopy, we show that the photocatalytic enhancement of the laser-treated TiO_2 is due to a complete oxidation of titanium, which includes an absence of TiO_x phases, and a reduced number of oxygen vacancy defects. It is through producing a more pure form of rutile TiO_2 that we achieve a higher rate of water oxidation.

Using the knowledge gained in our initial attempts at nitrogen-doping of TiO_2, we move on to doping transition metals in Chapter 5. We demonstrate that we can incorporate many different transition metals into TiO_2 at high concentrations. After annealing the various samples, we test water splitting in a photoelectrochemical cell. The resulting water oxidation is lower for TiO_2:Cr and TiO_2:Mn, but the water oxidation does not decrease with TiO_2:Ni. We attribute this chemical dopant variability to the placement of the dopant in the lattice with X-ray photoelectron spectroscopy. In addition to TiO_2, we present doping of other oxides, such as Fe_2O_3, with their resulting photocatalysis. By extending the doping method, we prove that doping of a variety of materials is possible though there does not seem to be a gain in the resulting photochemistry due to the laser-induced defects in the doped materials.

Lastly, we describe another application in dental implants in Chapter 6. For dental implant applications, the surface structures formed through laser irradiation of titanium are the ideal size with an oxide that runs deep into the material. By seeding human cells on the surfaces and adding fluorescent dyes, we show that the laser-treatment of titanium metal leads to higher cell adhesion and viability after 48 h. By changing the laser parameters, we still achieve high levels of cell viability, showing that the cell adhesion is invariant to laser parameters.

For future studies on laser doping and structuring of wide band gap semiconductors, there are a number of opportunities moving forward. Besides the materials described in this thesis, there are a variety of material platforms that our lab has yet to explore that could lead to interesting discoveries. Due to the difficulty working with materials that are composed of two elements, future experiments with doping should focus on singular elements, such as with silicon that we have studied extensively or new elements, like germanium. By trying to add in a third element in the form of a dopant, there exists an even larger set of possible combinations of how the elements are positioned in relation to another. With the photoelectrochemical evidence shown here, it is the oxidation state of the dopants that are the main cause of the lower water oxidation. By chosing the material platform carefully, it will be easier to reduce the defects that are inherent in femtsecond-laser doped materials and are known to trap charge carriers.

Furthermore, the use of laser-structured metals and oxides could be used outside for many applications. One new biological application is testing the laser-treated TiO_2 and TiN as plasmonic substrates for cell transfection. As for cell viability in implantology, further research is necessary comparing our samples to sand-blasted surfaces used today in the dental industry. Through working further with the Harvard School of Dental Medicine, a full implant study should be conducted to study how the cells will grow on the surface in vitro as opposed to our studies in vivo. With our initial results on cell adhesion and viability, there are exciting developments ahead with this material platform.

In general, our study of the exotic materials made from the interaction of femtosecond laser pulses with metals and dopants have enabled the preparation of materials unachievable by any other method. In femtosecond laser doping, we are able to introduce dopant concentrations on the order of a few percent, which is not feasible with many other methods. We have pushed the research in our group into other material regimes and intertwined our work into more applications outside of Black Silicon. We have learned more about the femtosecond laser doping technique and can inform future research in this field. The femtosecond laser doping technique has shown its utility not only through the creation of new materials but also through the devices it has enabled.

APPENDIX A

CHIRPED PULSE AMPLIFICATION

Chirped Pulse Amplification (CPA) is one of the most important techniques used in amplifying ultra-short laser pulses. Before the advent of CPA, amplification was limited at high powers by the amount of self-focusing that would occur in the crystal. Now the process involves spreading a pulse, amplifying the broadened pulse, and then compressing the pulse back, lowering the overall intensity in the crystal. In this appendix, the amplification process will be discussed, as well as the nonlinear limits of the current spreading and compressing techniques. We will also provide a comparison of regenerative and multipass amplifiers and will address the use of nonlinear optical parametric amplification for chirped pulses. Femtosecond pulse generation is necessary in order to explore many fields of science, but higher power pulses yield greater interaction with materials and their surroundings. Some examples will be provided of the uses of chirped pulses and their further applications in nonlinear optics.

A.1 Motivation

The process of using chirped pulse amplification has changed the way that short pulses are amplified. Mode-locking was discovered in the 1960s and created pulses in the picosecond range, but the pulses could not be amplified because it damaged the amplifying medium. In order to amplify mode-locked pulses, the gain media needed to handle longer bandwidths and higher stored energies. National laboratories could afford to have large laser systems without finding a new gain medium, but in order to make tabletop lasers that were accessible to the general scientific community, another solution needed to be found. The solution to this problem came in the form of chirped pulse amplification (CPA) at the University of Rochester in 1985.

With the creation of shorter pulses came higher peak intensities around 10^9 W/cm^2. To amplify picosecond pulses, the nonlinear effects that occur at these powers first need to be calculated. The index of refraction for nonlinear materials is given by:

$$n = n_0 + n_2 \cdot I. \tag{A.1}$$

where n_0 is the linear refractive index, n_2 is the nonlinear index of refraction, and I is the intensity, related to the energy squared, of the propagating pulse. [179] This generates a change in the nonlinear phase:

$$B = \frac{2\pi}{\lambda} \int_0^l n_2 \cdot I(z)\,\mathrm{d}z. \tag{A.2}$$

after propagating a length l in the crystal. [5] As the intensity is spatially-dependent, the nonlinear phase will also change over the length of the pulse. With a Gaussian-shaped pulse, the nonlinear phase will be the largest in the center of the pulse, where the intensity is the highest. Another way of looking at this situation is that the nonlinear index essentially becomes spatially-dependent. With a larger index of refraction in the center, the pulse acts like a lens and causes self-focusing to occur. The process of self-focusing will damage the crystal at high enough intensities. The nonlinear phase, referred to as the B-value from Eqn. A.2, shows that damage will occur in the crystal for an input Gaussian pulse when the power exceeds a critical power, given by:

$$P_{cr} = \frac{\lambda^2}{2\pi \cdot n_0 \cdot \ n_2}. \tag{A.3}$$

To amplify picosecond pulses in the 1970s, the beam size needed to be enlarged, which decreased the intensities, was costly, and forced the repetition rate to be decreased. A new method was needed to amplify these pulses that kept the nonlinear effects from destroying the crystal.

For an efficient laser, it is also necessary to have an input fluence, defined as the energy per area, comparable in size to the saturation fluence of the crystal:

$$F_{sat} = \frac{h \cdot \nu}{\sigma}. \tag{A.4}$$

where h is Plank's constant, ν is the frequency, and σ is the emission cross-section for the gain medium. [180] With similar input fluences, the stored energy can be extracted from the amplifier. The saturation fluence for Ti:sapphire lasers is around 1 J/cm^2, meaning that the input fluence should be on that order. A problem emerges from this situation when the damage fluence is less than the saturation fluence. To solve this problem, the pulse needs to pass through the crystal multiple times, but at such high intensities, this was not an option. Due to the lack of methods to amplify picosecond pulses, only dye lasers were used in labs before the invention of CPA.

A.2 Chirped Pulse Amplification

A.2.1 Basic Design

The solution that solves the issues presented above lies in Chirped Pulse Amplification (CPA). CPA has three main steps—pulse spreading, amplification, and pulse compression, which are shown in detail in Fig. 2.1. By spreading the pulse orders of magnitude in time and space, the pulse can be amplified in the crystal without damaging it or including nonlinear effects. [7] With a spread pulse, the overall fluence is the same but the power measured at any one frequency is significantly lower. After amplification, the pulse goes through the same method used to spread the pulse but in the opposite direction in order to compress the pulse back down.

The process of spreading and compressing can be achieved in many ways, including gratings and prims, which are explained below.

A.2.2 Chirped Pulse

When the pulse is dispersed by the spreader, the pulse becomes chirped, meaning that the many frequencies in the bandwidth are separated in time, as shown in Fig. A.1. The chirp comes from both the self-phase modulation and group velocity dispersion. The process is demonstrated in Fig. **??** as the red, green, and blue lines, representing different frequencies in the pulse, travel different path lengths in the spreader and compressor. For a positively chirped pulse, higher frequencies, like blue light, diffract with a lower angle from the normal than lower frequencies, such as red light, and thus travel a longer path length. This produces a pulse with the lower frequencies (red light) arriving first in time followed by the higher frequencies (blue light) coming later in time. Most systems produce positively-chirped pulses in the spreading process.

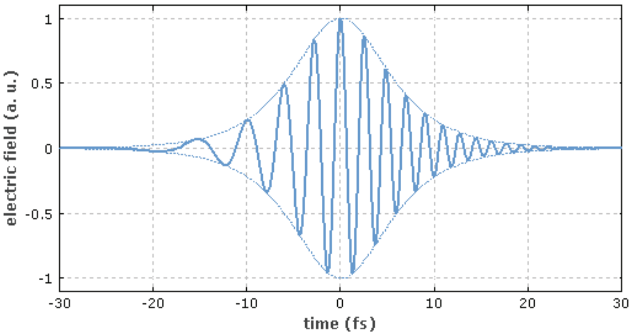

Figure A.1: Chirped Pulse, courtesy of Photonics.com website.

A.2.3 Pulse Spreading and Compressing

The invention of the spreading and compressing mechanism was a key factor in allowing CPA to work because the pulse could reach higher powers when it was spread orders of magnitude in time. The first spreader was designed by Strickland and Mourou in 1985 using an optical fiber for spreading with parallel gratings for compression. [7] Although this changed the field as we know it, their imperfect design did not compress the pulse the same as it was spread. This mismatch between the spreader and compressor only helped to spread the pulse two orders of magnitude before the pulse was too distorted to use. It was with the idea of M. Pessot in 1987 to perfectly match both components that allowed for such large changes in pulse duration between the input and spread pulse without significantly altering the wavefront of the output pulse. [9] His first design, which utilized a telescoped-grating pair matched with another grating pair, was able to spread the pulse 1000 times and laid the foundation for all future improvements in spreader-compressor designs.

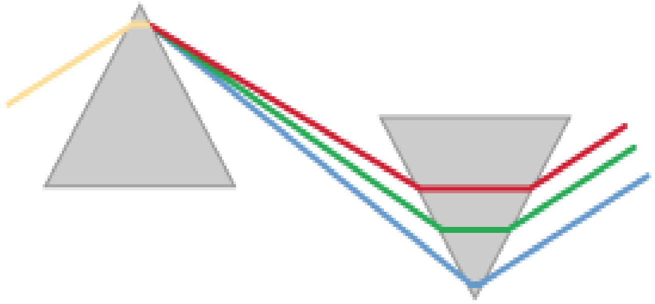

Figure A.2: Prism pair used for spreading a pulse, courtesy of Photonics.com website.

The normal method for spreading and compressing the pulse is by changing the second order dispersion, called group velocity dispersion (GVD) [181], given by D and defined as:

$$D(\omega) = \frac{-2\pi c}{\lambda^2} \cdot \frac{d^2\beta}{d\omega^2}. \tag{A.5}$$

For the spreader-compressor design, there are many configurations used in laser systems today. Fig. 2.1 shows the use of a telescope-grating combination for the spreading and a grating pair for the compressor. Prism pairs can also be used, which are shown in Fig. A.2. In most cases, the spreader enacts positive GVD, and the compressor enacts the opposite with negative GVD.

Matching the spreader and compressor is not the only step to ensure that the net GVD is zero for the pulse. As pulses became shorter, the delay from the coatings on the optics became an issue and had to be taken into account by adding in more optical components to equal out the GVD calculation.

A.3 Limitations to Chirped Pulse Amplification

A.3.1 Self-Phase Modulation

One main limiting factor in maximizing the amplification of pulses using CPA is self-phase modulation. To examine its effect on the wave, it is first necessary to look at how the electric field E is affected by the spreader-compressor design. The electric field can be split into a transverse component F and a complex amplitude component A with:

$$E(r,t) = \frac{F(x,y) \cdot A(z,t) \cdot e^{i(k_0 z - w_0 t)} + c.c.}{2}. \tag{A.6}$$

Neglecting the saturated gain term, the nonlinear Schroedinger equation becomes:

$$i\frac{\partial A(z,t)}{\partial z} = i\frac{\alpha}{2}A(z,t) + \frac{1}{2}\beta_2\frac{\partial^2 A(z,t)}{\partial \tau^2} - \frac{1}{6}\beta_3\frac{\partial^3 A(z,t)}{\partial \tau^3} - \gamma\left|A\right|^2 A(z,t), \tag{A.7}$$

where α represents the net gain, $\beta_2 = \frac{\partial^2 k}{\partial \omega^2}$ is the group velocity dispersion (GVD), $\beta_3 = \frac{\partial^3 k}{\partial \omega^3}\omega_0$ is the group delay dispersion (GDD), $\tau = t - \frac{z}{\nu_g}$, and $\gamma = \frac{n_2 \omega_0}{c}$. [182] When there is no contribution from nonlinearity, $\gamma = 0$, Eqn. A.7 can be solved using Fourier transforms to yield transform-limited pulses as long as:

$$\phi_{stretching}(w) + \phi_{compressing}(w) + \phi_{materialdispersion}(z,t) = 0. \tag{A.8}$$

When nonlinearity is taken into account, Eqn. A.7 must be solved numerically. To simplify the calculation, assume no material dispersion, $\beta_2 = \beta_3 = 0$. This is a valid assumption for a majority of laser systems that use CPA because the dispersion from the stretching and compressing is much larger than the dispersion from the gain medium. Eqn. A.7 then becomes:

$$i\frac{\partial A(z,t)}{\partial z} = i\frac{\alpha}{2}A(z,t) - \gamma\left|A\right|^2 A(z,t). \tag{A.9}$$

With the substitution $A(z,t) = \Lambda(z,t)e^{i\phi(z,t)}$, Eqn. A.9 can be decoupled into equations for the amplitude of the pulse Λ and the phase ϕ:

$$\frac{\partial\Lambda}{\partial z} = \frac{\alpha}{2}\Lambda(z,t), \frac{\partial\phi}{\partial z} = \gamma A^2. \tag{A.10}$$

Using these equations, numerical models were performed with various energy fluences, which alters the nonlinear phase (B-value) in the material without introducing more dispersion. The result is shown in Fig. A.3 for B-values=0, 1, 2, 3. For B=0, the pulse is transform-limited and is compressed fully to its original duration, as shown in Eqn. A.8. The recompressed pulses have longer pulse durations as the B-value increases. It has been shown that the frequency modulation of the pulse is determined by the time derivative of the nonlinear phase (B-value), shown with:

$$\omega(t) = \omega_0(t) - \frac{\partial B}{\partial t}. \tag{A.11}$$

When B=0, Eqn. A.11 presents that reinforcing that the linear pulse should be transform-limited and unchanged by the spreader-compressor process.

Although self-phase modulation plays an important role, the overall effect on a 100-fs pulse is on the order of 10^{-4} and will mostly serve as a detriment to the quality of the pulses after amplification.

A.3.2 Gain Narrowing

A major issue with CPA occurs when the bandwidth of the spectrum being amplified is greater than the bandwidth of the amplifying medium. The frequencies

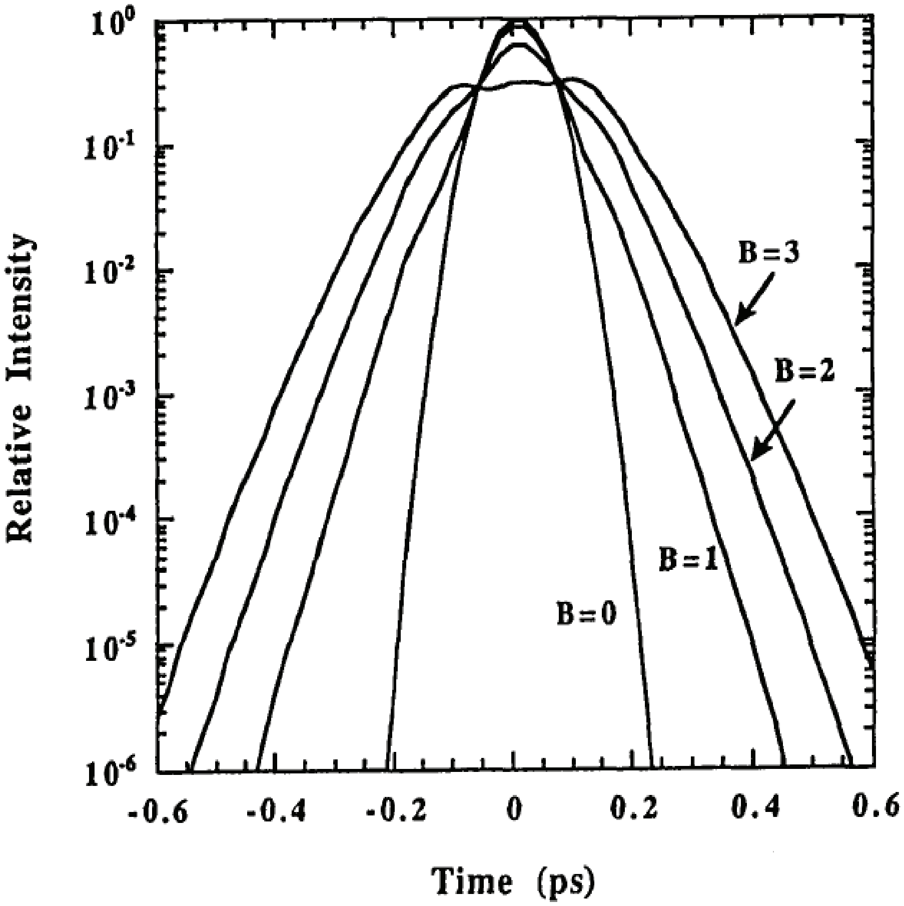

Figure A.3: Numerically-calculated compressed pulse shapes for 100 fs input pulses with varying nonlinear phases or B value, taken from Ref. [182] .

that are outside the medium's bandwidth are essentially lost when the other frequencies are amplified by orders of magnitude. This causes the bandwidth to narrow, a phenomenon called gain narrowing. Although CPA gives rise to very short, highly energetic pulses, gain narrowing represents a limitation in creating even shorter pulses with pulse durations less than 10 fs. With a Gaussian-shaped incoming pulse, the change in the spectrum of the pulse is calculated as:

$$\Delta\omega = \Delta\omega_a \sqrt{\frac{3}{G(\omega_a) - 3}}, \tag{A.12}$$

where G is the gain in decibels and $\Delta\omega_a$ is the material gain bandwidth. [183] When saturation is not taken into account, the intensity of the pulse after the compressor is given by:

$$I_{out}(\omega) = I_0(w)G(w)^n T(w)^n, \tag{A.13}$$

with gain G, input intensity I, number of passes through the gain medium n, and transmission function of the amplifying medium T. [184] To help reduce gain-narrowing, the bandwidth of the medium should be increased. It is also possible to give the incoming intensity a spectral profile that is opposite of the effect that CPA generates.

A.3.3 Gain Shifting

Another limitation with CPA is gain shifting. When the pulse is chirped, the frequencies are separated in time, as described above, but this means that the different frequencies of the pulse exhibit varying amounts of amplification. The front part of the pulse receives more gain than the back part of the pulse, meaning that the pulse shape changes and is no longer symmetric. [184] For a positive chirp (lower frequencies first), the lower frequencies are amplified more than the higher frequencies. The wavefront distortion due to gain shifting is difficult to control but should be accounted for when using CPA.

A.4 CPA Designs

A.4.1 Regenerative and Multipass Amplifiers

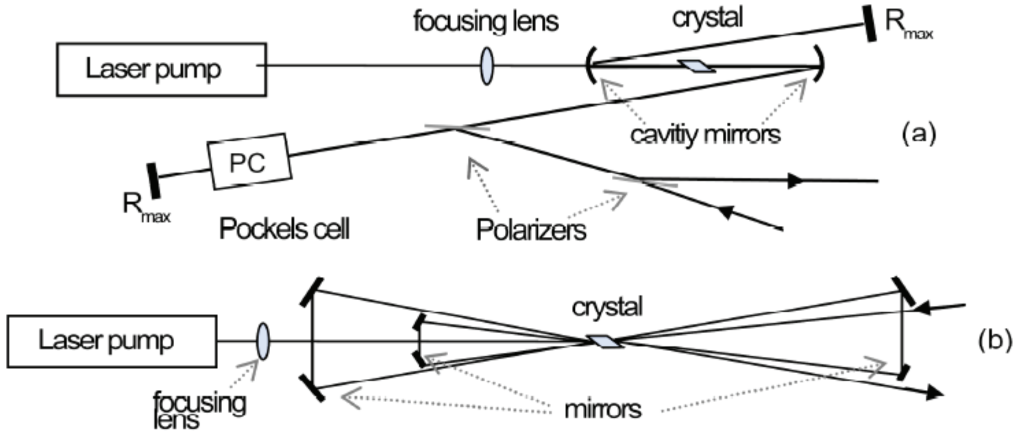

Figure A.4: Diagrams of regenerative (a) and multipass (b) amplifiers (Courtesy of V. Nuzzo).

There are two main types of amplifiers used commercially and academically: regenerative and multipass, shown in Fig. A.4. They each have their advantages and disadvantages. The main difference between the two amplifiers is how the number of passes through the amplifying media is determined. The multipass is configured for a fixed number of passes, while the regenerative amplifier extracts pulses once they reach a certain energy. The regenerative amplifier gives the user much more flexibility in how much the pulse is to be amplified and thus yields the highest extraction energies of amplifiers on the market. However, the multipass is inherently simpler with less optical components that cause dispersion and losses to the signal.

A regenerative amplifier consists of a cavity that contains the gain medium, an electro-optic switch, which is usually a Pockels cell, and a set of polarizers. The pulse is forced into the cavity by an electro-optic switch and then passes through the crystal multiple times within the resonator cavity. The switch can then be turned on again to let the amplified pulse out of the resonator. The design in Fig. A.4a uses the Pockels cell to act as the switch. [185] The Pockels cell is set at an angle in relation to the cavity so that it can act as a half- or quarter-wave plate. When a voltage is applied across the Pockels cell, the birefringence in the crystal causes the cell to act as a quarter wave plate and let pulses through. Using the polarizers in the above setup allows a pulse to enter the resonator when the switch is turned on, bounce back and forth through the amplifying media, and leave the cavity after an arbitrary number of passes through the crystal. This type of amplifier extracts extremely large energies but can be easily degraded with losses in the cavity and misalignment with the Pockels cell.

For multipass amplifiers, the pulse follows a distinct path where mirrors are used to direct its movement through the crystal. The multipass amplifier is designed to maximize the gain in a given number of passes, such as four passes as shown in Fig. A.4b. It is more difficult to change once setup so the number of passes through the crystal is inherently constant for the lifetime of the laser. With less passes through the crystal comes less dispersion that must be accounted for elsewhere, but the alignment of the mirrors must be precise to extract all of the energy out efficiently.

In practice, their pros and cons are used for different applications. When the gain is lower per pass through the crystal, regenerative amplifiers are used. However, when the gain is high per pass but the crystal has a lower saturation fluence, the multipass configuration is used. In Fig. A.5, we can see that there is a large disparity in the output bandwidth using the two types of amplifiers. In *Le Blanc et. al.*, the multipass amplifier has a larger output bandwidth for both the shorter and longer input bandwidths. [186] However, when other factors are taken into account the spectral bandwidth after amplification may not be the most important factor for an amplification scheme. It is important to analyze the input pulse, amplifying medium, and desired output pulse to determine which configuration will be the most efficient use of time, money, and energy.

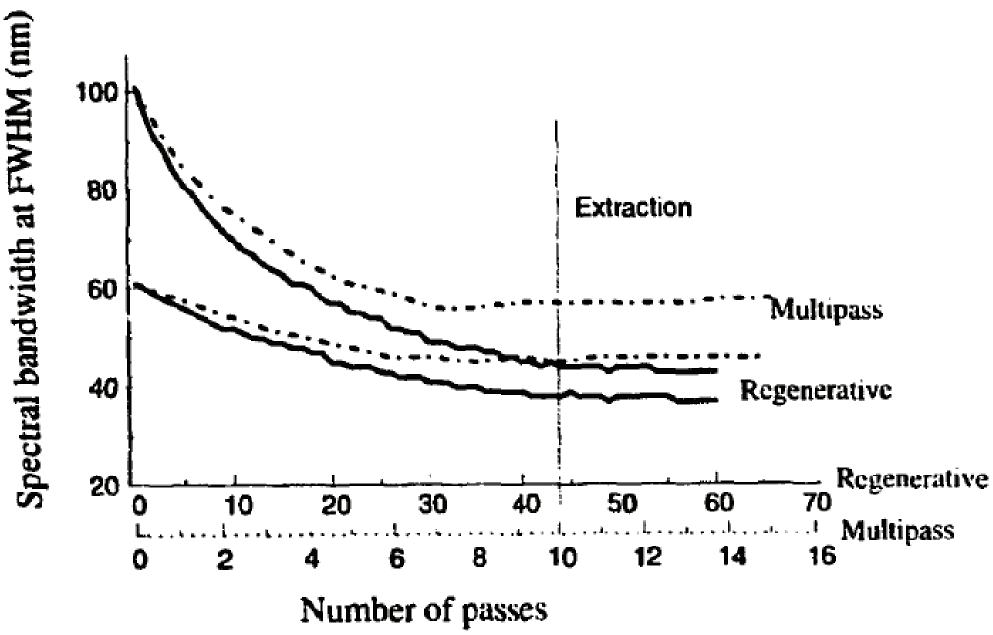

Figure A.5: Comparison of bandwidths given two input pulses with durations of 60 fs and 100 fs for regenerative (line) and multipass (dotted) amplifiers, taken from Ref. [186].

A.5 Optical Parametric Chirped Pulse Amplification

After the development of CPA in the late 1980s, scientists went on to explore the application of nonlinear properties in CPA—most notably with the use of optical parametric chirped pulse amplification (OPCPA). OPCPA involves three waves: the pump, the signal, and the idler. It is a form of difference-frequency generation with parametric gain occurring inside the nonlinear gain medium. At a specific crystal length, l_c, called the coherence length, the gain increases in the signal pulse and the phase condition differs from the ideal phase condition:

$$\Delta\phi = \phi_{pump} - \phi_{signa} - \phi_{idler} = \frac{-\pi}{2} \tag{A.14}$$

by a factor of $\Delta\phi = \pi$. [187]

There are many advantages of using OPCPA over conventional CPA. Because OPCPA works with similar crystals used in CPA, OPCPA has the same bandwidth and therefore can handle the same pulse durations. Due to the OPCPA's construction, it can also be tuned to produce many output wavelengths, while conventional lasers are wavelength-dependent. Another advantage is a decrease in the overall noise of the signal pulse by transferring the pulse aberrations in the pump pulse to the idler pulse.

Although OPCPA can generate high-energy, ultra-short pulses across different wavelengths, it is more difficult to to use from an experimental viewpoint. To yield an amplified, usable pulse, the two input pulses, the signal and pump, must have equal pulse durations. For maximized amplification, the crystals must be cut precisely and aligned carefully to obey the phase-matching conditions. Dephasing also can become a problem with inadequate beam quality in either the signal or pump beams. OPCPA is used in larger laser systems like some of the petawatt lasers discussed later.

A.6 Utilizaton of Ultra-Short Pulses

A.6.1 Major Applications

The applications of amplified pulses are spread throughout many fields, and the number of applications has only increased as pulses have become shorter in time and higher in energy. Some of the most important outcomes include high-harmonic generation, plasma interaction, and nonlinear quantum effects, such as quantum electrodynamics. [188]

Many labs make use of second- and third-harmonic generation, which is used to generate pulses with frequencies one-half to one-third of the original pulse length respectively. With intensities above 10^{14} W/cm^2, high-harmonic generation (HHG) applies the same principles to output pulses significantly shorter than the input pulse (on the order of 1/20 to 1/100). The harmonics are excited from surrounding gas atoms and release X-rays. The interaction time is extremely short, so the X-ray lifetime is equal to the duration of the input pulse. The cutoff harmonic frequency is calculated by:

$$h\nu_n = E_i + 3.2U_p, \tag{A.15}$$

with ionization energy E_{i} and ponderomotive energy, U_{p}, of an electron excited in an electric field in the laser. The 143$^{\mathrm{rd}}$ harmonic has been observed with a 1054 nm pulse interacting with helium. [188] As with all harmonic generation, HHG is limited by phase-matching conditions. Being able to generate these ultra-long X-ray pulses in a laboratory setting presents great strides in the field because many other X-ray sources require a synchrotron or other high energy source, such as a plasma facility.

At intensities around 10^{16}–10^{18} W/cm^2, the electrons in the surrounding field of gas are excited and create a plasma. Since the electrons are moving with a velocity close to the speed of light, a large magnetic field is created. This form of plasma excitation can also create a plasma stream when impacted with enough intensity. Although the conditions for plasma production are extremely laser-dependent, the plasma once created has a time-varying frequency, which causes relativistic self-focusing. With such large intensities focused down to an even smaller location, the surrounding electrons will create an extremely large magnetic field, which can be used for other experiments.

Looking at even higher intensities, laser-modified quantum electrodynamics is a developing field. When the laser interacts with many atoms, states of different atoms are forced to couple with one another and to the vacuum. This promotes quantum interference, which can be studied to see the atomic interaction between states. Multi-photon pair production and electron-positron coupling have been observed using an electron beam at SLAC. [188] With increased laser intensities, scientists will be able to explore new extremes, whether it be with easily-produced soft X-rays or pair production on the relativistic time-scale.

A.6.2 Petawatt Lasers

In order to produce ultra-short pulses with extremely high intensities, a couple of research groups have set out to build a laser that produces powers in the petawatt region (10^{15} W). When focused to a small spot, petawatt lasers can produce enormous intensities. Before the petawatt laser was built, the maximum power extracted from a Ti:sapphire laser using CPA was on the order of 125 TW (10^{14} W). [189] The Petawatt Project, started at Lawrence Livermore National Laboratory, ventured to build a huge laser using part of the components from their previously-constructed NOVA laser.

The Petawatt Project has a very complex design that consists of a laser pumped at 1054 nm with two resonators, both of which contain Ti:sapphire crystals and are pumped by Nd:YAG lasers. The first amplifier has a linear cavity design that acts like an oscillator to account for self-focusing and thermal lensing effects. The second amplifier is a ring regenerative amplifier. The pulse then experiences amplification from multiple rod amplifiers. Once sent to the disk amplifiers, the pulse is amplified to around 1 kJ for a beam size around 60 cm. Due to the large size of the beam, the diffraction gratings used for spreading and compressing are over a meter long. The overall output of the laser was around 1.5 PW (1500 TW) for a 800 fs-pulse, breaking the power barrier in the field. When the beam was focused down, the intensity exceeded 10^{20} W/cm^2. [189]

The Petawatt Project brought about many discoveries while it was in commission from 1996 to 1999. With such high energies, the beam was able to break open gold nuclei and produce other elements as the gold decayed. The freed gold electrons also accelerated and created X-rays, which decayed into electron-positron pairs. Many other groups went on to build petawatt lasers, but it was the Petawatt Project that began the experimental quest to maximize the energy output of the laser. The subsequent projects have been built with shorter pulses but smaller peak powers.

A.7 Future Work

A.7.1 Theoretical Limit of Pulse Amplification

Pulses continued to decrease in duration, but many other limitations have blocked the development of even shorter ultrafast pulses. With the invention of Kerr Lens Mode-locking in 1991, pulses could be generated less than 10 fs. Attosecond pulses came into play at a later time, but the additional components added to the CPA mechanism to create and amplify pulses in this length-scale is outside the scope of this appendix.

To theoretically understand the limit of pulse amplification, we must return to the saturation fluence, given in Eqn. A.4. The shortest pulses generated are a limiting factor, but given any pulse duration, we must examine the amplifying medium's bandwidth, given as such that the threshold power P_{th} is:

$$P_{th} = \frac{h\nu\Delta\nu}{\sigma}. \tag{A.16}$$

Eqn. A.16 demonstrates that the peak power is limited by the gain bandwidth and the cross-section of the gain material. To calculate the threshold intensity I_{th}, we must taken into account the power focused onto an area created by the wavelength squared. [185] This yields:

$$I_{th} = \frac{h\nu\Delta\nu}{\lambda^2\sigma} = \frac{h\nu^3\Delta\nu}{c^2\sigma}. \tag{A.17}$$

To maximize the intensity of the ultrashort pulse, it is necessary to increase the bandwidth and decrease the cross-sectional area of the amplifying medium. When examining the usual gain media used in the field with a square cross-section of 100 cm^2, a Yb:glass laser, with a threshold power around 3000 TW, could theoretically produce a spot with an intensity on the order of 10^{22} $\mathrm{W/cm}^2$. [190] For various other crystals and improved designs, the maximum intensity could be extended at least three orders of magnitude.

A.7.2 Experimental Limit of Pulse Amplification

Although theoretically higher intensities can be produced than what the best lasers have shown to date, the question becomes how much further can these limits be pushed experimentally. By improving on the design of the terawatt laser, more pulse aberrations can be accounted for and dispersion can be further minimized. However, small improvements will not bring about a power increase in two orders of magnitude. To make larger leaps, a new system must be devised. There is one project, still in the planning stages and based in Europe, called the Extreme Light Infrastructure that hopes to produce pulses with peak powers in the exawatt range (10^{18} W) with initial intensities around 10^{23} $\mathrm{W/cm}^2$ and later intensities $>10^{25}$ $\mathrm{W/cm}^2$. [191] By amplifying the pulse with a Nd:YAG and two Nd:glass amplifiers, the pulse will reach 25 PW and rival some of the top terawatt lasers to date. It is the last step, which involves collimating ten beamlines at the 25 PW level, that will produce energies near the exawatt regime. Because Extreme Light Infrastructure is only in the planning stages, it will take years to design and construct each beamline and possibly a decade before experiments will be completed at this intensity regime.

A.8 Conclusion

After this discussion on how ultra-short pulses are amplified, it is clear to say that not only has this process been achieved but that it has been refined. By spreading, amplifying, and recompressing pulses, it has become possible to amplify pulses in the picosecond and femtosecond range without causing damage to the gain medium or distorting the wavefront. While self-phase modulation and gain-narrowing limit the bandwidth and quality of the amplified pulses, many laser designs exist to minimize their effect. The majority of amplifiers used for ultra-short amplification use one of the main types of amplifiers described here, including regenerative, multipass, and OPCPA. The petawatt lasers have tackled another realm of peak power production with the applications of ultra-short amplified pulses spread throughout many engineering and physics disciplines.

We will only continue to see shorter pulse durations with wider bandwidths at higher intensities. As pulses become shorter, it will be possible to view more interactions that occur on such a short time scale. With higher intensities and powers, we can send higher peak powers to smaller regions and explore other areas outside of optics, such as astrophysics and biophysics. With so many applications, we will continue to use Chirped Pulse Amplification to produce shorter pulses and utilize the pulses across various disciplines.

BIBLIOGRAPHY

[1] Bo Gu, Proc. SPIE **5339**, 226 (2004).

[2] Koji Sugioka and Ya Cheng, Light Sci. Appl. **3**, e149 (2014).

[3] M. DiDomenico, J. Appl. Phys. **35**, 2870 (1964).

[4] L. E. Hargrove, R. L. Fork, and M. A. Pollack, Appl. Phys. Lett. **5**, 4 (1964).

[5] P. Maine, D. Strickland, P. Bado, M. Pessot, and G. Mourou, IEEE J. Quantum Electron. **24**, 398 (1988).

[6] G. E. Cook, IEEE Proc. IRE **48**, (1960).

[7] Donna Strickland and Gerard Mourou, Opt. Commun. **55**, 447 (1985).

[8] Perry, Sci. Technol. Rev. 24 (1995).

[9] M. Pessot, P. Maine, and G. Mourou, Opt. Commun. **62**, 419 (1987).

[10] S K Sundaram and E Mazur, Nat. Mater. **1**, 217 (2002).

[11] Mark Thomas Winkler, Ph.D. thesis, Cambridge, Massachusetts, 2009.

[12] Chris Dorman, Laser Tech. J. **5**, 44 (2008).

[13] J. M. Liu, H. Kurz, and N. Bloembergen, Appl. Phys. Lett. **41**, 643 (1982).

[14] J. M. Liu, R. Yen, H. Kurz, and N. Bloembergen, Appl. Phys. Lett. **39**, 755 (1981).

[15] D. Von der Linde and N. Fabricius, Appl. Phys. Lett. **41**, 991 (1982).

[16] J A Kittl, P G Sanders, M J Aziz, D P Brunco, and M O Thompson, Acta Mater. **48**, 4797 (2000).

[17] B. N. Chichkov, C. Momma, S. Nolte, F. von Alvensleben, A. Tunnermann, F. Alvensleben, and A. Tünnermann, Appl. Phys. A **63**, 109 (1996).

[18] P Lorazo, L J Lewis, and M Meunier, Phys. Rev. B **73**, 22 (2006).

[19] J E Sipe, J F Young, J S Preston, and H M Vandriel, Phys. Rev. B **27**, 1141 (1983).

[20] J Bonse and J Kruger, J. Appl. Phys. **108**, (2010).

[21] B R Tull, J E Carey, E Mazur, J P McDonald, and S M Yalisove, MRS Bull. **31**, 626 (2006).

[22] J F Young, J E Sipe, and H M Vandriel, Phys. Rev. B **30**, 2001 (1984).

[23] H. van Driel, J. Sipe, and Jeff Young, Phys. Rev. Lett. **49**, 1955 (1982).

[24] G. Dumitru, V. Romano, H.P. Weber, M. Sentis, and W. Marine, Appl. Phys. A Mater. Sci. Process. **74**, 729 (2002).

[25] Nitinkumar Sudani, Ph.D. thesis, 2009.

[26] C. Bradley Moore, *Chemical and Biochemical Applications of Lasers* (Academic Press, New York, 2012), p. 410.

[27] A. Sabbah and D. Riffe, Phys. Rev. B **66**, 165217 (2002).

[28] P. Saeta, J.-K. Wang, Y. Siegal, N. Bloembergen, and E. Mazur, Phys. Rev. Lett. **67**, 1023 (1991).

[29] Yamac Dikmelik, Caroline McEnnis, and James B. Spicer, Opt. Express **16**, 5332 (2008).

[30] Renee R. Frontiera, Anne-Isabelle Henry, Natalie L. Gruenke, and Richard P. Van Duyne, J. Phys. Chem. Lett. **2**, 1199 (2011).

[31] Barada K. Nayak, Vikram V. Iyengar, and Mool C. Gupta, Prog. Photovoltaics Res. Appl. **19**, 631 (2011).

[32] T. Jia, H. Chen, M. Huang, F. Zhao, J. Qiu, R. Li, Z. Xu, X. He, J. Zhang, and H. Kuroda, Phys. Rev. B **72**, 125429 (2005).

[33] Kiminori Okamuro, Masaki Hashida, Yasuhiro Miyasaka, Yoshinobu Ikuta, Shigeki Tokita, and Shuji Sakabe, Phys. Rev. B **82**, 1 (2010).

[34] Susanta Kumar Das, Kiran Dasari, Arkadi Rosenfeld, and Ruediger Grunwald, Nanotechnology **21**, 155302 (2010).

[35] Elizabeth C. Landis, Katherine C. Phillips, Eric Mazur, and Cynthia M. Friend, J. Appl. Phys. **112**, 063108 (2012).

[36] Vikram V. Iyengar, Barada K. Nayak, and Mool C. Gupta, Sol. Energy Mater. Sol. Cells **94**, 2251 (2010).

[37] V V Iyengar, B K Nayak, K L More, H M Meyer, M D Biegalski, J V Li, and M C Gupta, Sol. Energy Mater. Sol. Cells **95**, 2745 (2011).

[38] Benjamin G Lee, Lin Yu-Ting, Sher Meng-Ju, Eric Mazur, Howard M. Branz, Yu-Ting Lin, and Meng-Ju Sher, in *Photovolt. Spec. Conf. (PVSC), 2012 38th IEEE* (IEEE, Austin, 2012), pp. 1606–1608.

[39] E Yablonovitch, J. Opt. Soc. Am. **72**, 899 (1982).

[40] V. Zorba, L. Persano, D. Pisignano, A. Athanassiou, E. Stratakis, R. Cingolani, P. Tzanetakis, and C. Fotakis, Nanotechnology **17**, 3234 (2006).

[41] Tommaso Baldacchini, James E Carey, Ming Zhou, and Eric Mazur, Langmuir **22**, 4917 (2006).

[42] Ričardas Buividas, Mindaugas Mikutis, Tadas Kudrius, ArtÅńras Greičius, Gintas Šlekys, and Saulius Juodkazis, Lith. J. Phys. **52**, 301 (2012).

[43] Hongliang Wang, Ph.D. thesis, 2013.

[44] Heather Booth, J. Laser Micro/Nanoengineering **5**, 183 (2010).

[45] Paulius Gecys, G Raciukaitis, and A Wehrmann, J. Laser Micro/Nanoengineering **7**, 33 (2012).

[46] Tai-Wook Kim, Jeong-Yun Lee, Do-Hun Kim, and Heui-Jae Pahk, Int. J. Precis. Eng. Manuf. **14**, 1287 (2013).

[47] David Ruthe, Klaus Zimmer, and Thomas Höche, Appl. Surf. Sci. **247**, 447 (2005).

[48] Anna Risch and Ralf Hellmann, Phys. Procedia **12**, 133 (2011).

[49] Rajesh Patel, Beam profile effect for thin film solar cell scribing, 2010.

[50] F Colville, Glob. Sol. Technol. 12 (2009).

[51] O Haupt, V Schutz, and R King, in *Proc. 28th ICALEO* (LIA, Orlando, 2009), p. M 903.

[52] V Schütz, O Haupt, U Stute, H Nagel, and G. Lorenz, in *Proc. 25th EUPVSEC* (EUPVSEC, Valencia, 2010).

[53] XXX Sedao, Thierry Sarnet, Mohamed Fares, Malte Schlutz-Ruhtenberg, Jose Luis Hernandez, Stephan Krantz, and Richard Russel, in *Proc. EU PVSEC* (EUPVSEC, Valencia, 2010), No. September, pp. 2325–2328.

[54] XXX Sedao, Thierry Sarnet, Jose Luis Hernandez, Malte Schlutz-Ruhtenberg, and Stephan Krantz, Adv. Mater. Res. **321**, 234 (2011).

[55] R. Bartlome, B. Strahm, Y. Sinquin, a. Feltrin, and C. Ballif, Appl. Phys. B **100**, 427 (2010).

[56] G. Kamlage, T. Bauer, A. Ostendorf, and B.N. Chichkov, Appl. Phys. A **77**, 307 (2003).

[57] F. Korte, S. Nolte, B.N. Chichkov, T. Bauer, G. Kamlage, T. Wagner, C. Fallnich, and H. Welling, Appl. Phys. A Mater. Sci. Process. **69**, S7 (1999).

[58] J. Bonse, M. Geuss, S. Baudach, H. Sturm, and W. Kautek, Appl. Phys. A Mater. Sci. Process. **69**, S399 (1999).

[59] H.Y. Zheng, X.C. Wang, and Z.K. Wang, in *Adv. Laser Mater. Process. Technol. Res. Appl.*, edited by J.R. Lawrence, J. Pou, D.K.Y. Low, and E. Toyserkani (Woodhead Publishing Limited, Cambridge, 2010), Chap. 5, pp. 88–130.

[60] J.S. Dahm, Short pulsewidth, high pulse repetition frequency laser, 1997.

[61] J Sillanpaa, J Kangastupa, A Salokatve, and H Asonen, in *IEEE/SEMI Adv. Semicond. Manuf. Conf.* (IEEE, Munich, 2005).

[62] A Yokotani, T Mukumoto, T Mizuno, K Kurosawa, K Kawahara, T Ninomiya, and H Sawada, in *Proc. SPIE* (SPIE, San Jose, 2004), pp. 374–380.

[63] HK Tonshoff, A. Ostendorf, K Korber, and N Barsch, in *Proc. SPIE* (SPIE, Osaka, 2003), pp. 219–225.

[64] Daniel Recht, Ph.D. thesis, 2013.

[65] C Wu, C H Crouch, L Zhao, J E Carey, R Younkin, J A Levinson, E Mazur, R M Farrell, P Gothoskar, and A Karger, Appl. Phys. Lett. **78**, 1850 (2001).

[66] Mark T. Winkler, Daniel Recht, Meng-Ju Sher, Aurore J. Said, Eric Mazur, and Michael J. Aziz, Phys. Rev. Lett. **106**, 178701 (2011).

[67] C H Crouch, J E Carey, J M Warrender, M J Aziz, E Mazur, and F Y Genin, Appl. Phys. Lett. **84**, 1850 (2004).

[68] M A Sheehy, B R Tull, C M Friend, and E Mazur, Mater. Sci. Eng. B-Solid State Mater. Adv. Technol. **137**, 289 (2007).

[69] B R Tull and E Mazur, Ph.D. thesis, Cambridge, 2007.

[70] B R Tull, M T Winkler, and E Mazur, Appl. Phys. a-Materials Sci. Process. **96**, 327 (2009).

[71] M. J. Sher, M. T. Winkler, and E. Mazur, MRS Bull. **36**, 439 (2011).

[72] R Reitano, P M Smith, and M J Aziz, J. Appl. Phys. **76**, 1518 (1994).

[73] P H Bucksbaum and J Bokor, Phys. Rev. Lett. **53**, 182 (1984).

[74] N F Mott and W D Twose, Adv. Phys. **10**, 107 (1961).

[75] Jonathan P Mailoa, Austin J Akey, Christie B Simmons, David Hutchinson, Jay Mathews, Joseph T Sullivan, Daniel Recht, Mark T Winkler, James S Williams, Jeffrey M Warrender, Peter D Persans, Michael J Aziz, and Tonio Buonassisi, Nat. Commun. **5**, 3011 (2014).

[76] W Huang and W Ranke, Surf. Sci. **600**, 793 (2006).

[77] James E. Carey, Xia Li, and Nathaniel J. McCaffrey, High sensitivity photodetectors, imaging arrays, and high efficiency photovoltaic devices produced using ion implantation and femtosecond laser irradiation, 2014.

[78] J.M.P. Almeida, V. Tribuzi, R.D. Fonseca, A.J.G. Otuka, P.H.D. Ferreira, V.R. Mastelaro, P. Brajato, A.C. Hernandes, A. Dev, T. Voss, D.S. Correa, and C.R. Mendonca, Opt. Mater. (Amst). **35**, 2643 (2013).

[79] Katherine C. Phillips, Ph.D. thesis, 2014.

[80] A. Schneider, K. Sebald, A. Dev, K. Frank, A. Rosenauer, and T. Voss, J. Appl. Phys. **113**, 143512 (2013).

[81] Bonne Eggleston, Sergey Varlamov, and Martin Green, IEEE Trans. Electron Devices **59**, 2828 (2012).

[82] J Huang, N Wu, Q Zhang, and C Zhu, Appl. Phys. Lett. **87**, 173507 (2005).

[83] B.K. Nayak and M.C. Gupta, Appl. Phys. A **89**, 663 (2007).

[84] Hongliang Wang, Panjawat Kongsuwan, Gen Satoh, Y. Lawrence Yao, and Y. Lawrence Yao, (2012).

[85] I. Theodorakos, I. Zergioti, V. Vamvakas, D. Tsoukalas, and Y. S. Raptis, J. Appl. Phys. **115**, 043108 (2014).

[86] Nadeem H. Rizvi, Riken Rev. 107 (2003).

[87] D. Du, X. Liu, G. Korn, J. Squier, and G. Mourou, Appl. Phys. Lett. **64**, 3071 (1994).

[88] Rafael R. Gattass and Eric Mazur, Nat. Photonics **2**, 219 (2008).

[89] S. Passinger, M. S. M. Saifullah, C. Reinhardt, K. R. V. Subramanian, B. N. Chichkov, and M. E. Welland, Adv. Mater. **19**, 1218 (2007).

[90] M.S. Amer, M.A. El-Ashry, L.R. Dosser, K.E. Hix, J.F. Maguire, and Bryan Irwin, Appl. Surf. Sci. **242**, 162 (2005).

[91] DJ Shir and EC Nelson, J. Vac. Sci. Technol. B **28**, 784 (2010).

[92] S. Amoruso, G. Ausanio, R. Bruzzese, M. Vitiello, and X. Wang, Phys. Rev. B **71**, 033406 (2005).

[93] S. Eliezer, N. Eliaz, E. Grossman, D. Fisher, I. Gouzman, Z. Henis, S. Pecker, Y. Horovitz, M. Fraenkel, S. Maman, and Y. Lereah, Phys. Rev. B **69**, 144119 (2004).

[94] S. Amoruso, R. Bruzzese, N. Spinelli, R. Velotta, M. Vitiello, X. Wang, G. Ausanio, V. Iannotti, and L. Lanotte, Appl. Phys. Lett. **84**, 4502 (2004).

[95] Graham K. Hubler, MRS Bull. **17**, 26 (1992).

[96] J. E. Dominguez, X. Q. Pan, L. Fu, P. A. Van Rompay, Z. Zhang, J. A. Nees, and P. P. Pronko, J. Appl. Phys. **91**, 1060 (2002).

[97] X.L. Tong, D.S. Jiang, W.B. Hu, Z.M. Liu, and M.Z. Luo, Appl. Phys. A **84**, 143 (2006).

[98] Alan E Delahoy and Sheyu Guo, in *Handb. Photovolt. Sci. Eng.*, 2nd ed., edited by Antonio Luque and Steven Hegedus (Wiley and Sons, Chichester, 2011), Chap. 17.

[99] Klaus Ellmer, Nat. Photonics **6**, 809 (2012).

[100] A. M. Morales, Science. **279**, 208 (1998).

[101] Yong-fan Zhang, Wei Lin, Yi Li, Kai-ning Ding, and Jun-qian Li, J. Phys. Chem. B **109**, 19270 (2005).

[102] A Gaggl, G Schultes, W D Muller, H Karcher, W D Müller, and H Kärcher, Biomaterials **21**, 1067 (2000).

[103] A Semerok, C Chaleard, V Detalle, J L Lacour, P Mauchien, P Meynadier, C Nouvellon, B Salle, P Palianov, M Perdrix, and G Petite, Appl. Surf. Sci. **138**, 311 (1999).

[104] R G Flemming, C J Murphy, G A Abrams, S L Goodman, and P F Nealey, Biomaterials **20**, 573 (1999).

[105] Stefano Tugulu, Konrad Löwe, Dieter Scharnweber, and Falko Schlottig, J. Mater. Sci. Mater. Med. **21**, 2751 (2010).

[106] B K Nayak, M C Gupta, and K W Kolasinski, Appl. Phys. A **90**, 399 (2007).

[107] A Y Vorobyev, V S Makin, and C L Guo, J. Appl. Phys. **101**, (2007).

[108] Naofumi Ohtsu, Kenji Kodama, Kuniyuki Kitagawa, and Kazuaki Wagatsuma, Appl. Surf. Sci. **255**, 7351 (2009).

[109] Naofumi Ohtsu, Kenji Kodoma, Kuniyuki Kitagawa, and Kazuaki Wagatsuma, Appl. Surf. Sci. **256**, 4522 (2010).

[110] E. Gyorgy, E. György, A. Pérez del Pino, P. Serra, J.L. L. JL Morenza, and A. Perez del Pino, Surf. Coatings Technol. **187**, 245 (2004).

[111] D M Brunette, P Tengvall, M Textor, and P Thomsen, *Titanium in Medicine* (Springer-Verlag, Berlin, 2001).

[112] Barbara D Bovan, Thomas W Hummert, David D Dean, and Zvi Schwartz, Biomaterials **17**, 137 (1996).

[113] Long-Hao Li, Young-Min Kong, Hae-Won Kim, Young-Woon Kim, Hyoun-Ee Kim, Seong-Joo Heo, and Jai-Young Koak, Biomaterials **25**, 2867 (2004).

[114] Cong Wang, Haibin Huo, Michael Johnson, Mengyan Shen, and Eric Mazur, Nanotechnology **21**, 75304 (2010).

[115] P. Temple and M. Soileau, IEEE J. Quantum Electron. **17**, 2067 (1981).

[116] M W Chase, J. Phys. Chem. Ref. Data, Monogr. 9 (1998).

[117] Kaiyong Cai, Michael Müller, Jörg Bossert, Annett Rechtenbach, and Klaus D. Jandt, Appl. Surf. Sci. **250**, 252 (2005).

[118] Jing Zhang, Meijun Li, Zhaochi Feng, Jun Chen, and Can Li, J. Phys. Chem. B **110**, 927 (2006).

[119] A. Mooradian and P. M. Raccah, Phys. Rev. B **3**, 4253 (1971).

[120] R. Nemanich, C. Tsai, and G. Connell, Phys. Rev. Lett. **44**, 273 (1980).

[121] Spengler, W., R. Kaiser, A. N. Christensen, and G. Müller-Vogt, Phys. Rev. B 1095 (1978).

[122] Â Pino, P. Serra, J.L. L Morenza, A Pe, E Gyo, E. György, and A. Pérez del Pino, Appl. Surf. Sci. **186**, 130 (2002).

[123] Allen J. Bard; L.R. Faulkner, *Electrochemical Methods: Fundamentals and Applications* (John Wiley & Sons, New York, 1980), p. 2.

[124] M Gratzel, Nature **414**, 338 (2001).

[125] J Nowotny, C C Sorrell, L R Sheppard, and T Bak, Int. J. Hydrogen Energy **30**, 521 (2005).

[126] A Fujishima and K Honda, Nature **238**, 37 (1972).

[127] Jonathan D B Bradley, Christopher C Evans, Jennifer T Choy, Orad Reshef, Parag B Deotare, François Parsy, Katherine C Phillips, Marko Lončar, and Eric Mazur, Opt. Express **20**, 23821 (2012).

[128] I. Gregora, Unifit procedure.

[129] S. Margueron, A. Bartasyte, A. M. Glazer, E. Simon, J. Hlinka, I. Gregora, and J. Gleize, J. Appl. Phys. **111**, 104105 (2012).

[130] Jean-Charles Dupin, Danielle Gonbeau, Philippe Vinatier, and Alain Levasseur, Phys. Chem. Chem. Phys. **2**, 1319 (2000).

[131] Tian Ming, Jin Suntivich, Kevin J. May, Kelsey A. Stoerzinger, Dong Ha Kim, and Yang Shao-Horn, J. Phys. Chem. C **117**, 15532 (2013).

[132] Till Cremer, Stephen C. Jensen, and Cynthia M. Friend, Accept. to J. Phys. Chem C (2014).

[133] S.P.S. P S Porto, P.A. A Fleury, and T.C. C Damen, Phys. Rev. **154**, 522 (1967).

[134] Bilbao crystallographic server.

[135] C.D. Wagner, A.V. Naumkin, A. Kraut-Vass, J.W. Allison, C.J. Powell, and J.R. Rumble Jr., Technical report (unpublished).

[136] S. Bourgeois, P. le Seigneur, and M. Perdereau, Surf. Sci. **328**, 105 (1995).

[137] M. P. Seah and W. A. Dench, Surf. Interface Anal. **1**, 2 (1979).

[138] H.T. Jr. Clark, J. Met. **Vol: 1**, (1949).

[139] I. I. Kornilov, V. V. Vavilova, L. E. Fykin, R. P. Ozerov, S. P. Solowiev, and V. P. Smirnov, Metall. Trans. **1**, 2569 (1970).

[140] Bo Holmberg, Acta Chem. Scand. 1255 (1962).

[141] G. Lu, A. Linsebigler, and J. T. Yates, J. Phys. Chem. **98**, 11733 (1994).

[142] Ulrike Diebold, Surf. Sci. Rep. **48**, 53 (2003).

[143] William S. Epling, Charles H.F. Peden, Michael A. Henderson, and Ulrike Diebold, Surf. Sci. **412-413**, 333 (1998).

[144] Stephen C. Jensen and Cynthia M. Friend, Top. Catal. **56**, 1377 (2013).

[145] Enrique Farfan-Arribas and Robert J Madix, Surf. Sci. **544**, 241 (2003).

[146] Xiaobo Chen, Lei Liu, Peter Y Yu, and Samuel S Mao, Science **331**, 746 (2011).

[147] Chu-Chi Ting, San-Yuan Chen, and Dean-Mo Liu, J. Appl. Phys. **88**, 4628 (2000).

[148] Zheshuai Lin, Alexander Orlov, Richard M Lambert, and Michael C Payne, J. Phys. Chem. B **109**, 20948 (2005).

[149] Mohammad Mansoob Khan, Sajid A. Ansari, D. Pradhan, M. Omaish Ansari, Do Hung Han, Jintae Lee, and Moo Hwan Cho, J. Mater. Chem. A **2**, 637 (2014).

[150] W. Shockley and W. Read, Phys. Rev. **87**, 835 (1952).

[151] R. Hall, Phys. Rev. **87**, 387 (1952).

[152] P. Salvador, J. Appl. Phys. **55**, 2977 (1984).

[153] L. Kavan, M. Grätzel, S. E. Gilbert, C. Klemenz, and H. J. Scheel, J. Am. Chem. Soc. **118**, 6716 (1996).

[154] R Asahi, T Morikawa, T Ohwaki, K Aoki, and Y Taga, Science (80-.). **293**, 269 (2001).

[155] T Umebayashi, J. Phys. Chem. Solids **63**, 1909 (2002).

[156] Koichi Mizushima, Mitsuaki Tanaka, and Shuichi Iida, J. Phys. Soc. Japan **32**, 1519 (1972).

[157] M. K. Nowotny, L. R. Sheppard, T. Bak, and J. Nowotny, J. Phys. Chem. C **112**, 5275 (2008).

[158] R Dholam, N Patel, M Adami, and A Miotello, Int. J. Hydrogen Energy (2009).

[159] L. Errico, M. Rentería, and M. Weissmann, Phys. Rev. B **72**, 184425 (2005).

[160] Haowei Peng, Jingbo Li, Shu-Shen Li, and Jian-Bai Xia, J. Phys. Condens. Matter **20**, 125207 (2008).

[161] Holger Dau, Christian Limberg, Tobias Reier, Marcel Risch, Stefan Roggan, and Peter Strasser, ChemCatChem **2**, 724 (2010).

[162] Yelena Gorlin and Thomas F Jaramillo, J. Am. Chem. Soc. **132**, 13612 (2010).

[163] André L. J. Pereira, Lourdes Gracia, Armando Beltrán, Paulo N. Lisboa-Filho, José H. D. da Silva, and Juan Andrés, J. Phys. Chem. C **116**, 8753 (2012).

[164] Katherine C. Phillips, Till Cremer, Jin Suntivich, Ausrine Bartasyte, Ann-Kathrin Henss, Cynthia M. Friend, and Eric Mazur, Submitt. to Adv. Energy Mater. (2014).

[165] M.C. Biesinger, X-ray Photoelectron Spectroscopy Reference Pages, 2013.

[166] HW Nesbitt and D Banerjee, Am. Mineral. (1998).

[167] M. C. Biesinger, C. Brown, J. R. Mycroft, R. D. Davidson, and N. S. McIntyre, Surf. Interface Anal. **36**, 1550 (2004).

[168] Mark C. Biesinger, Brad P. Payne, Leo W. M. Lau, Andrea Gerson, and Roger St. C. Smart, Surf. Interface Anal. **41**, 324 (2009).

[169] Andrew P. Grosvenor, Mark C. Biesinger, Roger St.C. Smart, and N. Stewart McIntyre, Surf. Sci. **600**, 1771 (2006).

[170] Min Liu, Lingyu Piao, Lei Zhao, Siting Ju, Zijie Yan, Tao He, Chunlan Zhou, and Wenjing Wang, Chem. Commun. (Camb). **46**, 1664 (2010).

[171] Si H Pan, Daniel Recht, Supakit Charnvanichborikarn, James S Williams, and Michael J Aziz, Appl. Phys. Lett. **98**, 121913 (2011).

[172] T Sekiya, K Ichimura, M Igarashi, and S Kurita, **61**, 1237 (2000).

[173] Kevin Sivula, Florian Le Formal, and Michael Grätzel, ChemSusChem **4**, 432 (2011).

[174] Jin Suntivich, Kevin J May, Hubert A Gasteiger, John B Goodenough, and Yang Shao-Horn, Science **334**, 1383 (2011).

[175] S. Somiya, S. Hirano, and S. Kamiya, J. Solid State Chem. **25**, 273 (1978).

[176] A. M. Yankin and V. F. Balakirev, Inorg. Mater. **38**, 309 (2002).

[177] T. Bak, J. Nowotny, M. Rekas, and C.C. Sorrell, J. Phys. Chem. Solids **64**, 1057 (2003).

[178] Young-Taeg Sul, Carina Johansson, Ann Wennerberg, Lee-Ra Cho, Beom-Seok Chang, and Tomas Albrektsson, Int. J. Oral Maxillofac. Implants **20**, 349 (2005).

[179] Y. R. Shen, *The Principles of Nonlinear Optics* (John Wiley & Sons, Hoboken, 2002), p. 576.

[180] Lee M. Frantz and John S. Nodvik, J. Appl. Phys. **34**, 2346 (1963).

[181] Orazio Svelto, *Principles of Lasers* (Springer; 5th ed. 2010 edition, New York, 2009), p. 620.

[182] M. D. Perry, T. Ditmire, and B. C. Stuart, Opt. Lett. **19**, 2149 (1994).

[183] Ian N. Ross, Pavel Matousek, Geoffrey H. C. New, and Karoly Osvay, J. Opt. Soc. Am. B **19**, 2945 (2002).

[184] C. P. J. Barty, G. Korn, F. Raksi, C. Rose-Petruck, J. Squier, A.-C. Tien, K. R. Wilson, V. V. Yakovlev, and K. Yamakawa, Opt. Lett. **21**, 219 (1996).

[185] C P Barty, T Guo, C Le Blanc, F Raksi, C Rose-Petruck, J Squier, K R Wilson, V V Yakovlev, and K Yamakawa, Opt. Lett. **21**, 668 (1996).

[186] C. Le Blanc and F. Salin, in *Conf. Lasers Electro-Optics*, edited by G. Deutsch, T., Goldsmith, J., Killinger, D., and Valley (Optical Society of America, Baltimore, Maryland, 1995), Vol. 15, p. CWF46.

[187] Igor Jovanovic, Brian J. Comaskey, Christopher A. Ebbers, Randal A. Bonner, Deanna M. Pennington, and Edward C. Morse, Appl. Opt. **41**, 2923 (2002).

[188] M D Perry and G Mourou, Science **264**, 917 (1994).

[189] M. D. Perry, D. Pennington, B. C. Stuart, G. Tietbohl, J. A. Britten, C. Brown, S. Herman, B. Golick, M. Kartz, J. Miller, H. T. Powell, M. Vergino, and V. Yanovsky, Opt. Lett. **24**, 160 (1999).

[190] Xiaodong Yang, Zhi-zhan Xu, Yu-xin Leng, Hai-he Lu, Li-huang Lin, Zheng-quan Zhang, Ru-xin Li, Wen-qi Zhang, Ding-jun Yin, and Bing Tang, Opt. Lett. **27**, 1135 (2002).

[191] Jean-Paul Chambaret, Federico Canova, Rodrigo Lopez-Martens, Gilles Chériaux, Gérard Mourou, Arnaud Cotel, Catherine Le Blanc, Frederic Druon, Patrick Georges, Nicolas Forget, Fabien Plé, and Moana Pittman, in *Conf. Lasers Electro-Optics/Quantum Electron. Laser Sci. Conf. Photonic Appl. Syst. Technol.* (Optical Society of America, Baltimore, Maryland, 2007), p. JWC4.